2-2010

Existence, Stability, and Dynamics of Solitary Waves in Nonlinear Schroedinger Models with Periodic Potentials

Kody John Hoffman Law
University of Massachusetts Amherst, law@math.umass.edu

EXISTENCE, STABILITY AND DYNAMICS OF SOLITARY WAVES IN NONLINEAR SCHRÖDINGER MODELS WITH PERIODIC POTENTIALS

A Dissertation Presented

by

KODY JOHN HOFFMAN LAW

Submitted to the Graduate School of the
University of Massachusetts Amherst in partial fulfillment
of the requirements for the degree of

DOCTOR OF PHILOSOPHY

February 2010

Department of Mathematics and Statistics

EXISTENCE, STABILITY AND DYNAMICS OF SOLITARY WAVES IN NONLINEAR SCHRÖDINGER MODELS WITH PERIODIC POTENTIALS

A Dissertation Presented

by

KODY JOHN HOFFMAN LAW

Approved as to style and content by:

Panayotis G. Kevrekidis, Chair

Nathaniel Whitaker, Member

Hans Johnston, Member

T.J. Mountziaris, Member

George S. Avrunin, Department Head
Mathematics and Statistics

Dedication

To my father and mother, John H. and Julie N. Law,

and my sister, Amity N. Law

without whose support this would never have been possible.

ACKNOWLEDGMENTS

I would like to thank the following people.

Panayotis G. Kevrekidis: for being the chair of my committee and a decicated advisor, for countless hours of tolerance and advice, criticism and support, and neverending ideas.

Nathaniel Whitaker, Hans Johnston, and T.J. Mountziaris: for being on my committee, and moreover, always making themselves available for scientific and career advice.

Yannis G. Kevrekidis, Avadh Saxena, and Laurette S. Tuckerman: for scientific advising.

Floyd Williams: for moral and scientific advising.

all other collaborators: for the collaborations.

all my friends: for being friends.

Finally, I would like to express my gratitude to the Mathematics Department at the University of Massachusetts and the financial support of P.G. Kevrekidis under grants NSF-DMS-0505665 and 0349023.

ABSTRACT

EXISTENCE, STABILITY, AND DYNAMICS

OF SOLITARY WAVES IN

NONLINEAR SCHRÖDINGER MODELS

WITH PERIODIC POTENTIALS

FEBRUARY 2010

KODY J. H. LAW, B.S., UNIVERSITY OF MASSACHUSETTS

AMHERST

M.S., UNIVERSITY OF MASSACHUSETTS AMHERST

Ph.D., UNIVERSITY OF MASSACHUSETTS AMHERST

Directed by: Professor Panayotis G. Kevrekidis

The focus of this dissertation is the existence, stability, and resulting dynamical evolution of localized stationary solutions to Nonlinear Schrödinger (NLS) equations with periodic confining potentials in 2(+1) dimensions. I will make predictions about these properties based on a discrete lattice model of coupled ordinary differential equations with the appropriate symmetry. The latter has been justified by Wannier function expansions in a so-called tight-binding approximation in the appropriate parametric regime. Numerical results for the full 2(+1)-D continuum

model will be qualitatively compared with discrete model predictions as well as with nonlinear optics experiments in optically induced photonic lattices in photorefractive crystals. The predictions are also relevant for BECs (Bose-Einstein Condensates) in optical lattices.

TABLE OF CONTENTS

LIST OF FIGURES

CHAPTER 1

INTRODUCTION

1.1 Introduction

Nonlinear partial differential and difference equations with localized solutions are prevalent throughout the applied sciences, serving as appropriate models for a vast array of phenomena. Among such models, the NLS, in both its differential difference form [1] and in its partial differential form [2], has been very popular recently because of its success in modeling a wide variety of physical systems ranging from atomic physics, in the dynamics of Bose-Einstein condensates [3, 4], to condensed matter and nonlinear optics in the dynamics of optical fibers [5, 6], waveguide arrays [8] and photonic crystal lattices [7]. The interplay of discreteness and nonlinearity there led to the emergence of numerous phenomena that have gathered considerable attention subsequently, such as Peierls-Nabarro potential barriers, diffraction and diffraction management [9] and gap solitons [10], to name just a few. See, for example, the reviews [11, 12] and references therein.

In particular, with recent advances in optical technology and emergence of the analog of the semiconductor in optics, i.e. photonic bandgap [7] material, research interest in the area of nonlinear optics of periodic media has increased and the NLS model in this context is one which has had a significant amount of success.

More recently, there has been growing interest within nonlinear optics in the area of optically-induced photonic lattices in photorefractive crystals such as strontium barium niobate

($Sr_xBa_{1-x}NbO_3$, commonly abbreviated SBN). The original theoretical proposal of [13] was followed quickly by experimental realizations [14], and the foundation was thus set for the observation of a diverse array of novel nonlinear phenomena in this setting. Among others, these phenomena include dipole [15], multipole [16, 17], necklace [18], gap [10] and rotary [19] solitons as well as discrete [20] and gap [21] vortices, higher order Bloch modes [22], Zener tunneling [23], as well as localized modes in honeycomb [24], hexagonal [25] and quasi-crystalline [26] lattices, and Anderson localization [27] (see [28, 29] for additional examples). A considerable effort along these lines has been dedicated to the recently emerging area of *non-square* lattices [24, 30, 25, 31, 32, 33, 34, 35, 36]. Furthermore, the majority of these studies have dealt with the case of a focusing non-linearity rather than a defocusing one. Coherent structures in the latter case have received relatively limited attention until very recently, for example in the study of fundamental and higher order gap solitons [14, 21]. More complicated gap structures, such as multipoles and complex valued vortices are only starting to be explored in square lattices [37, 38]. A theoretical framework has been developed in parallel to this work, stemming from one-dimensional and square lattices [39, 12, 1]. However, the predictions of the latter can also be translated to contours (or paths) in non-square geometries [35, 36], based on arguments of dimensionality reduction along the contour. Knowledge of the accurate linear spectrum in these models as well as the existence, stability and dynamics of the localized solutions having energies in its complement (i.e., the photonic bandgap) provides invaluable insight. This dissertation contributes in this direction with the study of such models with defocusing nonlinearity as

well as non-square lattice geometry [including triangular (6-neighbor), honeycomb (3-neighbor), and Kagomé (more exotic lattice)] which have both recently been experimentally realized by our collaborators. See [37, 38] and [40] for first examples. For the stability predictions, the evolution scales of current experiments in the propagation direction are still inadequate for conclusive confirmation.

The full model of a continuous domain with a periodic potential is first reduced to the analogous discrete model of coupled oscillators, one for each well of the lattice. Qualitative predictions are obtained for the existence and linear stability of particular configurations of closed contours of excited nodes via expansion from the exactly solvable anticontinuum (i.e. uncoupled) limit. These structures consist of real-valued fields, such as monopoles, dipoles, and multi-poles as well as complex ones with relative phase across a contour summing to some multiple of 2π - this multiple is referred to as the topological charge of the corresponding vortex structure. The theoretical predictions are confirmed with a systematic numerical analysis of the discrete system of ODEs. This consists of identifying continuations of solutions in the coupling parameter from the anticontinuum limit and computing the spectrum of the linearization operator around each one. A positive real part in the spectrum then signifies instability. When unstable, the dynamical system is perturbed and evolved dynamically in order to observe the actual evolution of the instability and subsequent dynamics. Next, the predictions from the discrete model are tested against a full numerical approximation to the continuum setting of a 2(+1)-D nonlinear wave packet evolving in a periodic medium. The system typically emulates a photorefractive crystal with anisotropic refractive index in the planar and normal to the plane directions. The effect of the anisotropy is that the electric field of a pulse with polarization normal to the plane propagates nonlinearly while waves which are polarized in the planar direction propagate linearly.

By interfering such plane waves one can generate an effective optical lattice external potential for the nonlinearly propagating pulse. Such optical lattices can be constructed with a variety of different inherently 2-D symmetries, such as square, honeycomb, hexagonal, and Kagomé. The appropriate model for the nonlinear pulse propagation is an NLS equation with a periodic external potential and saturable nonlinearity [13]. I construct a system of ODEs that numerically represent the solution at selected points in the continuous domain. The investigation of the NLS consists of first locating the accurate spectrum (and, hence, band-gaps) of the linearized operator (around the zero solution) and then identifying families of solutions that are contours of localized structures analogous to those of the discrete model predictions for energies within the band-gaps. Subsequently, I linearize around each solution of the continuum and identify the dominant eigenvalues, whose real parts then determine the growth rates of infinitesimal perturbations. I qualitatively compare these linear stability results with the predictions of the discrete model. Then the system of ODEs is evolved in time in order to confirm the linear stability analysis and study the dynamics.

Finally, the numerical results are compared to experiments being done with actual anisotropically biased photorefractive Strontium Barium Niobate ($Sr_xBa_{1-x}Nb)O_3$, commonly abbreviated SBN) crystals by the group of Zhigang Chen at the Department of Physics and Astronomy at San Francisco State University and the Key Laboratory of Weak-Light Nonlinear Photonics at TEDA Applied Physics School at Nankai University, as well as the group of Yuri Kivshar at the Nonlinear Physics Centre in the Research School of Physical Sciences and Engineering at Australian National University, and the group of Cornelia Denz at the Institut für Angewandte Physik and Center for Nonlinear Science (CeNoS), at Westfälische Wilhelms-Universität in Münster, Germany.

1.2 Preliminaries

We introduce the following complex-valued non-linear evolution equation for the amplitude of the electric field U [41, 42],

$$-iU_z = [\mathcal{L} + \mathcal{N}(\mathbf{x}, |U|^2)]U, \tag{1.1}$$

where U is a function of $z \in \mathbb{R}_+$ and $\mathbf{x} \in \mathbb{Z} \times \mathbb{Z}$ in the discrete version or else $\mathbf{x} \in \mathbb{R} \times \mathbb{R}$ in the continuum version.

1.2.1 Discrete

First, we will consider the discrete version with

$$\mathcal{L}_\varepsilon = \varepsilon \left(\sum_{j \in \{G\}} \mathbf{e}_j - |G| \right), \tag{1.2}$$

where $\mathbf{e}_j$ is a translation by one site in some direction from the set of neighboring directions G of the discrete lattice, $|G|$ is the number of such directions and ε is the coupling between sites. The non-linear term is typically taken to be a cubic Kerr non-linearity as follows

$$\mathcal{N}(\mathbf{x}, |U|^2) = -s|U|^2. \tag{1.3}$$

where $s > 0$ corresponds to a defocusing nonlinearity and $s < 0$ corresponds to a focusing nonlinearity.

1.2.2 Continuum

The continuum version consists of defining $\mathcal{L} = D\nabla^2$, where ∇^2 is the two-dimensional Laplacian on $\mathbb{R} \times \mathbb{R}$ and

$$\mathcal{N}(\mathbf{x}, |U|^2) = \frac{E_0}{1 + I(\mathbf{x}) + |U|^2}, \tag{1.4}$$

with

$$I(\mathbf{x}) = I_0 \left| \sum_{j=1}^{N} e^{ik\mathbf{b}_j \cdot \mathbf{x}} \right|^2 \tag{1.5}$$

the optical lattice intensity function formed by N interfering lattice beams in the principal directions $\mathbf{b}_j$ with periodicity $2\pi/k$.

Here I_0 is the lattice peak intensity, z is the propagation constant and $\mathbf{x} = (x, y)$ are transverse distances (normalized to $z_s = 1\text{mm}$ and $x_s = y_s = 1\mu\text{m}$), E_0 is proportional to the applied DC field voltage ($E_0 > 0$ corresponds to a defocusing nonlinearity, while $E_0 < 0$ corresponds to a focusing nonlinearity), $D = z_s\lambda/(4\pi n_e x_s y_s r_{3,3})$ is the diffraction coefficient, λ is the wavelength of the laser in a vacuum, $r_{3,3}$ is the d is the periodicity in the x-direction and n_e is the refractive index along the extraordinary axis. The non-dimensional dispersion coefficient D is equivalent to rescaling space by a factor $\sqrt{D}$.

1.3 Existence considerations

Assuming a standing wave of u exists in the form $e^{-i\mu z}$, and letting the propagation constant $-\mu$ represent the (nonlinear) real eigenvalue of the operator of the righthand side of Eq. (1.1), the corresponding eigenvector u is a fixed point of

$$[\mu + \mathcal{L} + \mathcal{N}(\mathbf{x}, |u|^2)]u = 0. \tag{1.6}$$

1.3.1 Discrete

In the discrete case, we perform continuations in ε. In particular, if one indexes the sites by (m, n), then solutions in the limit $\varepsilon \to 0$ can easily be found of the general form $u_{m,n} = \sqrt{\mu}\exp\{-i(\mu t - \theta_{m,n})\}$ for any arbitrary $\theta_{m,n} \in [0, 2\pi)$ [12]. We can linearize Eq. (1.6) around the solution for $\varepsilon = 0$ denoted by u_0, accounting for complex valued perturbations by considering the conjugate of Eq. (1.6) as well, which has the solution u_0^*. The *Jacobian* of (1.6) as a function for fixed ε is

$$\mathcal{J}_\varepsilon(u) = [\mu + \partial(\mathcal{N}u, [\mathcal{N}u]^*)/\partial(u, u^*)] + \begin{pmatrix} \mathcal{L}_\varepsilon & 0 \\ 0 & \mathcal{L}_\varepsilon \end{pmatrix}. \tag{1.7}$$

We may also take the coupling ε, when sufficiently small, as the small parameter in the expansion with $[u, u^*]^T = [u_0, u_0^*]^T + \varepsilon u_1$. The first order correction in ε to Eq. (1.6) is then

$$\mathcal{J}_0(u_0)u_1 + \tfrac{1}{\varepsilon} \begin{pmatrix} \mathcal{L}_\varepsilon & 0 \\ 0 & \mathcal{L}_\varepsilon \end{pmatrix} \begin{pmatrix} u_0 \\ u_0^* \end{pmatrix} = 0.$$

Projecting this map onto the kernel of $\mathcal{J}_0(u_0)$ eliminates the first term and we are left with the condition

$$\left\langle \begin{pmatrix} \mathcal{L}_\varepsilon & 0 \\ 0 & \mathcal{L}_\varepsilon \end{pmatrix} \begin{pmatrix} u_0 \\ u_0^* \end{pmatrix}, \ker\{\mathcal{J}_0(u_0)\} \right\rangle = \mathbf{0},$$

where we use $\langle \cdot, \cdot \rangle$ to denote the standard inner product on the Hilbert space l^2 and $\mathbf{0}$ is the zero vector with the same dimension as the kernel. We let $\mu = 1$

without loss of generality (here and for the rest of this work, in the discrete cases) and denote by j the indices (m, n) along the one-dimensional contour. The nontrivial part of the Jacobian $\mathcal{J}_0(u_0)$ decouples into a direct sum of N 2×2 blocks if there are N excited sites in the contour. For each j there is a nontrivial element $(e^{i\theta_j}, -e^{-i\theta_j})^T \in \ker\{\mathcal{J}_{0,j}(u_0)\}$. So, the condition for existence of solutions to Eq. (1.6) with $\varepsilon > 0$ reduces to the vanishing of the vector function $\mathbf{g}(\boldsymbol{\theta})$ of the phase vector $\boldsymbol{\theta} = (\theta_1, \ldots, \theta_N)$ where

$$g_j \equiv (\sin(\theta_{j-1} - \theta_j) + \sin(\theta_{j+1} - \theta_j)), \tag{1.8}$$

subject to periodic boundary conditions. We consider primarily contours M within the subcategory of those for which $|\theta_{j+1} - \theta_j| = \Delta\theta$ is constant for all $j \in M$, $|\theta_1 - \theta_{|M|}| = \Delta\theta$ and $\Delta\theta|M| = 0 \mod 2\pi$. A standard Newton fixed-point solver will be used to construct branches of solutions to Eq. (1.6) in ε from the AC limit.

1.3.2 Continuum

For the continuum problem where $\mathbf{x} \in \mathbb{R}^2$, there exists no such analytical solution from which to construct a continuation. On the other hand, it is well-known that localized solutions exist for values of the propagation constant μ in the complement of the linear spectrum (i.e. the so-called spectral gap) defined by the following eigenvalue problem (also known as the linearization around the zero solution),

$$[\mu - \mathcal{L} - \mathcal{N}(\mathbf{x}, 0)]u = 0. \tag{1.9}$$

These solutions are exponentially localized in space, so-called gap-soliton, states of the original nonlinear partial differential equation. They may reside either in the so-called semi-infinite gap for focusing nonlinearities ($E_0 < 0$) or else in a higher

gap beyond the first band of linear eigenvalues, μ, for defocusing nonlinearities ($E_0 > 0$) Since the parameter of interest is μ, diagnostics are plotted against μ. Continuations in this parameter can be found with a fixed-point solver and an initial guess of a collection of Gaussian wave-packets in the appropriate configuration. Using a standard eigenvalue solver package implemented through MATLAB, we will identify the spectral bands.

The localized states u of the continuum version of Eq. (1.6) were obtained using the Newton-Krylov fixed point solver nsoli from [43], which utilizes a GMRES iterative algorithm, based on residual reduction in successive Krylov subspaces, in order to minimize the memory necessary for the linear solver within each step of the Newton algorithm. Again, as with the discrete version, there are various numerical approaches (see the appendix A). Some care has to be taken to handle the large size of the representation of a 2D continuum domain. A pseudo-arclength continuation [44] will be used to follow each branch and locate the bifurcations which occur at the edges of the bands.

The square root of the optical power of the localized waves is defined as follows:

$$P = ||U||_{\mathrm{L}^2} = \left[\int |U|^2 \, dS\right]^{1/2}, \tag{1.10}$$

where in the continuum problem, $dS = dxdy$ (i.e. the L^2-norm), while in the discrete problem we define $dS = \delta_{m,n}/\sqrt{\varepsilon}$ with $\delta_{m,n}$ the Kronecker delta function at the lattice node indexed by (m, n), i.e. the weighted l^2-norm.

1.4 Stability considerations

Stability is examined by linearizing Eq. (1.1) and its conjugate around an exact stationary solution $(u, u^*)^T$ to Eq. (1.6). If we assume the perturbation is separable of the form $\tilde{u} = e^{\lambda t} w(x)$, then we have the following eigenvalue problem for $i\lambda$ (commonly referred to in atomic physics as the Bogoliubov De-Gennes system)

$$\{i\lambda I_2 + \sigma\left[\mathcal{J}_\varepsilon(u)\right]\} v = 0, \tag{1.11}$$

where

$$\sigma = \begin{pmatrix} I & 0 \\ 0 & -I \end{pmatrix}, \tag{1.12}$$

$\mathcal{J}$ is defined in Eq. (1.7), (ε has no meaning in the continuum version) and I_2 is identity matrix of twice the dimension of the solution. The eigenvalue problem imposes no restriction on the eigenvectors v. This form of the Jacobian is identical for the discrete and continuum versions of the problem, up to the definitions of the operators $\mathcal{N}$ and $\mathcal{L}$ and the domain in which the spatial variables live. The modest size of this matrix for the discrete version of the problem will not pose a problem for a full diagonalization and we will implement the MATLAB function **eig** to do so. On the other hand, the matrix for the model of the continuous domain will be considerably larger (by at least an order of magnitude) and cannot be inverted. Fortunately a standard finite difference discretization leads to a sparse banded matrix which is perfectly suited for Arnoldi iterative algorithms which minimize memory and use successive approximations of eigenvalues and eigenvectors until convergence. Such a method is implemented by the MATLAB function **eigs**, which we use here.

Twofold symmetry over each the real and imaginary axes is guaranteed by the

fact that the Jacobian of the full problem, which defines the linearization at any point, H, has the property that $JHJ = H^T$ (where J is the canonical symplectic matrix having the properties $JJ = -I$ and $JJ^T = I$), which implies $e^H = Q$ is *symplectic* or $Q^T JQ = J$, and so $\mathrm{Re}(\lambda_j) \neq 0$ implies an instability.

In the discrete case, the stability will be compared to analytical results for small ε based on Lyapunov-Schmidt analysis of the expansion of the equation around the AC limit (see, e.g. [12] and references therein for details). For the contour M, there are $|M|$ eigenvalues γ_j of the $|M| \times |M|$ Jacobian $\mathcal{M}_{jk} = \partial g_j / \partial \theta_k$ of the diffeomorphism given in Eq. (1.8). Now, for each excited site, there are a zero and a negative eigenvalue of $\{\mathcal{J}_0(u_0)\}$, which are both mapped to zero eigenvalues of $\sigma\mathcal{J}(u_0)$. So, one can follow the same procedure for the eigenvalue problem of the linearization (Eq. 1.11) of the original problem, except projecting also onto the generalized kernel and expanding to lower order ($\sqrt{\varepsilon}$) and, hence, obtain a mapping between its eigenvalues and those of the Jacobian of $\mathbf{g}$. In particular, for each eigenvalue γ_j of $\mathcal{M}$, the full linearization around a stationary solution with non-zero nodes in M, given by Eq. (1.11), will have an eigenvalue pair λ_j given, to leading order, by

$$\lambda_j = \pm\sqrt{2\gamma_j\varepsilon} \tag{1.13}$$

in the case that the sites in M are nearest neighbors of each other. If the excited nodes are separated by a site then, for the DNLS model eigenvalues, ε is replaced by ε^2 in the previous relation. The Jacobian matrix $\mathcal{M}$ has the following form:

$$(\mathcal{M})_{j,k} = s$$
$$\begin{cases} -\cos(\theta_{j+1} - \theta_j) - \cos(\theta_{j-1} - \theta_j), & j = k, \\ \cos(\theta_j - \theta_k), & j = k \pm 1, \\ 0, & |k - j| \geq 2. \end{cases} \tag{1.14}$$

We now briefly discuss the principal stability conclusions. In the presence of a focusing nonlinearity out-of-phase excitations are predicted to be stable, while in-phase excitations are expected to be unstable. For a solution u_f of the focusing problem, the configuration $u = (-1)^{\sum_{j=1}^{d} n_i} u_f$, in d dimensions, with n_j indexing the j^{th} dimension, is a solution of the focusing problem, in a square lattice [39]. This transformation, known as the staggering transformation, implies that the in-phase nearest neighbor configuration in the defocusing case corresponds to an out-of-phase such configuration in the focusing case and should thus be stable [12]. On the other hand, next nearest neighbor out-of-phase defocusing configurations would correspond to next nearest neighbor out-of-phase focusing configurations and should also be stable (at least close to the anticontinuum limit). By the same token, out-of-phase nearest neighbor, and in-phase next nearest neighbor structures should be unstable. This consideration covers all real-valued solutions, and implies that if ever there are 2 neighbors leading to an instability, the configuration will be unstable, while if all neighbors should be stable, then we expect stability. However, notice that, as discussed in [39], multipole structures characterized as potentially stable above will, in fact, typically possess imaginary eigenvalues of negative Krein signature (see e.g. [45] and references therein). These may lead to oscillatory instabilities through complex quartets of eigenvalues, which arise by means of Hamiltonian-Hopf (HH) bifurcations [46] emerging from collisions of these eigenvalues of negative Krein signature with eigenvalues of positive Krein signature.

These conclusions will be discussed in connection with our detailed numerical results.

The results will be organized as follows. In Chapter 2 we will apply this methodology in the investigation of the defocusing case in a square lattice. The discrete model predictions have been previously confirmed numerically in a truly discrete domain in [39] and we will proceed to confirm the qualitative existence and stability results in a continuum setting relevant to nonlinear optics systems in photorefractive crystals with a saturable nonlinearity as well as investigate the dynamical evolution of the unstable configurations. Finally, the numerical results will be compared with experiments of saturably nonlinear evolution of optical wave-packets in photorefractive crystals with photonic lattices of the appropriate geometry. In Chapter 3 we will first extend the discrete results from the square lattice to hexagonal (six-neighbor) as well as honeycomb (three-neighbor) lattices, with a thorough study of existence, stability, and dynamics of typical 1D contour configurations therein. Then, in Chapter 4 we will extend these results again to the continuum setting with a saturable nonlinearity relevant to experiments in nonlinear optics, investigating the honeycomb lattice with a defocusing nonlinearity and some particularly interesting configurations with non-trivial current in the focusing version. These results will again be compared with experiments in photorefractive crystals with external bias and a photonic lattice of the appropriate geometry. Finally, in Chapter 5, the procedure from the previous chapters will be repeated in an abridged version for the case of the more exotic kagomé lattice with a defocusing nonlinearity. These results have not yet been compared with actual experiments.

CHAPTER 2

SQUARE LATTICE

2.1 Setup

Here the diffusion coefficient will be normalized by the spatial rescaling $\mathbf{x} \to \sqrt{D}\mathbf{x}$, such that the diffusion coefficient is effectively 1. The external potential, in units of I_d (the dark irradiance of the crystal) is

$$I = I_0 \cos^2\left(\frac{x+y}{\sqrt{2}}\right)\cos^2\left(\frac{x-y}{\sqrt{2}}\right). \tag{2.1}$$

Furthermore, the units of the propagation distance, z, will be $2k_0 n_e d^2/\pi^2$, and the transverse distances, (x, y), will be in units of d/π, where d is the lattice spacing, $k_0 = 2\pi/\lambda_0$ is the wavenumber of the laser in the vacuum, λ_0 is the wavelength, and n_e is the refractive index along the extraordinary axis. In line with our experiment, we choose the lattice intensity $I_0 = 5$ (in units of I_d). A plot of the optical lattice is shown in Figure 1, also for illustrative purposes regarding the location where our localized pulses will be "inserted". In addition, we choose other physical parameters consistently with the experiment as

$$d = 25\ \mu\text{m}, \quad \lambda_0 = 0.5\ \mu\text{m}, \quad n_e = 2.3, \quad r_{33} = 280\ \text{pm/V}.$$

Thus, in this chapter, one x or y unit corresponds to 7.96 μm, one z unit corresponds to 3.66 mm, and one E_0 unit corresponds to 12.76 V/mm in physical units. In the

experiments, the applied voltage is -550V/5mm, which gives $E_0 = 8.62$ in our numerical simulations.

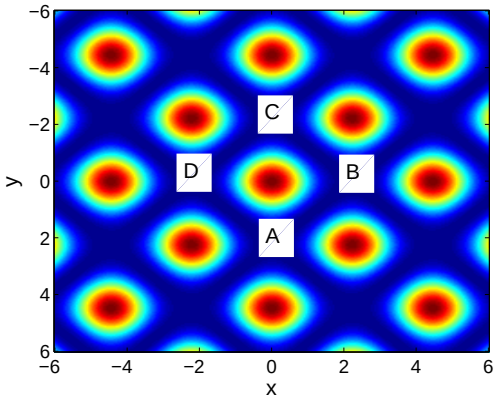

Figure 1. A spatial $(x - y)$ contour plot of the ordinary polarization standing wave [lattice beam in Eq. (1.1)]. The localized pulses will be sitting at the minima of the lattice field, as opposed to the focusing nonlinearity lattice field, where they reside at the maxima. Points A, B, C, and D are used for naming the dipole configurations. A is a nearest-neighbor minimum of B and D (in our "diagonally-oriented" lattice), while it is a next-nearest-neighbor of C. Because of that, dipoles whose two lobes are at A and B (or at C and D) will be called nearest-neighbor dipole solitons. The ones that are sitting at A and C (or at B and D) will be called next-nearest-neighbor dipoles.

It should also be noted here that in our experimental results the diffraction length can be approximately evaluated (for the beam widths and wavelengths that we typically used) as being 2.5mm. As our crystal extends over 10mm in the z-direction, it is clear that the patterns that we observe are over a few (roughly 4) diffraction lengths and hence if they are self-supported within such length scales, this will indicate that they are indeed self-trapped beams. On the other hand, as we will see in what follows (in our numerical simulations), for all the configurations that we will find to be unstable, the instability development will arise typically for

dimensionless propagation distances of $10 < z < 100$. Since these distances are considerably longer (in dimensional units) than the propagation distance in our crystal, all of the patterns presented in Sections 3-5 below (even the most unstable ones) should, in principle, be experimentally observable in our setting. This is corroborated by our experimental results in Section 6.

The numerical simulations are done with a uniform spatial mesh with $\Delta x = 1/3$ and domain size 30×30, i.e. 91×91 grid points for most configurations (see Figure 1 for a schematic of the spatial configurations). For some of the configurations, a larger domain was required, in which case a domain of size 60×60, i.e. 181×181 grid points, was used. Regarding the typical dynamics of a soliton when it is unstable, we simulate the z-dependent behavior using a Runge-Kutta fourth-order method with a step $\Delta z = 0.00025$.

Stationary solutions of Eq. (1.1) are sought in the form of $U(x, y, z) = u(x, y)e^{i\mu z}$, where μ is the propagation constant and u is a function satisfying

$$\mu u - (u_{xx} + u_{yy}) - \frac{E_0}{1 + I_{ol} + |u|^2} u = 0. \tag{2.2}$$

The localized states $u(x, y)$ of (2.2) were obtained using the Newton-GMRES fixed point solver nsoli from [43] and continuation was used as a function of μ, to follow the relevant branches of solutions.

The propagation constant μ we consider in this report is in the first spectral gap [1]. Using Hill's method for the 2D problem [47], for parameter values mentioned above, we find the band gap to be $4.2 \lesssim \mu \lesssim 5.46$ [2] .

[1] It is necessary that propagation constants are outside of the semi-infinite gap for solutions with defocusing nonlinearity.

[2] We note that the linear spectrum for μ quoted here and shown in the following images was the most accurate we computed using Hill's method based on consistency over Δx in the limit $\Delta x \to 0$. The linear spectrum for the discretized problem with our chosen discretization is slightly different however, and in particular, the first band edge occurs at a slightly larger value of μ. It

	NN Stability	NNN Stability
IP Dipole	Stable ($N_i^- = 1$)	Unstable ($N_r = 1$)
OOP Dipole	Unstable ($N_r = 1$)	Stable ($N_i^- = 1$)
IP Quadrupole	Stable ($N_i^- = 3$)	Unstable ($N_r = 3$)
OOP Quadrupole	Unstable ($N_r = 3$)	Stable ($N_i^- = 3$)

Table 2.1. Summary of the stability results of the discrete model with defocusing cubic nonlinearity, studied in [39], for all the in-phase (IP) and out-of-phase (OOP), nearest-neighbor (NN), as well as next-nearest-neighbor (NNN) configurations. N_r denotes real eigenvalue pairs and N_i^- denotes imaginary eigenvalue pairs with negative Krein signature.

At this point, it is also relevant to list the results of the *discrete* NLS defocusing model of [39] that we will use for comparison with the findings below. These results are incorporated in Table 1, where the stability of all the possible combinations of in-phase and out-of-phase, nearest-neighbor and next-nearest-neighbor configurations is quantified in terms of their relevant eigenvalues of linearization. The configurations are dubbed unstable when they possess (for all parameter values) real eigenvalue pairs, whereas they are considered marginally stable, when they do not always have such pairs. However, the latter configurations typically, in this setting, possess imaginary eigenvalues with negative Krein signature (see e.g. [45] and references therein), which practically means that if these collide with other eigenvalues, as μ is varied, complex eigenvalue quartets will emerge out of Hamiltonian-Hopf bifurcations [46], destabilizing the relevant solution. Hence, such solutions are not *always* linearly unstable, but *may become* unstable for some parameter ranges.

is interesting to note that all saddle-node bifurcations occur near the accurate band edge, while those solutions which degenerate to linear Bloch modes actually degenerate beyond this value at the band edge particular to the discretization (not shown).

2.2 Dipoles

For dipole solutions, we consider both in-phase (IP) and out-of-phase (OP) configurations for both nearest (N) neighbor and next-nearest (NN) neighbor configurations.

2.2.1 Nearest-neighbor Dipole Solitons

In this section, we report dipole solitons where the two lobes of the wave are located in two nearest-neighbor (N) lattice sites in the 2D square lattice potential shown in Figure 1. The lobes can have the same phase or π phase difference and are, accordingly, hereafter termed in-phase (IP) dipoles and out-of-phase (OP) dipoles, respectively. Notice that due to the (diagonal) nature of our lattice, the nearest-neighbor configurations that we consider are "built" along the diagonal direction; see Figure 1.

We have found IP dipoles in a large interval of propagation constants μ for the given voltage E_0. We found that the solitons exist for μ smaller than 5.46, or for peak intensities larger than 0.144. We note that the intensity of the dipoles cannot be arbitrary low, a result similar to the observed results of the focusing case [15, 42]. The relevant findings are summarized in Figure 2.

The top left panel of Figure 2 shows the stability of the dipoles as a function of the propagation constant μ, by illustrating the maximal growth rate (maximum real part over all perturbation eigenvalues) of perturbations. When $\max(\mathrm{Re}(\lambda)) = 0$, this implies stability of the configuration, while the configuration is unstable if $\max(\mathrm{Re}(\lambda)) \neq 0$ in this Hamiltonian system. We found that the stability region of this type of dipoles is given by $4.2 \lesssim \mu \lesssim 4.91$, the left hand limit corresponding to the Bloch band. The top right panel depicts the peak intensity and the power

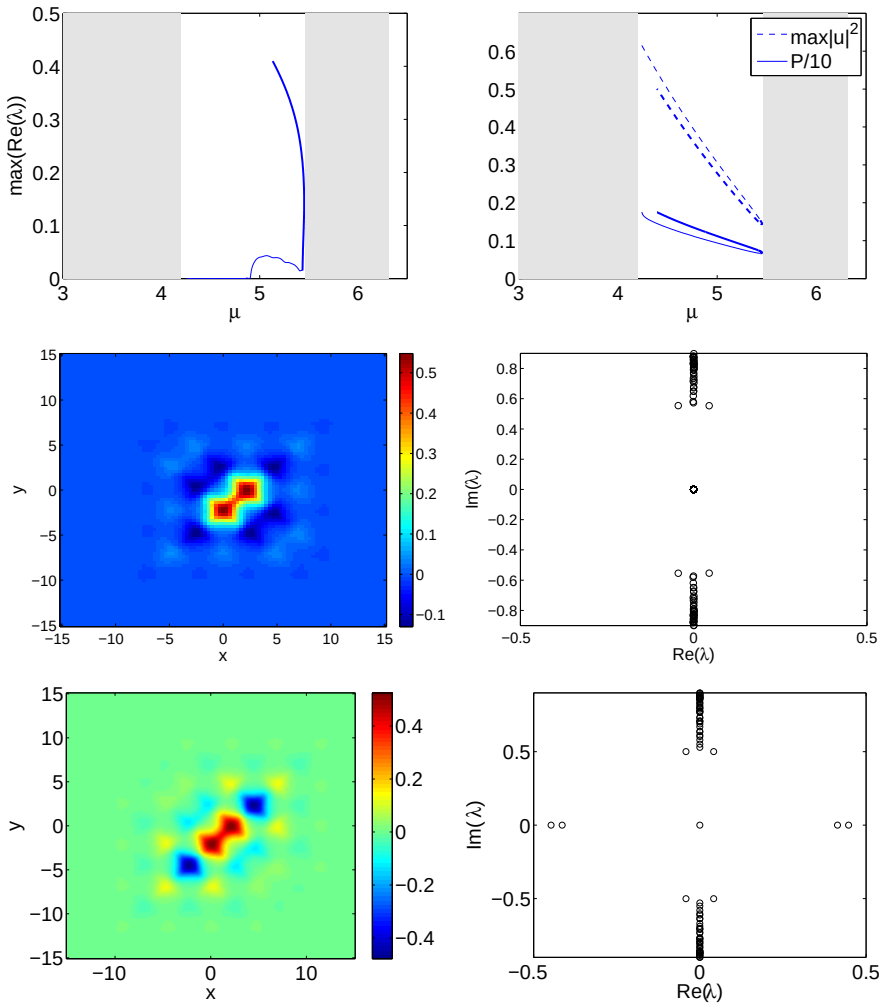

Figure 2. The top left panel shows the stability of the dipoles as a function of the propagation constant μ. It is stable when the spectra is purely imaginary (i.e., when $\max(\mathrm{Re}(\lambda)) = 0$). The top right panel depicts the peak intensity and the power of the dipoles. The thin line corresponds to the solution represented in the middle row, while the bold line corresponds to the waveform illustrated in the bottom row. These two branches of solutions collide and mutually annihilate in a saddle-node bifurcation. The shaded areas in both of these panels represent the bands of the periodic potential. The middle (resp. bottom) left and right panels show the profile u of the branch indicated by thin (resp. bold) line in the top row at $\mu = 5$ and the corresponding complex spectral plane $(\mathrm{Re}(\lambda), \mathrm{Im}(\lambda))$ of the eigenvalues $\lambda = \mathrm{Re}(\lambda) + i\mathrm{Im}(\lambda)$.

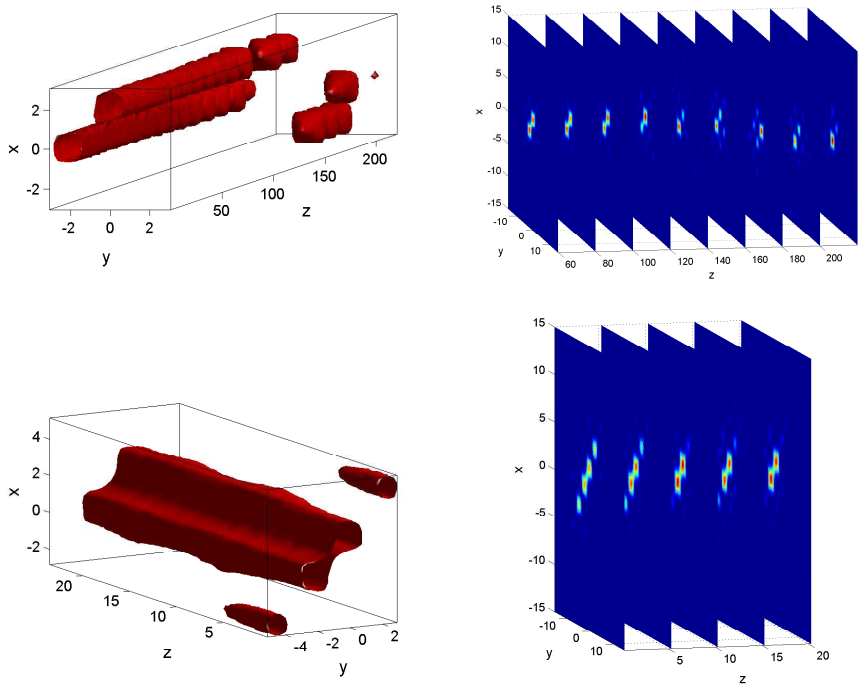

Figure 3. The evolution of the dipoles shown in Figure 2 perturbed by a random noise of maximum intensity 0.25% of the soliton peak intensity. Presented in the figure are the isosurfaces (left panels) of magnitude 0.2 for the first configuration (top panels) and of magnitude 0.1 for the second one (bottom panels) and their slices at some particular instances (right panels).

of the dipoles.

The middle left and right panels show the profile u of a dipole at $\mu = 5$ and the corresponding spectra at the complex plane, respectively. We see that the soliton is unstable due to an oscillatory instability. This is the typical instability in this case, in line with the discrete cubic model results. Clearly, there is an imaginary eigenvalue with negative Krein signature [45] which upon collisions with the continuous spectrum results in Hamiltonian-Hopf bifurcations and concomitant oscillatory instabilities.

As we increase μ further, the dipoles disappear in a saddle-node bifurcation. The bifurcation diagram is depicted in the top panels of Figure 2. At the bifurcation point, $dP/d\mu \to \infty$, as $\mu \to 5.46$, i.e., at the boundary of the first Bloch band. At this point, the IPN configuration collides with a configuration shown at the bottom panel of Figure 2 (where the two nearest-neighbors, along the axis of the dipole, of the two populated wells become out-of-phase with them) and disappears in a saddle-node bifurcation.

The corresponding profile and spectral plane for the saddle branch at $\mu = 5$ is shown in the bottom right panel of the same figure, illustrating the strong instability of the latter.

We have also simulated the dynamics of the solitary waves when they are unstable. In Figure 3 we present the evolution of the unstable dipoles shown in Figure 2. The dipoles are perturbed by a random noise with maximum intensity 0.25% of the soliton peak intensity. Shown in Figure 3 are the isosurfaces and the slices of the soliton along the propagation direction.

The dynamics of the soliton shown in the middle panel of Figure 2 is presented in the top panels of Figure 3. One can see that even with that strong perturbation, at $z = 100$ the soliton still resembles its initial configuration. Physically, this corresponds to a propagation distance of approximately 366 mm. This means that the instability is very unlikely to be observed in the photorefractive crystal lattice used in our experiments. For longer propagation distances, the oscillatory instability sets in and finally rearranges the dipole into a fundamental soliton type configuration principally centered around a single site.

For the dipole shown in the bottom panel of Figure 2, we present its dynamics as bottom panels of Figure 3. We found that the instability is strong as predicted above such that even after a relatively short propagation distance, the configuration

turns into the more stable solution of the IPN dipole branch. We did not present the further dynamics of the dipole, as it is similar to the upper panels.

We have also found OP dipoles arranged in nearest-neighboring lattice wells. We summarize our findings in Figure 4 where one can see that the solitons exist in the whole entire region of propagation constant μ in the first gap, $\mu \in (4.2, 5.46)$. This smooth transition indicates that the OOP NN dipole solitons emerge out of the Bloch band waves; see e.g. [48] and [49] for a relevant discussion of the 1D and of the 2D problem respectively, in the case of the cubic nonlinearity. Nonetheless, the OOP NN dipoles are typically unstable due to a real eigenvalue pair. Notice that this is in agreement with the prediction of the discrete model (as can be seen from Table 1).

As the branch merges with the band edge, we observe an interesting feature, namely that the configuration resembles that of a quadrupole with a π phase difference between two neighboring solitons, which we call $+-+-$ quadrupoles below. This can be an indication that these structures bifurcate out of the Bloch band from the same bifurcation point. We elaborate this further in our discussion of the quadrupole structures in section 5.

In Figure 5 we present the instability dynamics of an OPN dipole soliton perturbed by a similar random noise perturbation as in Figure 3. This type of dipole is typically more unstable than its IP counterpart, as is illustrated in the figure. In particular, in this example of unstable evolution even at $z = 10$, the instability already manifests itself. One similarity of the instability of OPN dipoles with that of the IPN ones is that the dipoles tend to degenerate to a single-site, fundamental gap soliton, which is stable in this setting. We note in passing that similar evolution results for dipoles and quadrupoles (but for short propagation distances) in the focusing case are discussed in [42].

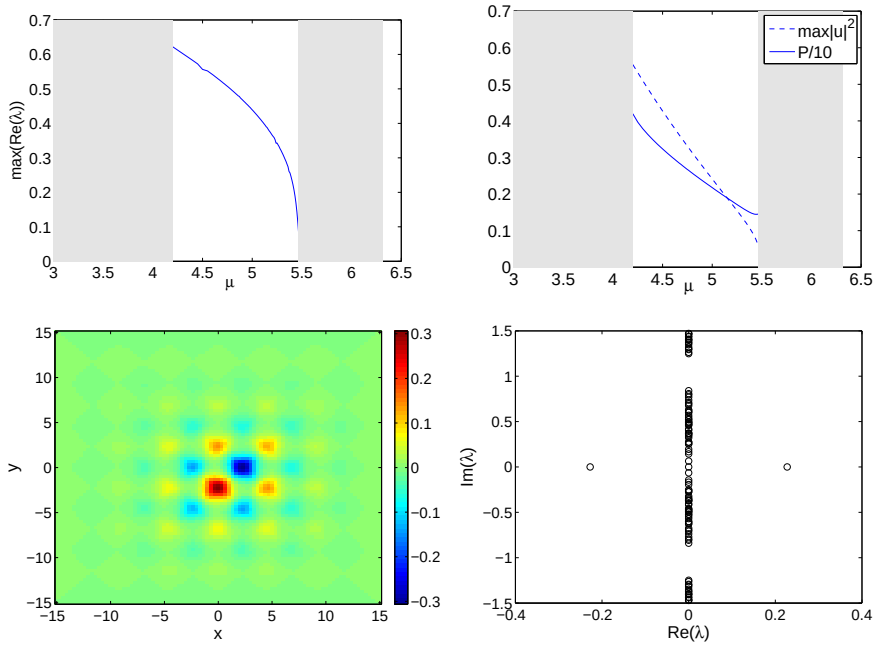

Figure 4. The top panels correspond to the same panels of Figure 2 but for OOP NN dipole solitons. The bottom panel shows the profile u and its spectrum in the complex plane for parameter value $\mu = 5.4$.

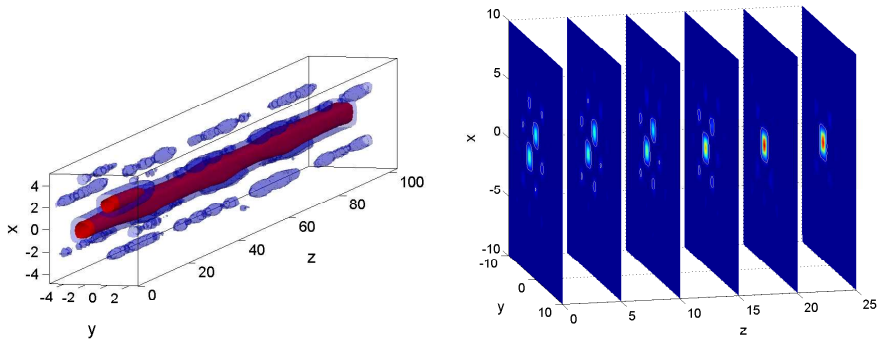

Figure 5. Similar to Figure 3 but for the evolution of OOP NN dipoles. Shown are the isosurfaces of height 0.05 (red) and 0.015 (blue) and the contour plot slices at some select propagation distances.

2.2.2 Next-nearest-neighbor Dipole Solitons

We have also obtained dipole solutions that are not oriented along the two nearest-neighboring lattice wells, but rather where the two humps of the structure

are located at two next-nearest-neighboring lattice sites. These humps can once again have the same phase or π phase difference between them. We will again use the corresponding IP and OP designations for these next-nearest-neighbor (NN) waveforms. Notice here that NN configurations that we consider are among the "closest" next-nearest-neighbor pairs, i.e., with the structures being aligned horizontally. In principle, one can consider more remote pairs of next-nearest-neighbors (e.g., along the diagonal), however the main qualitative stability properties discussed below would not change in such a case.

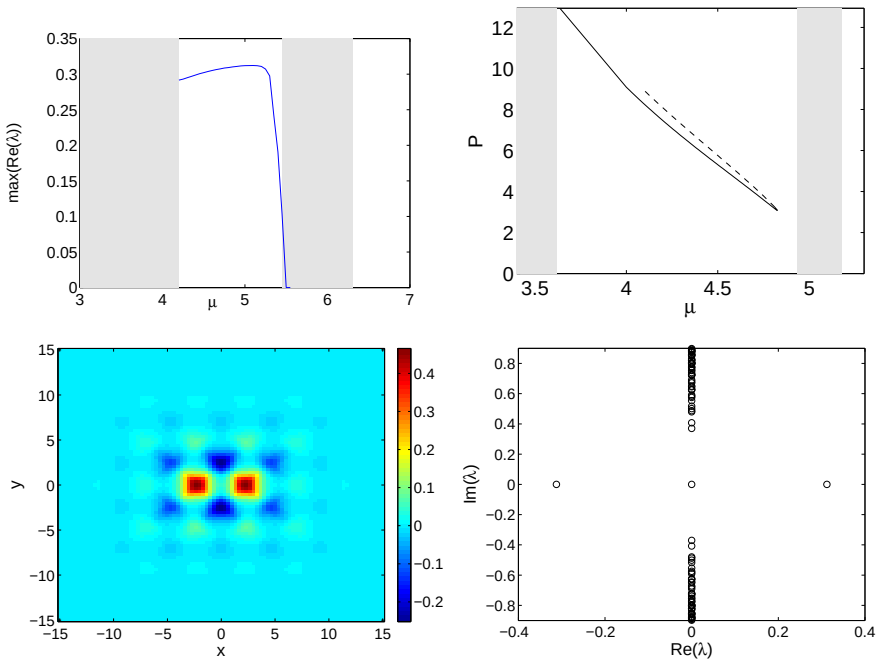

Figure 6. The top panels correspond to the same diagnostics as in Figure 2 but for IPNN dipole solitons. The bottom panels show the profile u and the spectral plane of the IPNN dipole at $\mu = 5.1$.

We have obtained this type of IPNN dipole solitons in a wide parameter range. The stability, the power and peak intensity of these dipoles are shown in Figure 6. These dipoles typically possess a real eigenvalue (again in line with the discrete

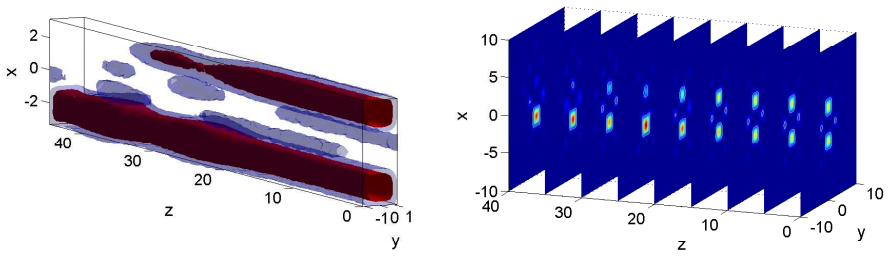

Figure 7. Similar to Figure 3 but for the evolution of the IP dipole shown in Figure 6. Presented are the isosurfaces of height 0.1 (red) and 0.05 (blue) and the sliced contours at some selected propagation distances.

cubic model prediction of Table 1).

If one compares these IPNN dipole solitons with the IPN dipole solitons of Figure 2, there are clear differences, such as the typical instability (with a real eigenvalue) of the former in contrast with the typical stability of the latter (possessing an imaginary eigenvalue of negative signature that can potentially become unstable upon collision with another eigenvalue). Another important difference is that the present IP dipoles emerge out of the Bloch band edges, contrary to what is the case for their IPN counterparts where the solitons disappear through a saddle-node bifurcation. Interestingly, as the branch approaches the upper band-edge, the profile of an IPNN dipole becomes similar to that of a $+-+-$ quadrupole (see section 5.1 below) and of an OPN dipole, as the relevant limit is approached.

In Figure 7, we present the dynamical evolution of the IPNN dipole shown in Figure 6 under similar random noise perturbation as above. Here, we also see that the instability appears earlier than the IPN dipoles. The two humps deform until they become one hump already at the propagation distance $z \approx 20$, transforming the dipole solution into a single-hump gap soliton.

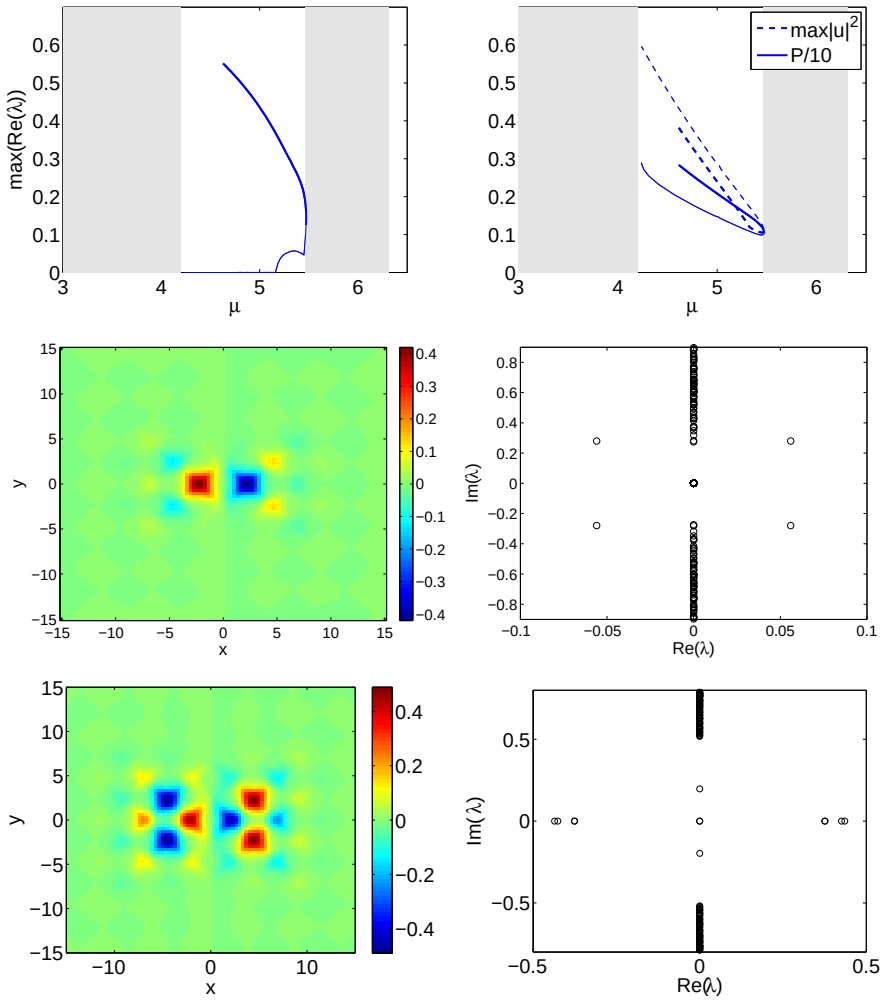

Figure 8. The top panels depict the largest real part of the critical eigenvalue, as well as the power and the peak intensity of the OPNN dipole solitons. The middle panels show the profile u and the corresponding spectra in the complex plane of the dipole at $\mu = 5.3$, and the bottom is the unstable saddle configuration, which collides with the OPNN profile in a saddle-node bifurcation, shown for $\mu = 5$.

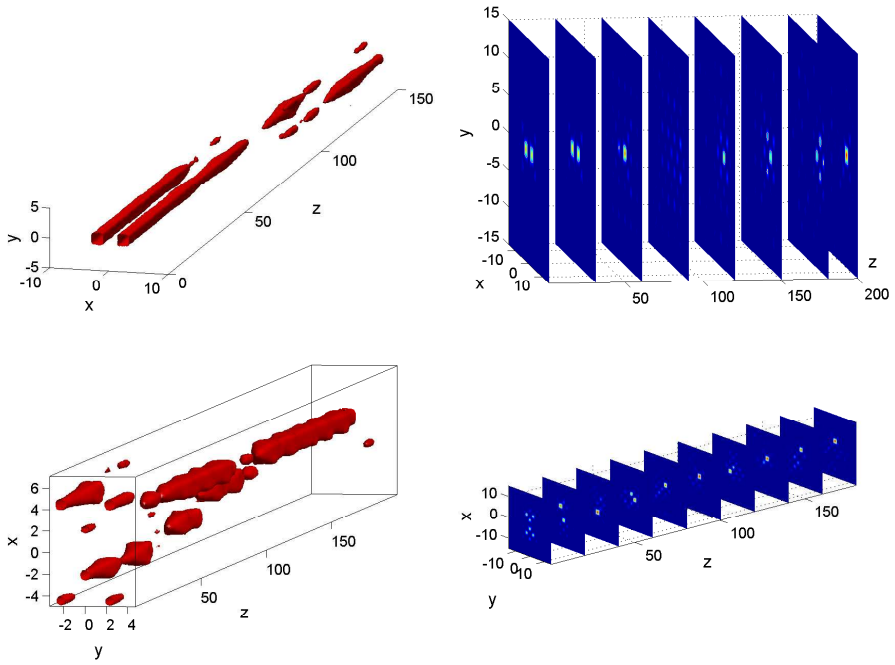

Figure 9. The evolution of the OPNN dipole and its corresponding counterpart for the same propagation constant μ, i.e. $\mu = 5.3$, shown in Figure 6. Presented are the isosurface of height 0.1 and the slices at particular propagation distances where one can see clearly that the light tunnels away from its initial lattice wells, eventually forming a single-site structure.

We have also obtained OPNN dipole solitons. A typical profile of this family of solutions for $\mu = 5.3$ is shown in Figure 8. The power diagram of these solitons is presented in the top panel of Figure 8. One important finding in this case is that there is a relatively wide stability region, i.e., typically these structures are stable (as indicated again by the comparison with the results of Table 1). We have found that the stability range for $E_0 = 8.62$ is $4.15 \lesssim \mu \lesssim 5.17$. This class of solutions typically suffers an oscillatory instability due to the presence of a single eigenvalue with negative signature and its collision with the continuous spectrum, as shown in the middle right panel of Figure 8 (c.f. once again with the discrete

model prediction of Table 1).

For this solution also, we observe that similarly to the IPN dipoles, it disappears at a non-zero peak intensity, in particular for $\max(|u|^2) \approx 0.11$. The disappearance is because of collision of this dipole with another configuration shown in the bottom panels of Figure 8 in a saddle-node bifurcation. It is relevant to note that the point of the bifurcation is very close to the edge of the Bloch band, i.e., for $\mu \approx 5.46$.

Subsequently, we simulate the dynamics of the instability and present it in Figure 9. One can see that for the OPNN, tunneling occurs during the propagation of the soliton along the z-direction, finally leading to localization at a well different from the original support of the dipolar structure. Regarding the counterpart solution of the other branch, the evolution along the z-direction is a bit different as there is no tunneling away from the original position. Yet, this configuration also leads to localization at a single site in its final configuration.

2.3 Quadrupoles

We now turn to the examination of quadrupolar structures with configurations having four lobes at four adjacent lattice wells. Such structures turn out to exist in a large parameter region as well. In particular, we will focus our discussion on the case of such nearest-neighbor quadrupoles.

Before we proceed with the discussion of our findings, we will explain the notations that we use for the quadrupole configurations. Since there are four humps with the phase difference between two neighboring wells being either 0 or π, we have four possible configurations (up to rotational and phase symmetries), i.e. $+-+-$, $+--+$, $++++$, and $+---$, where '+' and '-' represent the sign of the excitation of the main hump of u, i.e. whether it is positive (phase 0) or negative (phase π),

respectively, at the four excited sites A, B, C and D of Figure 1.

2.3.1 $+-+-$ Nearest-neighbor Quadrupole Solitons

First, we consider the $+-+-$ type. In Figure 10, we present a field profile of this structure for $\mu = 5$. We found that this configuration exists in the entire gap $\mu \in (4.2, 5.46)$, i.e., OPN quadrupoles also bifurcate from the edge of the Floquet band. Nonetheless, we observe that the instability of these structures involves 3 real eigenvalue pairs (two of which are coincident in the bottom right panel of Figure 10), in line with the predictions of Table 1.

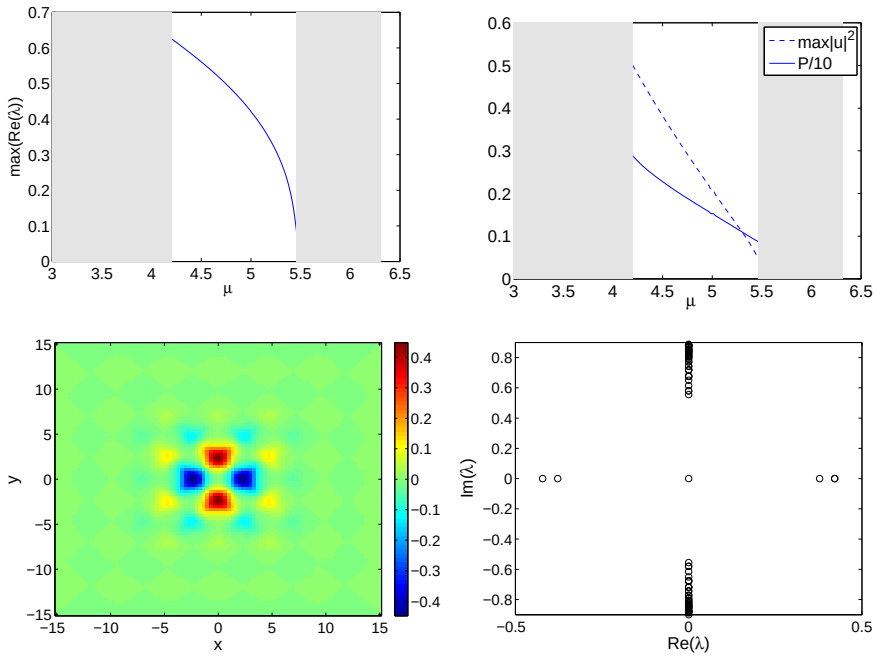

Figure 10. The maximum of the real part of the critical eigenvalue (top left panel) and the power and the peak intensity of the $+-+-$ quadrupoles (top right panel). The bottom panels depict the profile u of a $+-+-$ NN quadrupole at $\mu = 5$ and the corresponding linearization spectral plane of eigenvalues.

In Figure 11, we present the evolution of the unstable $+-+-$ quadrupole shown

in Figure 10. One can see that the configuration is strongly unstable resulting in a breakup of the structure already for $z \approx 10$ to a IPNN dipole state. Subsequent evolution also visits the other state associated with the quadrupole branch, namely the OPN and eventually results into a single hump gap soliton.

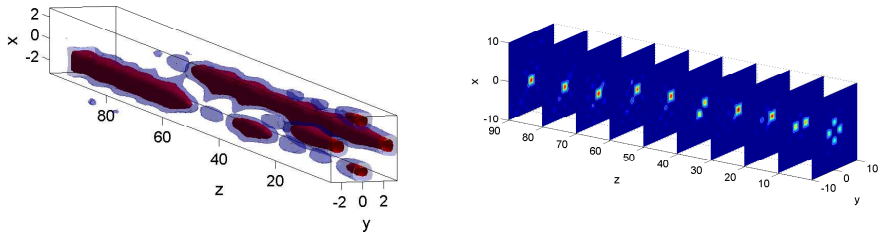

Figure 11. The evolution of the quadrupole presented in Figure 10. Shown are the isosurfaces of height 0.15 (red) and 0.07 (blue) and its slices at some selected propagation distances.

2.3.2 $++++$ Nearest-neighbor Quadrupole Solitons

$++++$ quadrupoles have four in-phase humps at adjacent lattice sites. A typical example of this sort is shown in Figure 12 at $\mu = 5$. We have analyzed the stability of this configuration, finding that it is stable in a wide parametric range, namely for $4.09 \lesssim \mu \lesssim 4.93$, in line with what is predicted by the cubic nonlinearity discrete model in Table 1. Similarly to the IPN and the OPNN branch this branch disappears at a non-zero peak intensity (in this case, for $\max(|u|^2) \approx 0.16$).

The dynamics of the configuration when it is unstable has also been simulated; as a particular example, we integrate the field profile shown in Figure 12 in z. Even though it is unstable, we found that propagation even for 100 units of (dimensionless) length, the profile still resembles its initial condition. This seems to indicate

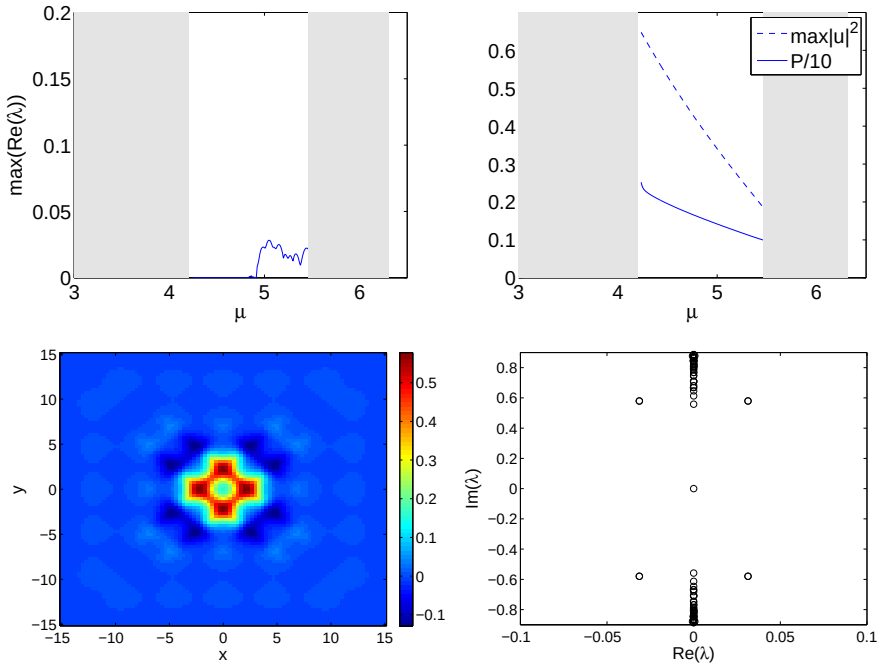

Figure 12. The same as Figure 10 but for the $++++$ quadrupoles. The top panels show the maximal instability growth rate of perturbations (left panel) and the branch optical power and maximal intensity (right panel), while the bottom panels show the solution profile (left) and linear stability (right panel) for $\mu = 5$.

that such structures should be rather straightforward to observe experimentally. For sufficiently long propagation, the dipole will eventually be destroyed through an oscillatory instability.

2.3.3 $+--+$ and $+---$ Nearest-neighbor Quadrupole Solitons

One can also examine other types of quadrupole configurations such as $+--+$ or $+++-$. However, one then typically finds, as may be inferred by their non-symmetric profile, that these configurations are always unstable. As a representative example of these asymmetric profiles, we show in the middle panels of Figure 14 the case of the $+--+$ profile, which is always unstable due to two real eigenvalue

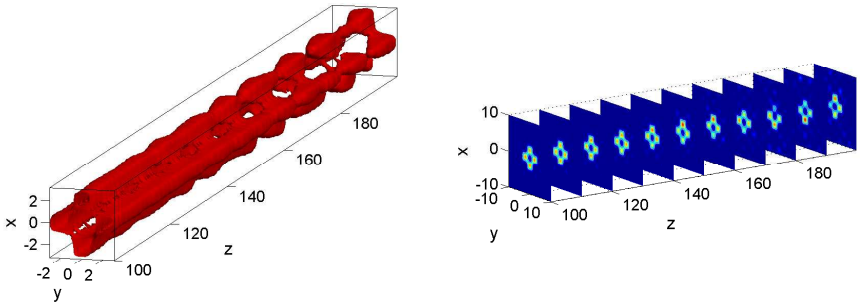

Figure 13. The evolution of the quadrupole presented in Figure 12. Shown are the isosurfaces of height 0.2 (red) and 0.15 (blue) and its slices at particular propagation distances.

pairs (and potentially also oscillatorily unstable).

Note that this configuration is equivalent to the superposition of two IPN (or two OPN, etc.) dipoles. Another saddle node bifurcation happens in this case as the solution approaches the band edge, leading to the collision of this branch with a more extended saddle configuration shown in the bottom panels of Figure 14.

In this case also, observing the dynamics of the instability in Figure 15, we have seen the relatively fast degeneration of the mode into a single site solitary wave profile. The corresponding evolution dynamics for quadrupoles in the focusing case (but for short propagation distances) can be found in [42].

2.4 Experimental Results

In our experiments [3], we use a setup similar to that used in [50]. A partially spatially incoherent beam (of wavelength 488 nm) is produced by use of a rotating diffuser. A negatively biased photorefractive crystal (SBN:60 6x10x5mm^3) pro-

[3]These experiments have been performed by the group of Zhigang Chen at Department of Physics and Astronomy at San Francisco State University and the Key Laboratory of Weak-Light Nonlinear Photonics at TEDA Applied Physics School at Nankai University.

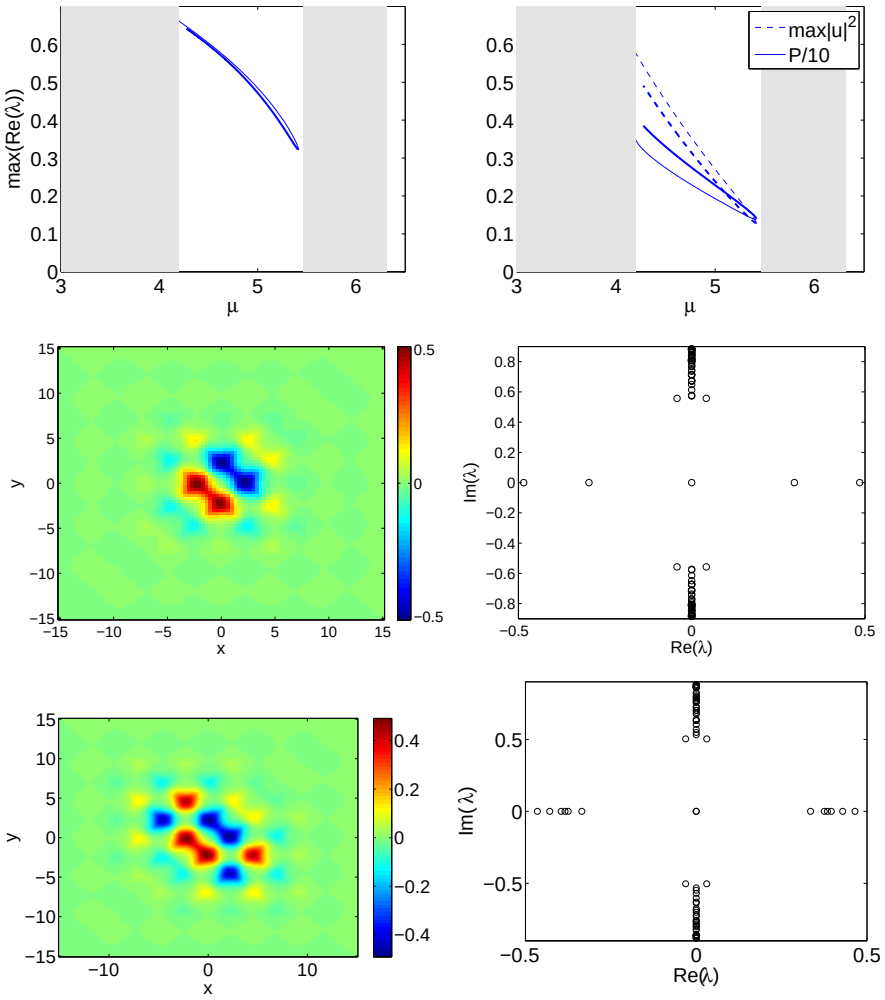

Figure 14. The top four images are the same as Figure 10 but for the $+-\,-+$ quadrupoles; once again the thin lines of the top row correspond to the solution profile and spectral plane of the middle row, while the bold lines of the top row to the solution profile and spectral plane indicated in the bottom row.

vides a self-defocusing nonlinearity. An amplitude mask is also used to spatially modulate the otherwise uniform beam after the diffuser, in order to produce a 2D periodic lattice. The mask is then imaged onto the input face of the crystal, thus creating a pixel-like input intensity pattern with a spatial period of about 25 μm. The ensuing lattice beam (represented by I_{ol} in our theoretical model) is diagonally

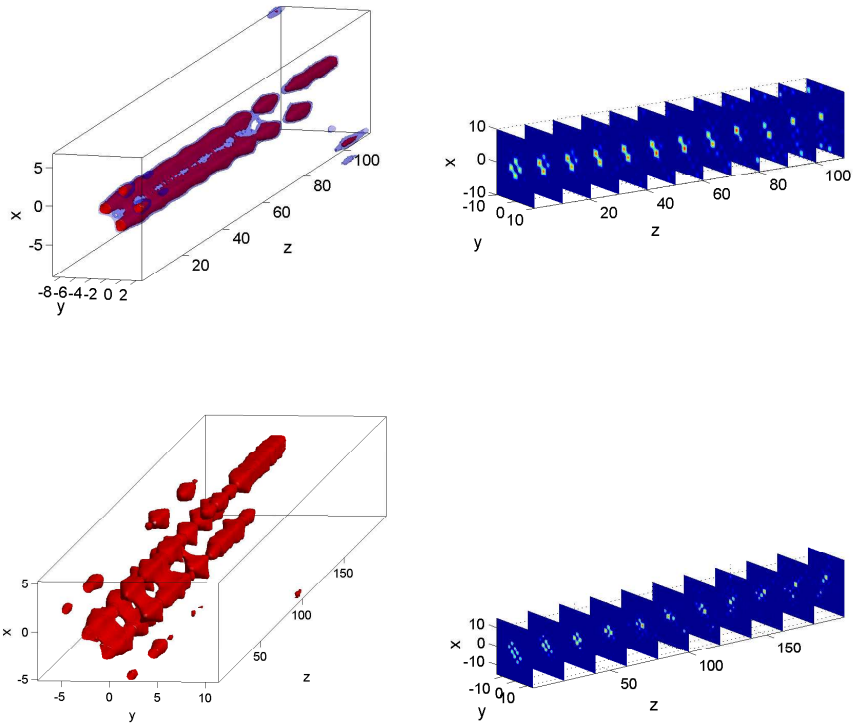

Figure 15. The evolution of the quadrupoles presented in Figure 14. Top panels show the isosurfaces of height 0.2 (red) and 0.15 (blue) and the contour at select propagation distances of the configuration in the middle panels of Figure 14. Bottom panels are the corresponding figures for the counterpart soliton. The isosurface shown is of height 0.1. Both configurations eventually give rise to single-site localization.

oriented and ordinarily polarized, thus the induced waveguide arrays remain invariant during propagation. An extraordinarily (normal to the $x-y$ plane) polarized beam splitting from the same laser output is used as the probe beam (this is the complex field u that we monitor in our analysis above). The probe beam (intensity about 6 times weaker than that of the lattice beam) is sent into a Mach-Zehnder interferometer to create a dipole-like or quadrupole-like input pattern whose phase is controlled with the piezo-transducer (PZT) mirrors. The input/output inten-

sity patterns and the k-space (i.e. Fourier space) power spectra of the lattice and soliton-forming beams are monitored with CCD cameras.

By employing a defocusing nonlinearity, the two-dimensional pixel-like intensity pattern induces a backbone waveguide lattice whose intensity minima correspond to the waveguide sites [14, 51]. Launching two narrow Gaussian beams into two nearest-neighbor or next-nearest-neighbor waveguide sites either with in-phase or with out-of-phase relations, the probe beams evolve into dipole-like gap solitons through the 10 mm SBN crystal under a proper strength of nonlinearity. Typical results are shown in Figure 16, where the output intensity patterns, upon propagation through the crystal (first column), show two main bright spots. This indicates that the energy of the probe beams is mostly localized in the waveguides that were initially excited. The interferograms between these output patterns and a tilted plane wave show that these two main spots remain in-phase or out-of-phase, maintaining their initial phase relation, although the secondary intensity peaks adjacent to the main ones are always out-of-phase with the primary spots. The spatial spectra (Fourier transform) of the patterns (third column) are in good agreement with those obtained from the Fourier transform of the corresponding theoretical solutions (last column). It is important to note here that although some of these configurations such as the OOP NN and the IP NNN dipoles (second and third rows in Figure 16) have been found to *always* be unstable, the limited propagation distances inside the crystal (10mm which corresponds to $z \approx 2.73$ in our dimensionless units) are too short for the instability to develop to an observable degree in the experiment, while it is clearly shown in the theoretical analysis of soliton solutions in the previous sections.

We have also performed experiments to excite quadrupole-like gap solitons, with four narrow Gaussian beams launched into four adjacent waveguide sites (i.e., four

adjacent intensity minima) for both in-phase and out-of-phase conditions. Under a proper level of defocusing nonlinearity, self-trapping is observed with four principal intensity peaks localized in the waveguides initially excited [Figure 17(a)] for both in-phase (top) and out-of-phase (bottom) conditions. Furthermore, the measured spatial spectra [of Figure 17(b)] for these quadrupole-like gap solitons are also in good agreement with the corresponding ones obtained from the theoretical solutions [as shown in Figure 17(c)].

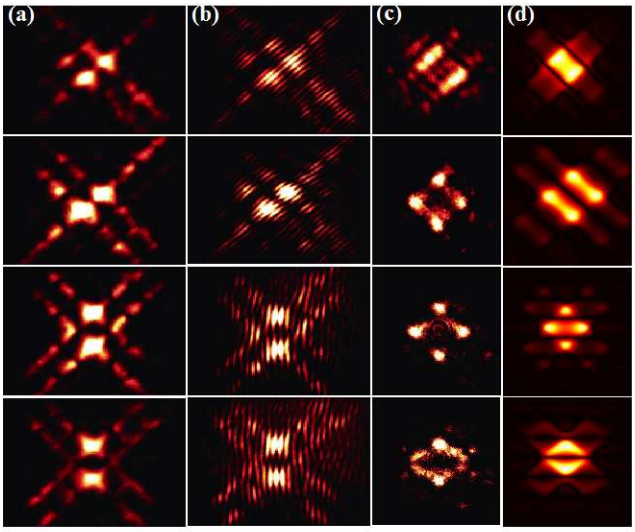

Figure 16. Observations of dipole like gap soliton. From top to bottom: IPN, OPN, IPNN, and OPNN. Panel (a) shows the output intensity patterns, (b) shows the interferograms of these patterns with a tilted plane wave, (c) shows the spatial (Fourier) spectra and, (d) shows those spectra from theoretical calculations of the corresponding solutions.

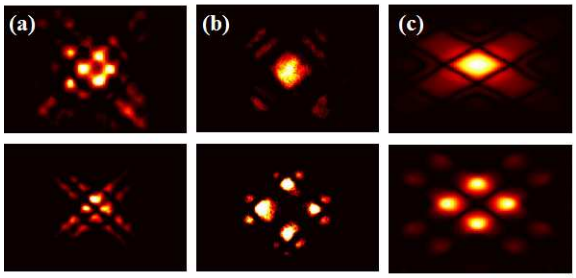

Figure 17. Observations of in-phase (top) and out-of-phase (bottom) quadrupole-like gap solitons. Panel (a) shows the output intensity patterns, (b) shows the spatial spectra, and (c) shows those spectra from theoretical calculations of the corresponding profiles.

2.5 Vortices

In this section we will consider solutions with nontrivial current, i.e. vortex solutions. First we look at the single charge case, which we will refer to as $S = 1$, since it has a phase distribution like $e^{iS\theta}$ (in polar coordinates). We include the experimental attempt to identify the nonexistent 4 site "S=2" vortex (which is indeed the +-+- quadrupole from the previous section).

2.5.1 S=1 Vortices

In this section we report the first experimental demonstration [4] of self-trapping of both single- and double-charged vortex beams by on-axis excitation in a "backbone" photonic lattice induced with a saturable self-defocusing nonlinearity. We show that, under proper nonlinear conditions, a single-charged (S=1) vortex beam can evolve into a gap vortex soliton, while a double-charged (S=2) vortex beam tends to turn into a self-trapped quadrupole-like structure. The spatial power spectra and interferograms (with a tilted plane wave) of the self-trapped vortices from both experiments and numerical simulations are presented, and the stability of the vortex solitons is also studied numerically. Our results show that the gap vortex soliton does not bifurcate from the edge of the first Bloch band. The experimental setup for our study is similar to those used earlier for observation of discrete (semi-infinite gap) vortex solitons in self-focusing lattices [20], except that we now use a self-defocusing nonlinearity to induce the waveguide lattices [37]. The lattice is induced in a photorefractive SBN crystal (5x10x5 mm^3) by a spatially modulated partially coherent light beam sent through an amplitude mask. The mask is appropriately imaged onto the input face of the crystal, creating a periodic input intensity pattern for lattice induction. The lattice period is about 27 μm. With a negative bias voltage, the intensity pattern induces a "backbone" waveguide lattice, as the crystal turns into a defocusing nonlinear medium [13]. The vortex beam is generated by sending a coherent laser beam through a computer generated vortex hologram. In all experiments, the lattice beam is ordinarily-polarized while the vortex beam is extraordinarily-polarized. Thus the lattice beam will undergo nearly

[4] Again, the experiments have been performed by the group of Zhigang Chen at Department of Physics and Astronomy at San Francisco State University and the Key Laboratory of Weak-Light Nonlinear Photonics at TEDA Applied Physics School at Nankai University.

linear propagation in the crystal while the vortex beam will experience a large nonlinearity due to the anisotropic property of the photorefractive crystal [14, 52, 53]. An incoherent white light source was used as a background illumination to fine tune the screening nonlinearity. The output beam patterns and Fourier spectra are monitored with CCD cameras. The vortex beam exiting the crystal is also sent into a Mach-Zehnder interferometer for phase measurement as needed. In the experiment, the off-site excitation scheme is used so that the vortex core is on an index minimum while the donut-like vortex beam covers four adjacent index maxima. To open the first Bragg reflection gap (between the first and second Bloch bands), a relatively high lattice beam intensity and bias field is employed for induction of a deep lattice potential [37]. By fine-tuning the nonlinearity (through the bias field and the lattice-to-background intensity ratio), self-trapping of the vortices can be established. Typical experimental results are presented in Figure 18, for which the intensity ratio of the vortex beam to the lattice beam is about 1:4, and the bias field is about -1.2 kV/cm. The interferograms of the input vortex beams with a tilted plane wave are shown in Figure 18(a), where the central fork resulting from the fringe bifurcation indicates the phase singularity (S=1 for top panels, and S=2 for bottom panels) of the vortex beam. When self-trapping is established in the nonlinear regime, both S=1 and S=2 vortices assume an intensity pattern primarily consisting of four spots [Figure 18(b)], similar to the semi-infinite-gap vortex solitons [20]. Along the directions of the principal axes of the square lattice (which are oriented diagonally rather than horizontally and vertically), long "tails" beyond the central four spots can be seen. Although the intensity patterns of self-trapped S=1 and S=2 vortices look somewhat similar, significant differences can be found in their phase structure and spatial spectrum. First, we use two different interference techniques to identify the phase structure of self-trapped vortices as used

earlier for vortices in self-focusing lattices. One is to send a tilted broad beam (quasi-plane wave) to interfere with the output vortex beam [Figure 18(c)]. For the limited propagation distance of our crystal length (10 mm), it appears that the vortex singularity (manifested by the central fork in the interferograms) persists after the nonlinear propagation through the crystal, although it seems that charge-flipping (reversal of forks) is associated with the S=2 but not the S=1 vortices at the crystal output. However, as shown below from numerical simulations for longer propagation distance, the singularity can be maintained only for the S=1 but not for the S=2 vortices. In fact, our theoretical analysis shows that a "true" double-charged gap vortex soliton does not exist under this excitation condition, and a quadrupole-like soliton structure is found instead for the S=2 vortex. The other technique is to send a co-axial broad Gaussian beam as an interfering beam. We can see clearly that the phase structures for self-trapped S=1 and S=2 vortices are different [Figure 18 (d)]. The two diagonal spots are out-of-phase for the S=1 vortex but in-phase for the S=2 vortex, similar to self-trapped vortices in self-focusing photonic lattices [20].

Next, we measure the spatial spectrum of self-trapped vortices [Figure 18(e)] by using the technique of Brillouin Zone (BZ) Spectroscopy [54]. Again, dramatic differences between S=1 and S=2 vortices can be seen in these Fourier spectra, indicating quite different physical pictures for self-trapping. For the S=1 vortex, most of the power is located alongside the first BZ, but it would not concentrate just to the four corner points (corresponding to four high-symmetry M points) which mark the edge of the first Bloch band and where the diffraction is anomalous [14]. For the S=2 vortex, however, the nonlinear spectrum reshaping makes the power spectrum settle into the M-points quickly, similar to those of the fundamental gap solitons and gap soliton trains [51]. Numerical simulations (see below) show

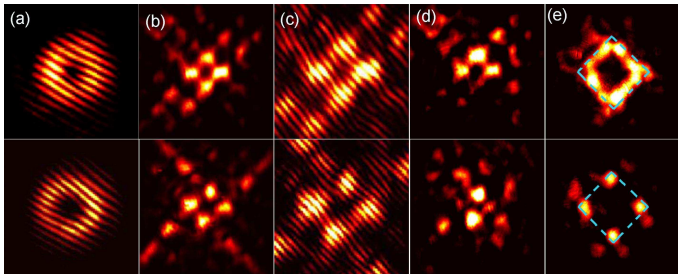

Figure 18. Experimental results of self-trapping of single-charged (top) and double-charged (bottom) vortices in a defocusing photonic lattice. (a) Interferograms showing the phase of the input vortex beams, (b) intensity patterns of self-trapped vortex beams at lattice output, (c, d) interferograms between (b) and a tilted plane wave (c) and an on-axis Gaussian beam (d), respectively, and (e) the Fourier spectra of (b) where the dash squares mark the first Brillouin-zone of the square lattice. (a, c) are zoomed in with respect to (b, d) for better visualization.

that these spectral differences remain for long propagation distances. On the other hand, the S=2 vortex can evolve into a quadrupole-like localized state, which does seem to bifurcate from the edge of the first Bloch band as confirmed by our earlier numerical analysis. We would like to mention that in Figure 18 we did not show the linear output of the vortex beams simply due to that the linear output pattern does not differ significantly as compared to the nonlinear output of Figure 18(b) in our experiment. This is because the induced lattice potential is deep (for opening the first gap [51]) and the length of our photorefractive crystal is only 10mm so the vortex beam does not exhibit strong discrete diffraction as clearly seen in our simulations for longer propagation distances. However, the experimentally measured phase and spectrum of the linear output are apparently different from those of the nonlinear output. In the linear region, all adjacent intensity peaks from the vortex beam have an in-phase relationship and the power spectrum covers the entire first BZ with most of the energy concentrated in the center of the BZ. We now

compare the above experimental observations with our numerical results obtained using beam propagation simulations with the initial condition similar to that for the experiment. The numerical model is a nonlinear wave equation with a 2D square lattice potential under self-defocusing photorefractive nonlinearity [14, 15]. Figure 19 shows the typical simulation results corresponding to experimental results of Figure 18. Excellent agreement can be seen for the 10mm of propagation distance (i.e. our crystal length) for both S=1 and S=2 vortices. In particular, even for only 10mm of propagation, clear differences can be seen in the phase structure [Figure 19(c, d)] and Fourier space power spectrum [Figure 19(e)], as observed in our experiments (Figure 18).

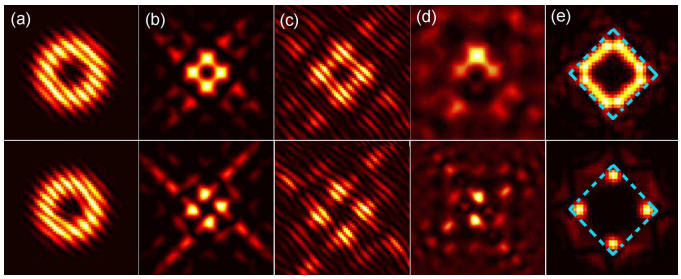

Figure 19. Numerical results of self-trapping of single-charged (top) and double-charged (bottom) vortices in a defocusing photonic lattice corresponding to experimental results of Figure 18. The propagation distance is 10 mm corresponding to the length of the crystal used in experiment.

To examine whether the relevant gap soliton structures can persist for longer propagation distances, simulations are also performed with a propagation distance up to 40 mm while all other parameters are left unchanged. The results are shown in the left panels of Figure 20. Indeed, the corresponding intensity patterns are found to be nearly unchanged even after 40 mm of propagation. However, by interfering the vortex beam with a titled plane wave to observe the phase structure, a major difference is noticed after 40-mm of propagation: while the fork is still in the center

of the interferogram for the S=1 vortex (hence showing that the S=1 gap vortex can maintain its helical phase structure), this is not the case for the S=2 vortex. In the latter case, the forks in the center disappear gradually and the vorticity is eventually lost. In fact, the S=2 vortex loses its original angular momentum and transforms itself into a quadrupole-like structure. Before the vorticity completely disappears, a transient state of charge flipping is found from our detailed simulations, but unlike the periodical appearance of S=2 and S=-2 vortices found in the self-focusing case [55], the S=2 vortex singularity cannot be maintained in self-defocusing lattices, and the vortex disintegrates into an unstable quadrupole-like structure. (In the self-focusing case, the quadrupole appears only as a transient state for charge flipping of the S=2 vortex under the isotropic photorefractive lattice potential [55]). This dynamical evolution can be seen more clearly in the 3D plot of beam propagation illustrated in the right panels of Figure 20. Furthermore, our numerical simulations to longer propagation distances also indicate that the tails of the self-trapped S=2 vortex have wave properties typical to Bloch modes located in the vicinity of the first-band M point (being out-of-phase between adjacent sites along directions of the lattice principal axes [22]). This is consistent with the Fourier space power spectrum that settles onto four M points, indicating that the S=2 vortex evolves into a gap quadrupole soliton bifurcating from the edge of the first Bloch band. On the other hand, similar simulations to 40mm propagation distance for the S=1 vortex does not show this well-defined phase relation in the tails [Figure 20(a)], as some neighboring sites are in-phase and some are out-of-phase along directions of the lattice principal axes. The power spectrum concentrates more into the four sides of the first BZ rather than evolves into a well-defined four M-point spectrum as in Figure 20(b), suggesting that the S=1 gap vortex soliton does not bifurcate from the edge of the first Bloch band. Finally, we investigate the stability of both

S=1 and S=2 self-trapped vortices by means of linear stability analysis for typical parameters corresponding to experimental observations. Our analysis shows that, indeed, the S=1 vortex gap soliton is stable almost throughout the first gap of the defocusing lattice, while the quadrupole gap state is always linearly unstable. Since the latter instability growth rate is relatively small, the quadrupolar structure is observable for certain propagation distances, as demonstrated in our experiment and numerical simulations.

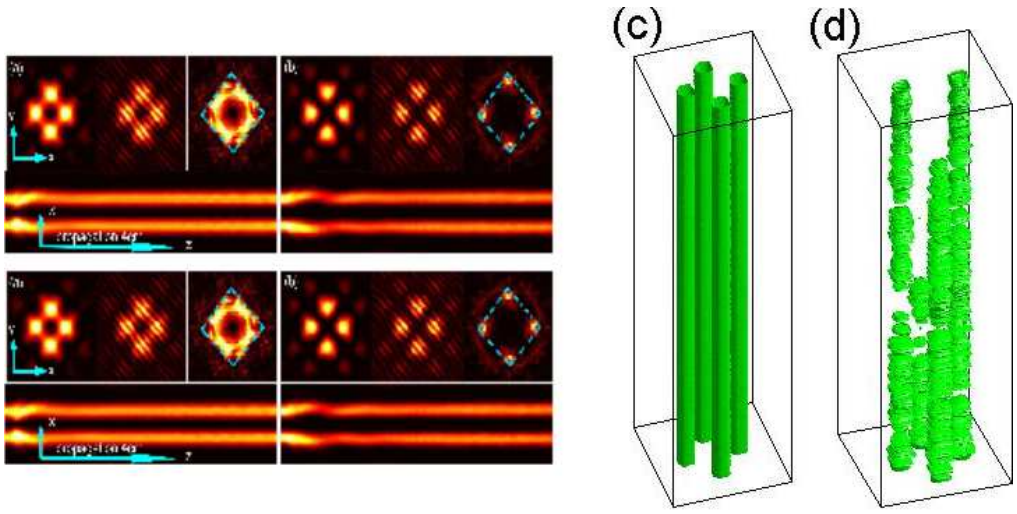

Figure 20. Simulation results of single-charged (a) and double-charged (b) vortex beams propagating to a longer distance of 40 mm. Left panels show the output transverse (x-y) intensity pattern (left), its interferogram with a tilted plane wave (middle), and its Fourier space spectrum (right) in both (a) and (b). Notice that the vortex singularity maintains in (a) but disappears in (b). Right panels show the propagation of a stable S=1 vortex beam (c) and of an unstable quadrupole beam as arising from the breakup of S=2 vortex (d) long the longitudinal z-direction (from bottom to top) through the defocusing lattice.

The soliton solutions (in real and Fourier space) and the corresponding maximal growth rates [maximum real part Re(λ) of the linearization eigenvalues] as

a function of the propagation constant μ are illustrated in Figure 21, where regions of zero growth rate (max[Re(λ)]=0) indicate the linear stability of the gap soliton solutions. We note again that, as seen in Figure 21 (right panels), while the unstable quadrupolar structure seems to bifurcate from a linear Bloch mode of the first band, the same is not true for the S=1 gap vortex soliton, as the latter stability (and corresponding existence) curve appears to have a turning point before reaching the band edge. Results from our experimental observation and numerical analysis are in good agreement with recent theoretical work on the families of the S=1 gap vortex solitons in periodic media [56], where it is also shown that the single-charged vortex families do not bifurcate from edges of Bloch bands, but rather they turn back and move into band gaps before reaching band edges. Although such non-edge bifurcation of vortex gap solitons can be found from the mathematical model of nonlinear propagation of vortices in 2D periodic media, it seems that the underlying physical mechanism for the emergence of such "purely nonlinear" states merits further investigation. Intuitively, this might be attributed to the nontrivial helical phase structure of the vortex, which cannot be expressed as a simple superposition of linear Bloch modes near the band edge. Although the gap vortices in periodic structures have been previously proposed in the literature [56], the theoretical analysis presented here with a model involving a saturable self-defocusing nonlinearity is particularly relevant to our experiments and helpful for a systematic understanding of the experimental observations. Furthermore, the features of the nonlinear spectrum reshaping and instability analysis which have not been illustrated before will stimulate further theoretical study of spatial gap vortex solitons in periodic systems beyond optics.

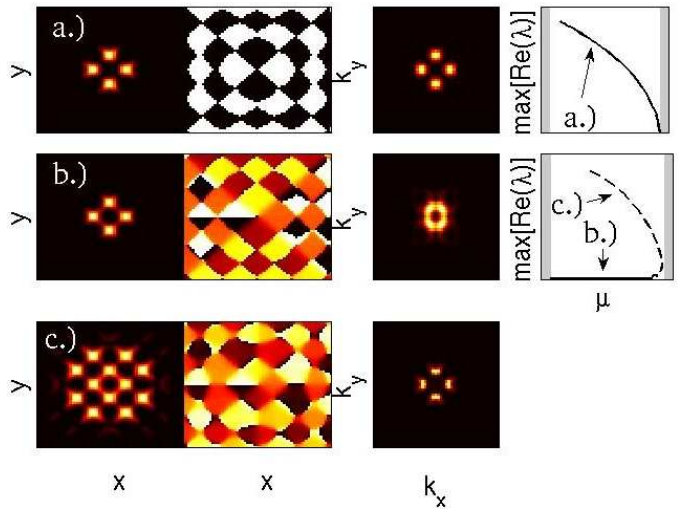

Figure 21. Numerical solutions of self-trapped quadrupole (a) and single-charged vortices (b, c). Shown are typical stationary patterns (first column), corresponding phase structure (second column), Fourier spectra (third column), and maximal instability growth rates (fourth column). Plots in fourth column are given as a function of the propagation constant μ, while the spectral bands are denoted by shaded areas. The first Bloch band is located to the right, where for the single-charged vortex family the stable node branch (solid curve, b) collides with the unstable saddle branch (dashed curve, c) before reaching the band edge. Zero growth rates indicate that the self-trapped structure is linearly stable.

CHAPTER 3

HEXAGONAL AND HONEYCOMB LATTICES (DISCRETE)

In this chapter, we will focus, in particular, on the recently emerging area of *non-square* lattices in waveguide arrays, as well as in light induced photonic crystals [24, 25, 31, 33, 34]. Such lattices were also considered earlier from a theoretical perspective in discrete settings such as, e.g. [30]. We will study here the existence, stability and dynamical properties of multi-pulse solitary wave structures, as well as of discrete vortex structures in both hexagonal and honeycomb lattices. We will focus on two prototypical contours of such lattices, namely, a more extended six-site contour, as well as a reduced three-site contour, both depicted in Figure 22. Our prototypical model of interest will be the discrete nonlinear Schrödinger (DNLS) equation and our results will be presented for the case of a focusing nonlinearity; however, our findings can be directly transformed to the case of a defocusing nonlinearity. Additionally, we should note that similar results can be obtained in Klein-Gordon models and have been illustrated, e.g., for three-site contours in hexagonal lattices [32, 57].

It is relevant to note that crystalline configurations of strongly coupled doped plasmas (dusty plasma crystals) occur in the form of 1D or 2D monolayers formed

in low-temperature gas discharge experiments [58]. Interestingly, such dust crystals generically appear as spontaneously formed hexagonal 2D arrangements [59], although alternative configurations also include honeycomb 2D lattices [60] and 1D dust chains (when appropriate trapping potentials are used for lateral confinement [61]). A discrete Klein-Gordon description has recently been employed to model the dynamics of transverse vibrations of dust grains in dusty plasma crystals, both in 1D [62] and in hexagonal 2D dust lattices [63].

The key findings that we report here are the following:

- For the focusing nonlinearities in a six-site honeycomb/hexagonal contour, topological charge $S = 2$ configurations may be stable, while $S = 1$ ones can never be stable (this is reversed for defocusing nonlinearities). This represents a notable qualitative difference from the results in the case of a square lattice [12], where the prototypical contour consisting of four sites features a potentially stable $S = 1$ vortex.

- In these contours, alternating 0-π phase configurations are also potentially stable, while in-phase configurations are not stable (again, the results are reversed for defocusing nonlinearities). While this instability can be implicitly inferred from the instability of the corresponding building blocks (i.e., the instability of the in-phase dipole and the potential stability of the out-of-phase dipole [64]), its quantitative characteristics can only be traced through the approach presented below.

- In three-site contours, the only potentially stable configuration is that of a discrete vortex, while both in-phase and alternating phase configurations are observed to be unstable.

- The evolution of the dynamical instability in the discrete lattices is more complex than in the square lattice case, and may involve not only degeneration to single-site solitons but possibly to multi-site solitary wave structures, and often the formation of robust breathing states, consisting of multiple sites (possibly even as many as the original configuration). In fact two clear breather formations recur in multiple simulations:
  - Two sites with fluctuating, usually π-separated, phases and oscillating amplitudes of comparable magnitude.
  - Two sites with different amplitudes oscillating between the same relative phases and π-separated phases, depending on whether the amplitudes are closer or further, respectively.

Six-site configurations with phases of 0 or π will be collectively called "hexapoles" herein, while three-site configurations with phases 0 or π will be collectively termed "tripoles".

Our presentation of the above findings is structured as follows. In section 3.1, we present theoretical predictions, then in Section 3.2 we corroborate them with numerical bifurcation results illustrating the various nonlinear modes in both hexagonal and honeycomb geometries and their stability properties, and finally in section 3.3 we explore the dynamical manifestation of the instabilities. The continuum version will be explored in the following Chapter.

3.1 Existence and stability theory

We first translate the general theoretical considerations presented in Chapter 1 to the present scenario.

Herein each site of the lattice will have either six neighbors, in the hexagonal case, or else three neighbors in the honeycomb case The neighbor set G of the discrete Laplacian, 1.2, will then be either one of the two three element sets $\pm\{\mathbf{b}_1 = (1,0), \mathbf{b}_2 = (-\frac{1}{2}, -\frac{\sqrt{3}}{2}), \mathbf{b}_3 = (-\frac{1}{2}, \frac{\sqrt{3}}{2})\}$, depending on the site for the honeycomb lattice, or else $\{\pm\mathbf{b}_1, \pm\mathbf{b}_2, \pm\mathbf{b}_2\}$ for the hexagonal.

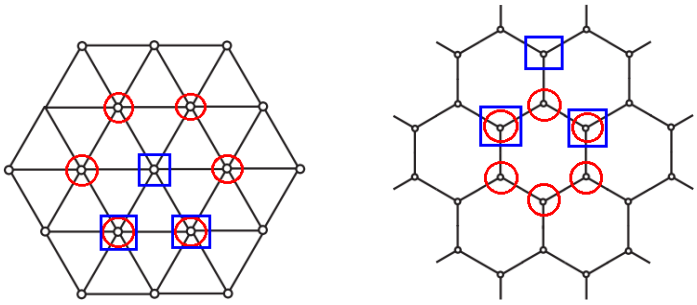

Figure 22. Discrete lattice configurations for the hexagonal geometry (left), in which each node has six neighbors, and the honeycomb geometry (right), in which each node has three neighbors. The relevant "hexapole" configurations are represented by the red circles and the "tripoles" are given by blue squares. Notice that the relevant three site configuration for the honeycomb is composed of next-nearest neighboring sites.

We will consider three- and six-site contours in each of the hexagonal and honeycomb geometries, shown in Figure 22. Recall the relationship between the eigenvalues, λ_j, of the linearized operator (1.11) and the eigenvalues, γ_j, of the Jacobian, (1.14), of the persistence condition given in Eq. (1.8), is given by $\lambda_j = \pm\sqrt{2\gamma_j\varepsilon}$ (1.13), for nearest-neighbor excitations. If the non-zero sites comprising the contour are next-nearest neighbors instead, as in the case of the three site contours for the honeycomb lattice geometry (see Figure 22), then ε is replaced by ε^2 in the previous relation. Again, unstable solutions for weak coupling (small ε) can then be identified as those for which the eigenvalues λ_j have non-zero real part, given

the Hamiltonian nature of the model.

We will consider primarily contours M such that $|\theta_{j+1}-\theta_j| = \Delta\theta$ is constant for all $j \in M$, $|\theta_1 - \theta_{|M|}| = \Delta\theta$ and $\Delta\theta|M| = 0 \bmod 2\pi$ and $|M| = 3$ or 6, except one case which will be treated separately. In the primary case, all the non-zero elements of this matrix are then factors of $a = \cos(\Delta\theta)$, and the eigenvalue problem of the Jacobian $\mathcal{J}$ reduces to the following difference equations:

$$a(2x_n - x_{n+1} - x_{n-1}) = \gamma_j x_n. \tag{3.1}$$

These can be solved by a discrete Fourier transform with any eigenvector $x_n \sim \exp(i2\pi nj/|M|)$, whence $\gamma_j = 4a\sin^2(\pi j/|M|)$ and then

$$\lambda_j = \pm\sqrt{8\varepsilon\cos(\Delta\theta)\sin^2\left(\frac{\pi j}{|M|}\right)}. \tag{3.2}$$

Recall that for the honeycomb three-site next-nearest-neighbor contours the above formula should be used with ε replaced by ε^2. The special case of the three-node contour with phases 0, π and 0 can be treated also in the framework of the Jacobian of Eq. (1.14) [and its eigenvalues computed by Eq. (1.13)], although it does not fall under the general calculation of Eqs. (3.1)-(3.2). We will consider contours of nodes with $|M| = 3$ or 6 and separated by either $\Delta\theta = 0, \pi, \pi/3$, or $2\pi/3$, for the different contours in this work.

3.2 Numerics

Both in this section, detailing the various configurations and their corresponding stability over the six-node and three-node contours, and in the next one, comparing the corresponding dynamics, we will partition our discussion into two subsections. The first one will be devoted to the results obtained for the hexagonal geometry, and the second devoted to the case of the honeycomb geometry.

3.2.1 Hexagonal geometry

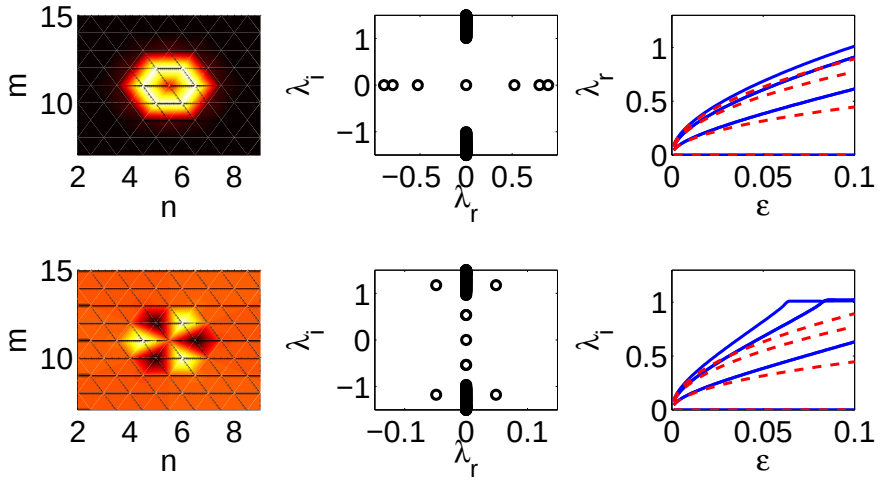

Figure 23. Six-site real-valued configurations in a hexagonal geometry. The top row corresponds to the *unstable* $\Delta\theta = 0$, or "in phase" solutions, while the bottom corresponds to the *stable* $\Delta\theta = \pi$, or "out of phase" ones. From left, the first column is the profile at $\varepsilon = 0.08$, the second column shows the corresponding linearization spectrum (λ_r, λ_i) of the eigenvalues $\lambda = \lambda_r + i\lambda_i$, and finally the third column shows the continuation in ε of the actual eigenvalues [real, λ_r, and imaginary, λ_i, components] (solid) and the theoretical predictions given by Eq. (3.2) (dashed).

First, we will study six-site contours, of which we will consider four. The first two of these are real and are such that either $\Delta\theta = 0$ or $\Delta\theta = \pi$ (any additional combination of 0 and π phases is also possible but the main qualitative characteristics of stability will not change from those reported below). The relation (3.2) for $\Delta\theta = 0$ predicts double eigenvalue pairs at $\pm\sqrt{2\varepsilon}$ and $\pm\sqrt{6\varepsilon}$ and single pairs at $\pm\sqrt{8\varepsilon}$ and 0, while for $\Delta\theta = \pi$ each of these is multiplied by the imaginary unity. Direct numerical computation and continuation in the coupling parameter ε from the AC limit confirm the predictions presented in Figure 23. The in-phase

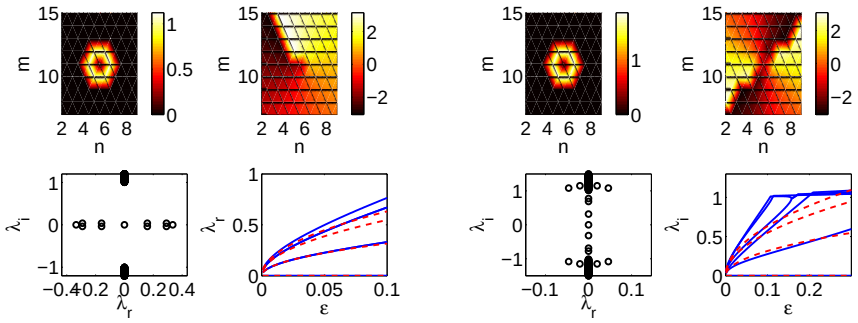

Figure 24. The six-site vortices in the hexagonal geometry are shown. The left four images show the *unstable* single-charged solution branch with $\Delta\theta = \pi/3$, while the right set is for the *stable* double-charged solution branch with $\Delta\theta = 2\pi/3$. The single-charged vortex is *unstable*, while the double-charged one is *stable* (until the oscillatory instability resulting from the collision of the pairs of negative Krein signature with the phonon band). The top row of each set displays the modulus (left) and argument (right) of the solution with $\varepsilon = 0.025$ (top) and $\varepsilon = 0.125$ (bottom), while the bottom left is the linearized spectral plane and the bottom right is the continuation of the relevant eigenvalues from the AC limit, with the solid and dashed lines representing the numerical solution and the theoretical prediction, respectively.

configuration with $\Delta\theta = 0$ becomes strongly unstable (immediately) away from the AC limit, while the out-of-phase configuration with $\Delta\theta = \pi$ is stable for small ε. It should be noted that more generally any configuration that has two adjacent in-phase nodes along the six-site contour will also be unstable for all values of ε, while the *only* potentially stable configuration of this type (real solution comprising 0 and π phases) is the out-of-phase adjacent node structure of $\Delta\theta = \pi$. However, we emphasize that even for that configuration, the imaginary eigenvalues which bifurcate from the origin in the AC limit have the topological property of negative Krein signature [12]; this means practically that they become structurally unstable upon collision with other eigenvalues, such as those of the phonon band, which

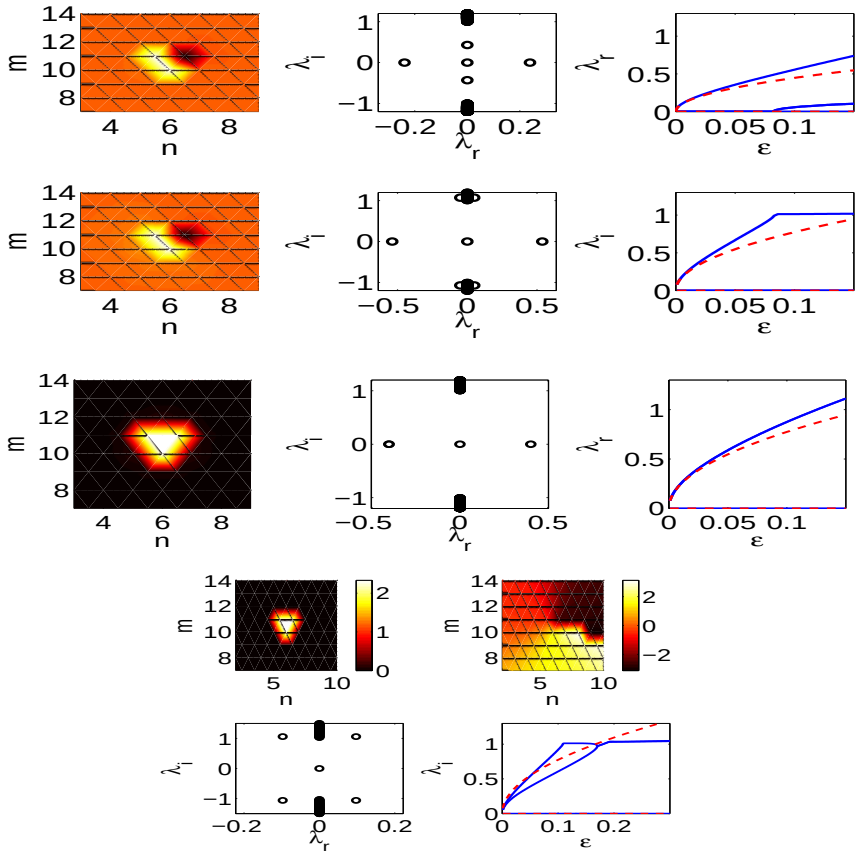

Figure 25. The three-site configurations in the hexagonal geometry. The top two rows present the same panels as Figure 23 except for the *unstable* unconventional case where $\theta_1 = \pi$, and $\theta_2 = \theta_3 = 0$ and the third is the *unstable* three-site $\theta = 0$ case shown in the same format. The four panels below that display the *stable* (for $\varepsilon \lesssim 0.1$) three site singly-charged vortex with $\theta = 2\pi/3$. They are (clockwise from top left) the modulus (for $\varepsilon = 0.2$), phase, continuation of its principal eigenvalues as a function of the inter-site coupling strength ε, and linear stability spectrum (for $\varepsilon = 0.2$). Two rows are given for the $0, \pi, 0$ case because one of the null pairs from the AC limit becomes real (third column of the first row; the solution and its stability in the first and second column are shown for $\varepsilon = 0.025$), while the other becomes imaginary (third column of the second row; here the solution and its stability are for $\varepsilon = 0.095$).

have positive Krein signature. Hence, when the coupling becomes sufficiently large ($\varepsilon \gtrsim 0.06$), these eigenvalues eventually intersect with the continuous spectrum (the phonon band) edge located at $\pm i\Lambda$, and result in Hamiltonian-Hopf bifurcations associated with complex quartets of eigenvalues and oscillatory instabilities. Such collisions can be detected in the graphs illustrating the lowest imaginary eigenvalue parts λ_i in the bottom right panel of Figure 23, and are associated with the points where the eigenvalue trajectories begin to level out. The spectrum of the solution at $\varepsilon = 0.08$ in the bottom middle panel of Figure 23 reveals the presence of such quartets.

Next, we consider the complex valued solutions along the six site contours, for which our conditions guarantee vorticity (i.e., the relevant solutions will be discrete vortices whose phase completes a round trip of a multiple of 2π along the discrete contour). The fundamental solutions here are for $\Delta\theta = \pi/3$, which is a single-charged vortex, and $\Delta\theta = 2\pi/3$, which is a double-charged vortex. The relation (3.2) predicts that the single-charged vortex will be unstable with double eigenvalue pairs $\pm\sqrt{\varepsilon}$ and $\pm\sqrt{3\varepsilon}$, and single pairs at $\pm\sqrt{4\varepsilon}$ and 0. On the other hand, the double-charged vortex is actually linearly *stable* in this lattice geometry for sufficiently small values of the coupling, with the same pairs as the single charged vortex, except multiplied by i. Figure 24 presents both types of configurations, indeed illustrating the numerical linear instability of the former, and numerical linear stability of the latter structures. Nevertheless, it should be pointed out that for higher values of the inter-site coupling ($\varepsilon \gtrsim 0.1$) in this case also, the topological charge $S = 2$ solution eventually becomes unstable as well due to oscillatory instabilities, as is shown in the bottom right continuations of the relevant eigenvalues of Figure 24. Notice also the generally excellent qualitative and good quantitative agreement –at least for small values of ε (for larger values

of the coupling parameter higher order effects become important)– between the theoretical predictions of Eq. (3.2) and the numerical results.

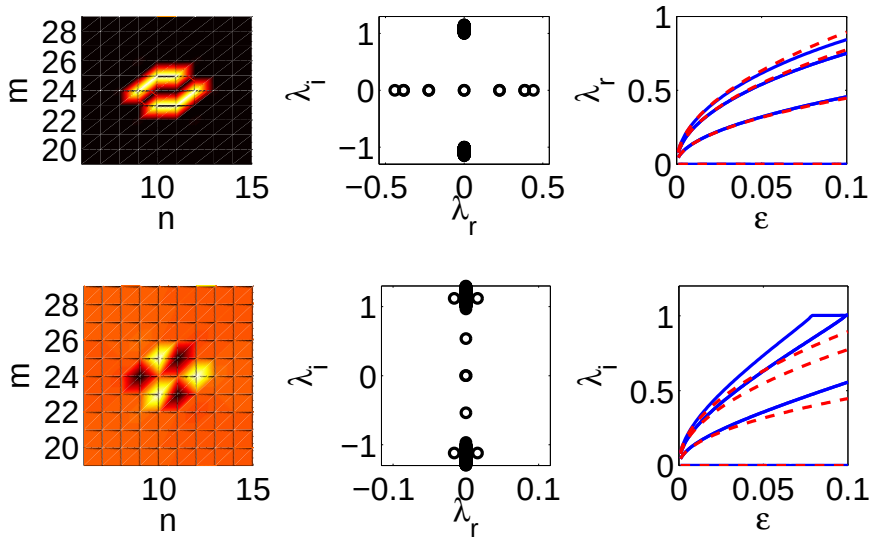

Figure 26. The same panels as Figure 23, except for the honeycomb geometry. The particular solutions are for $\varepsilon = 0.025$ (top) and $\varepsilon = 0.095$ (bottom).

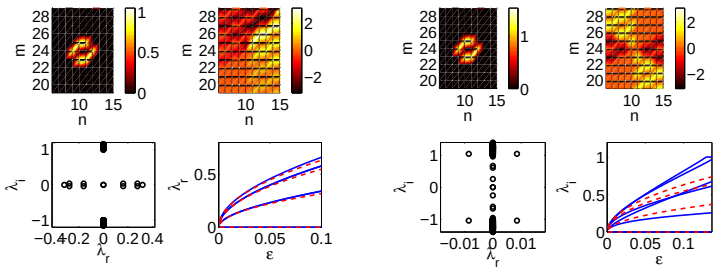

Figure 27. The same as Figure 24 except for the honeycomb lattice. The particular solutions given are for the coupling constants $\varepsilon = 0.025$ (left) and $\varepsilon = 0.135$ (right).

We now turn to the configurations comprised of three lattice sites. We consider three such cases, similarly to [32] where a Klein-Gordon model was considered. The first two are the standard real ($\Delta\theta = 0$) and complex-valued ($\Delta\theta = 2\pi/3$,

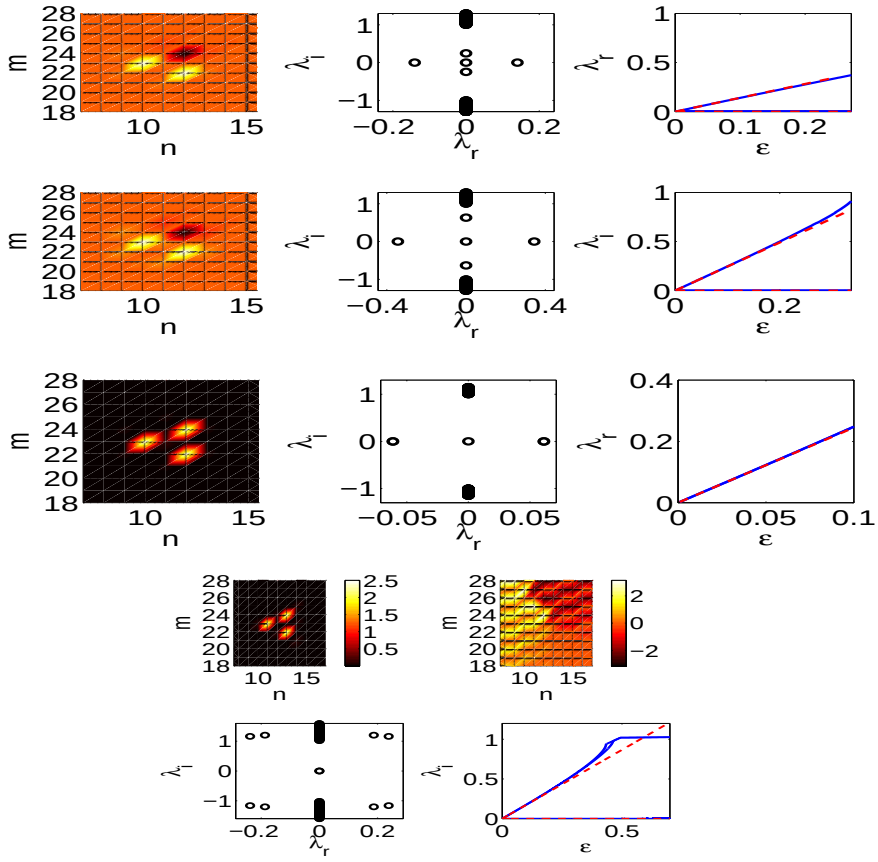

Figure 28. The same as Figure 25 except for the honeycomb lattice geometry. The particular solutions shown are for $\varepsilon = 0.025$ (top and third rows), $\varepsilon = 0.27$ (second row) [the unconditionally *unstable* solutions], and $\varepsilon = 0.6$ for charge 1 vortex solution, which is *stable* for $\varepsilon \lesssim 0.5$, in the bottom set.

corresponding to a discrete vortex of topological charge $S = 1$) ones, while the last one is the non-standard case with phases 0, π and 0 for the three sites. For $\Delta\theta = 0$ the theoretically predicted double pair of $\pm\sqrt{6\varepsilon}$ and pair at 0 are confirmed to exist in the middle row of Figure 25, while for the discrete single-charged vortex solution with $\Delta\theta = 2\pi/3$, the double pair $\pm\sqrt{3\varepsilon}i$ and a pair at 0 are also found to reasonably approximate its linearization eigenvalues in the bottom row of Figure 25. It should be noted that for larger coupling ($\varepsilon \gtrsim 0.02$) the double pair of eigenvalues splits, as

can be observed in the numerical results. These solutions also become unstable as usual after the first eigenvalue collides with the continuous spectrum at $\varepsilon \approx 0.09$. On the other hand, for the configuration with phases 0, π and 0 of the top rows, one pair of eigenvalues remains at the origin, due to the phase invariance, while one of the remaining two pairs becomes imaginary (theoretically predicted as $\pm i\sqrt{6\varepsilon}$) and the other one becomes real (predicted as $\pm\sqrt{2\varepsilon}$). We can again observe that the full numerical results agree well not only qualitatively but also even quantitatively with the theoretical description.

3.2.2 Honeycomb Geometry

We now explore the same configurations systematically in the case of the honeycomb lattice geometry, in which each node has three neighbors as opposed to six. In Figure 26, we again consider two representative real configurations, namely the in-phase six-site structure (top row), and the out-of-phase hexapole, where adjacent neighbors have a relative phase shift of π. We find that the principal stability characteristics are similar to those in the hexagonal case, in agreement with the theoretical prediction. In fact, we can observe that quantitatively the agreement of the linearization eigenvalues is arguably even better between theoretical predictions and full numerical computations in this case. This is because the central site, mediating second-order inter-site interaction between the excited sites, is absent in the six-site configuration in the honeycomb lattice (contrary to the case for the hexagonal configuration). This feature reduces the role of higher order corrections to the theoretical predictions and hence renders the leading order predictions accurate for wider parametric ranges. This is a feature that we consistently observe throughout our honeycomb lattice results.

The six-site discrete vortices are illustrated for this lattice in Figure 27. Once

again, the interesting feature of the immediate and generic (i.e., independently of the precise value of ε) instability of the vortex of topological charge $S = 1$ can be observed, while the vortex of topological charge $S = 2$ is stable for small values of the coupling and is destabilized for sufficiently large couplings ($\varepsilon \gtrsim 0.13$) by means of oscillatory instabilities. Note the larger value of the coupling necessary for the onset of an oscillatory instability here as compared to the hexagonal case, presumably a result of the higher order terms present in the latter due to presence of the center site.

Finally, the interesting feature of the three-site configurations in the honeycomb case is that they now constitute *next-nearest-neighbor* configurations. As a result, the theoretical prediction that should be compared to the full numerical results is now $\propto \varepsilon$ rather than $\propto \sqrt{\varepsilon}$. This is clearly seen to be consonant with the full numerical findings of Figure 28, not only for the strongly unstable (with a double real pair $\pm\sqrt{6}\varepsilon$) configuration of the in-phase case, or for the linearly stable (for $\varepsilon \lesssim 0.43$)) vortex case (with a double imaginary pair $\pm\sqrt{2}i\varepsilon$), but also for the top-row, 0-π-0 case of one real ($\pm\sqrt{2}\varepsilon$) pair and one imaginary ($\pm\sqrt{6}i\varepsilon$) pair of eigenvalues.

3.3 Dynamical Evolution Results

We now examine the nonlinear dynamics of an unstable solution of each configuration upon integration of a slightly perturbed waveform $u = u^s(1+u^r)$, where u^s is the complex valued vector field which is a stationary unstable solution to Eq. (1.1), and u^r is a random noise field (i.e., a field in which every entry is a random variable distributed uniformly in the interval between $\pm 0.05 \max_{\{m,n\}}[|u_{m,n}(t=0)|^2]$). Since the coupling sensitively affects the dynamics (in particular, larger coupling

facilitates communication between sites and hence manifestation of the instability), we use a fixed coupling of $\varepsilon = 0.1$ for all solutions except for those which are stable until larger values of ε. In a few seemingly counterintuitive cases we examine the cases of larger perturbation and coupling, and find that these effects (more so the coupling) do indeed influence the dynamical evolution. We will see that several cases degenerate to similar two-site breathing structures with phase correlation which may be either out-of-phase or oscillating between in- and out-of-phase.

3.3.1 Hexagonal Geometry

First, we explore the evolution of characteristic unstable solutions from the families of configurations in a hexagonal geometry given in section 3.2.1. Within this class we begin with the six-site configurations. The evolution of the real valued solution with $\Delta\theta = 0$ from the family in the top row of Figure 23 is displayed in Figure 29. The rapid destruction of the original configuration confirms the linear stability analysis, which predicts strong instability from five pairs of real eigenvalues. However, for $\varepsilon = 0.1$ (top set) and a 5% perturbation, after the destruction of the initial configuration, a robust three site oscillating breather state emerges (note the plot of individual site amplitudes as a function of propagation distance in the third row of Figure 29). Despite the apparent coherence of the amplitude oscillations, the relative phases of the sites appear to be uncorrelated and are not shown. A similar phenomenon is observed for a much larger initial perturbation of 25% of the initial amplitude (bottom left panels of Figure 29), although here the amplitude oscillations remain irregular even with three populated sites, and after a long distance, a nonlinear dynamical structure emerges in the form of a two-site breather. Again, however, there is no definite pattern in their relative phases. For a much larger coupling, on the other hand, as shown in the bottom right panels, all

sites except for one decay very rapidly and a single site survives for long distances. Dynamical evolution of a real valued solution from the bottom row of Figure 23 with $\Delta\theta = \pi$ is displayed in Figure 30. The original configuration takes considerably longer to decompose than the in-phase counterpart given above, confirming the expectation based on the small magnitude complex quartet of unstable eigenvalues of the linearized system. Once again, in this case a two-site structure with oscillating amplitudes persists long after the original break-up. However, in this case, there is a strong phase correlation, and when the amplitudes of these sites are close they are in-phase, while when they are distant they are out-of-phase (shown in the right panels).

Next, we consider the vortex solutions with six sites. Both of these configurations confirm again the linear stability analysis, and also both feature two-site breathers for long distances. The single-charged vortex ($\Delta\theta = \pi/3$) from the left panels of Figure 24 decays into a breather with uncorrelated phases, similarly to the bottom left panel of Figure 29 and, hence is not shown. The evolution of the more stable double-charged vortex ($\Delta\theta = 2\pi/3$) from the right panels of Figure 24 is in Figure 31. Notice the almost harmonic oscillations of the breather shown in the inset for the double-charged case. Here the two sites are also of comparable amplitudes, but as they oscillate they remain usually out-of-phase with each other as shown in the right panels. Another feature of both of these cases is that one of the two ultimately surviving sites is the originally unpopulated center site, which inherits mass from other sites when they decay (see also the insets in each figure).

We now consider the three-site configurations. Both the $\theta_i = 0, \pi, 0$ solution from the top rows of Figure 25 (unstable due to one real pair of eigenvalues) and the more unstable $\Delta\theta = 0$ solution given below that (which is unstable due to two pairs of real eigenvalues), ultimately decay into in-phase/out-of-phase breathers

such as the one shown in Figure 30, although faster in the latter case due to the two unstable directions. The latter is displayed in Figure 32. The final three site configuration is from the potentially stable $\Delta\theta = 2\pi/3$ family in the bottom panels of Figure 25. The imaginary eigenvalues with negative Krein signature do not reach the continuous spectrum until a large coupling value in this case, and so we investigated the dynamics for $\varepsilon = 0.2$. Despite the magnitude of the growth rate being comparable with the previous cases, two of the original populated sites here rapidly decay and a robust single site remains. This may be a result of the stronger site interaction induced by the larger coupling.

3.3.2 Honeycomb Geometry

We now turn to the same configurations as above but in the honeycomb geometry, as explored in section 3.2.2. Interestingly, in this case, for $\varepsilon = 0.1$, and a 5% perturbation, all configurations result in multi-site breathing structures with up to four populated sites for long propagation distances. Since the dynamical evolution of the six-site configurations in the hexagonal geometry all involve communications with the center site, it is reasonable to hypothesize that this is a major contributor to the rather significant differences observed below between the nonlinear evolution presented in this and the previous subsection.

First, we display the results of the evolution of a real valued configuration from Figure 26 in Figure 33. The linearized system of the solution with $\Delta\theta = 0$ in Figure 33 is strongly unstable with five real pairs of eigenvalues, and the one with $\Delta\theta = \pi$ has all the same multiplied by the imaginary unity. The dynamical evolution confirms the stability analysis and two sites decay very rapidly for the in-phase configuration, while much more slowly for the more stable out-of-phase one (not shown). On the other hand, it is noteworthy that the four sites persist for long

distances in each case and that the more linearly stable out-of-phase one decays into three sites eventually, which have apparently uncorrelated phases. The resulting four site breather in the in-phase case for $\varepsilon = 0.1$ (left) is actually comprised of two out-of-phase breather pairs, such as the one in Figure 31, while for $\varepsilon = 0.3$ (right) the phases of the unequal amplitude breather pair oscillate between in-phase and out-of-phase. Also, as in the hexagonal case of the $\Delta\theta = 0$ family, we explored the sensitivity of the nonlinear evolution to larger perturbation and coupling and found that two sites robustly remain for the larger coupling $\varepsilon = 0.3$, while four remain for $\varepsilon = 0.1$ (not shown). For this reason, these solutions were continued for an extra long propagation distance up to $z = 2000$, and for consistency and comparison the remaining cases in this setting will also be continued for the same distances.

The instability of the discrete vortices from Figure 27 results in multiple sites persisting with large amplitude oscillations for long distances, ultimately evolving to an out-of-phase two-site breathing structure for the single-charged ($\Delta\theta = \pi/3$) one (not shown) and a four-site structure for the double-charged ($\Delta\theta = 2\pi/3$), shown in Figure 34. This four site structure consists of an out-of-phase pair close in amplitude and an unequal amplitude pair oscillating between in-phase and out-of-phase (see right panels) until a very long distance when they reshape into two out-of-phase pairs (phase not shown). The latter part is reminiscent of the result of evolution of the in-phase hexapole for small ε given in the left panels of Figure 33.

Finally, we show the evolutions of the three-site configurations from Figure 28. Figure 35 displays the dynamics of an unstable $\theta_i = 0, \pi, 0$ solution. The persistence for very long distances of the three sites for the smaller coupling prompted an investigation of a solution with larger coupling of $\varepsilon = 0.27$ from this family. This turned out to decay very rapidly to a single site (not shown). In the smaller coupling

case, an intricate breathing pattern emerges which apparently converts the mode into a three-site breather (rather than a three-site stationary solution). The three-site configuration with $\Delta\theta = 0$ is not shown, but again here all three sites survive for a long propagation distance for $\varepsilon = 0.1$. This does not necessarily contradict the linear instability, since the configuration deviates almost immediately in terms of amplitude distribution. There is no clear correlation in the phases in this case. Again the persistence of all three sites for $\varepsilon = 0.1$ prompted investigation for a larger coupling $\varepsilon = 0.3$ and again a single site ultimately remained, although in this case two sites also persisted for a significant distance before the ultimate degeneration into a single-site waveform. For the last three site configuration the same consideration of the coupling arises, since this configuration is unique among those considered here, in the sense that a considerably larger coupling strength is required for the imaginary eigenvalues to collide with the continuous spectrum and the instability of this state to occur. Even with the very mild instability when the first imaginary pair collides with the phonon band at the very large coupling value of $\varepsilon = 0.43$, the dynamics clearly illustrate the oscillatory instability. The original configuration persists until $z = 30$, ultimately concentrating primarily on a single site for long propagation distances. Aside from the six-site in-phase configuration, this is the only one for which the dynamics are qualitatively similar in the honeycomb and hexagonal geometries. Breather-like structures arose for certain parameter values for all other configurations considered. The relative phases of the two-site breathers which recurred in many of the simulations suggest that these may exist as potentially stable time-periodic solutions.

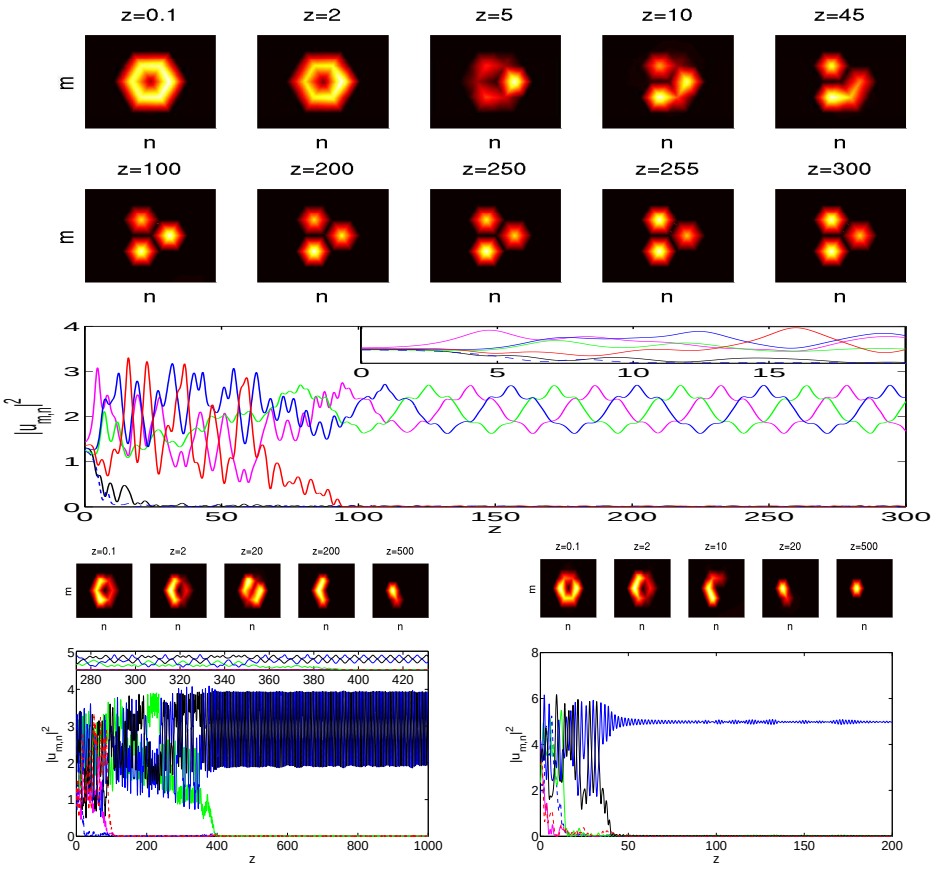

Figure 29. The top two rows are snapshots in the evolution of the solution corresponding to $\varepsilon = 0.1$ from the family with $\Delta\theta = 0$ given in the top row of Figure 23, under a small perturbation by a random noise field to seed the instability. The third row shows the squared amplitude as a function of propagation distance of the relevant sites, and the inset shows a closeup of the small distance dynamics. Notice the structure of the robust three-site periodic structure which emerges after the original configuration dissolves. Below the third row panel there are two sets of images for a much larger perturbation of 25% of the intitial amplitude (left), where the third populated site eventually decays as well and only two sites persist for long distances, and a much larger coupling $\varepsilon = 0.3$ (right), where the configuration decays very rapidly and a single site solitary wave remains. There is no clear correlation between the phases of either of the solutions with multiple remaining sites.

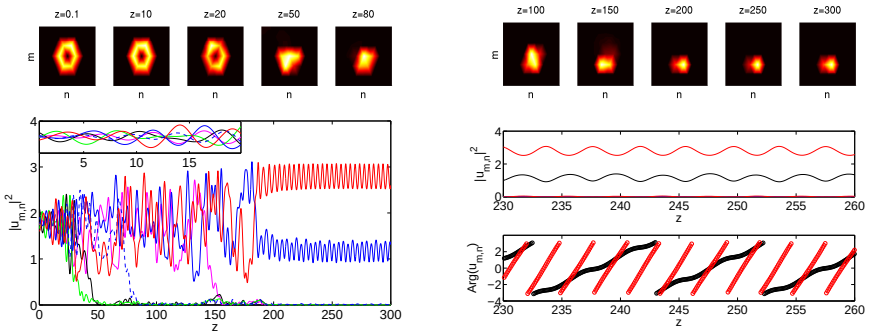

Figure 30. The same set of figures as in Figure 29 (top row, left panels) except for the solution from the out-of-phase family in the bottom row of Figure 23 are shown, also for $\varepsilon = 0.1$. On the right a closeup of the amplitude oscillations (top) and phase correlation (bottom) present in the remaining breather is given. As one can see, the distance until the initial configuration breaks down is much longer than for the in-phase case, as expected from the linear stability analysis (cf. the inset here and in Figure 29). The ultimate surviving configuration here contains a two-site breathing structure (see bottom left panel of the intensity evolution), in which there is a difference in amplitude and the phases of the the two sites are the same when the amplitudes are closer and opposite when they are further apart.

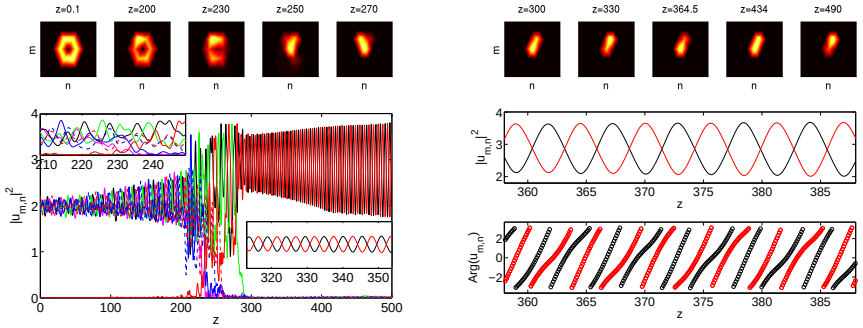

Figure 31. The same set as the previous images, this time for a solution from the charge-two family from the bottom panels of Figure 24 with $\varepsilon = 0.125$, i.e., large enough that a quartet of eigenvalues emerges. The long distance until initial breakup confirms the linear stability analysis, but a two-site (including the initially unpopulated center site) breathing structure persists after the disintegration of the initial structure. The inset panels show closeups of the amplitudes for shorter and longer propagation distances, respectively. In the right panels, one can observe that these two sites remain usually out of phase as their amplitudes oscillate.

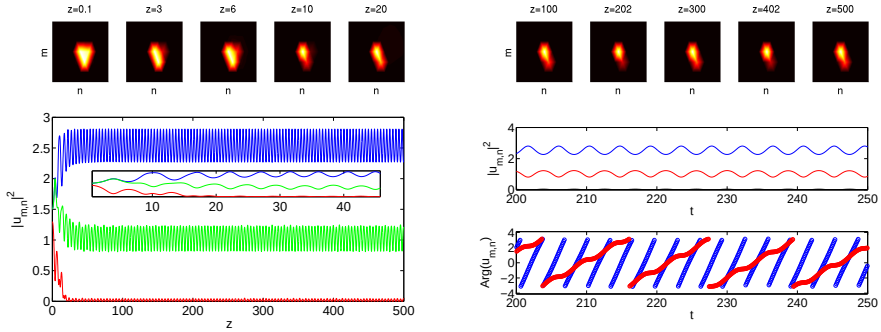

Figure 32. The in-phase, three-site configuration from the third row of Figure 25 is shown, in which a two-site breather persists for long propagation distances. The phases are correlated like the other unequal amplitude two-site breather which resulted in the evolution of the out-of-phase hexapole shown in Figure 30, in which they become in-phase and out-of-phase depending on whether their amplitudes are similar or considerably different, respectively.

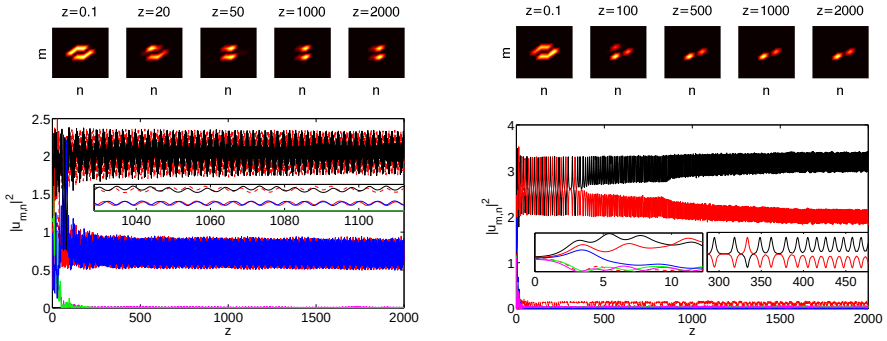

Figure 33. The evolution of the in-phase six-site configuration with the honeycomb lattice geometry from the top row of Figure 26 is given above (left) for $\varepsilon = 0.1$ and (right) for $\varepsilon = 0.3$. As in the hexagonal case shown in Figure 29 for $\varepsilon = 0.1$ a multi-site structure persists over a long distance, although now it is comprised of four sites, two pairs of out-of-phase breathers with comparable amplitude (the phase structure is not shown, but each pair is comparable with that of Figure 31). This interesting difference inspired us to continue the dynamical evolution for a longer distance, and the structure did indeed persist up to another order of magnitude. Even with the much larger perturbation of 25% of the initial amplitude (not shown) as opposed to 5%, a very similar four site structure persists for a long distance, although the degeneration of the other two sites is very rapid. The same robustness to perturbation is found for $\varepsilon = 0.3$, although a two site unequal amplitude breather remains, which oscillates between in-phase and out-of-phase (not shown, but same as the unequal amplitude breather in Figure 30).

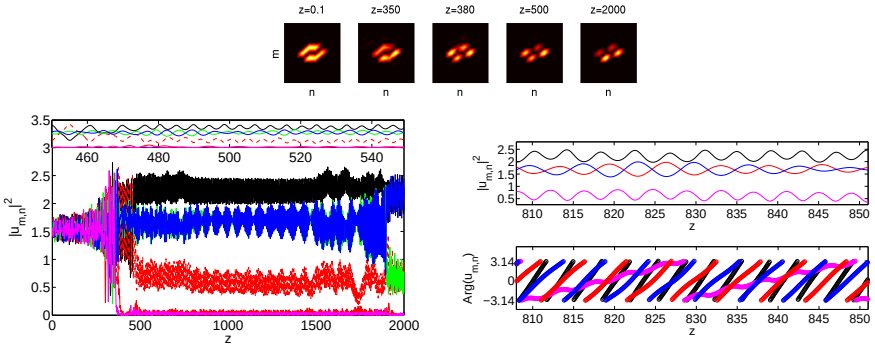

Figure 34. The six-site double-charged honeycomb lattice vortex for $\varepsilon = 0.135$ from the bottom set of panels in Figure 27 is significantly more stable than the single-charged counterpart. All original sites remain populated for a long distance, up to $z = 400$, and, when the two sites eventually decrease in amplitude, the remaining four reshape into a four-site breather. Two of the sites remain close in amplitude and out-of-phase, while one has larger and the other has smaller amplitude and these oscillate between in-phase and out-of-phase in the same manner as the others, such as those in Figure 30 (see panels on the right). The inset features a closeup image of the complex oscillations of the four sites. At a very long distance, close to $z = 2000$, they reshape in amplitude and phase, becoming two pairs of out-of-phase breathers, like the in-phase hexapole from Figure 33 ultimately does, although the dynamics is not followed further to see if this structure persists.

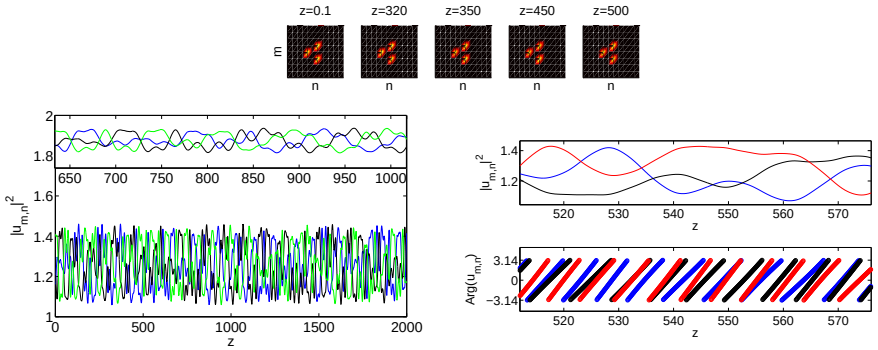

Figure 35. The dynamics for the $0, \pi, 0$ honeycomb lattice configuration from the top rows of Figure 28 for $\varepsilon = 0.1$ This solution persists for very long propagation distances despite the linear instability. Moreover, the relative phase structure persists, although the one site that is out-of-phase with the other two oscillates from one to another among the three (see the right panels).

CHAPTER 4

HEXAGONAL AND HONEYCOMB LATTICES (CONTINUUM)

We now consider the continuum setting with a saturable nonlinearity for the cases of lattices with 3 and 6 principal neighboring directions. The main results are the following:

- The predictions are confirmed in the continuum for both focusing and defocusing saturable nonlinearity in hexagonal and honeycomb lattices, where solutions predicted to be stable have intervals of stability and complex quartets of eigenvalues, and typically intersect with unstable solutions having out-of-phase nearest neighbors (in the defocusing case, and the in-phase nearest neighbors in the focusing case) in saddle-node bifurcations, much like in the square lattice.

- The dynamical evolution is not always a-priori understood from the linearized spectrum and unstable strongly nonlinear solutions can exhibit relatively stable dynamics.

- The solutions with non-trivial current are confirmed to exist and be relatively robust in experiments, although propagation distances available in ex-

periments are far shorter than the length scales for which instabilities are expected to manifest.

4.1 Continuum honeycomb lattice

First we consider the setting of a honeycomb photonic lattice induced in a photo-refractive crystal with saturable defocusing nonlinearity. The principal lattice vectors of Eq. (5.1) are the same as the 3 principal directions of the discrete honeycomb lattice. In other words, we have $\mathbf{b}_1 = (1, 0)$, $\mathbf{b}_2 = (-\frac{1}{2}, -\frac{\sqrt{3}}{2})$, and $\mathbf{b}_3 = (-\frac{1}{2}, \frac{\sqrt{3}}{2})$. In fact, this lattice has the structure of both the honeycomb and hexagonal lattices as its minima and maxima, respectively, when the nonlinearity is defocusing, while the opposite is true when it is focusing. In the next section, we will consider this case. Here we have that d is the period in the x direction with $k = 4\pi/(3d)$ and the period in the y direction is $\sqrt{3}d$ in the definitions given below Eq. (5.1).

We choose the lattice intensity $I_0 = 0.6$. A plot of the optical lattice is shown in Figure 36 for illustrative purposes regarding the location where our localized pulses will be "inserted". In addition, we choose other physical parameters consistently with a typical experimentally accessible setting [37] as

$$d = 30\mu\text{m}, \quad \lambda = 532 \text{ nm}, \quad n_e = 2.35, \quad E_0 = 8, \quad D = 18.01.$$

The numerical simulations are performed in a rectangular domain corresponding to the periodicity of the lattice using a rectangular spatial mesh with $\Delta x \approx 0.75$ and $\Delta y \approx 0.86$ and domain size $4d \times 3\sqrt{3}d$, i.e. 160×180 grid points. See Figure 36 for a schematic of the spatial configurations.

Regarding the typical dynamics of a soliton when it is unstable, we simulate the z-dependent evolution using a Runge-Kutta fourth-order scheme with a step $\Delta z = 0.01$.

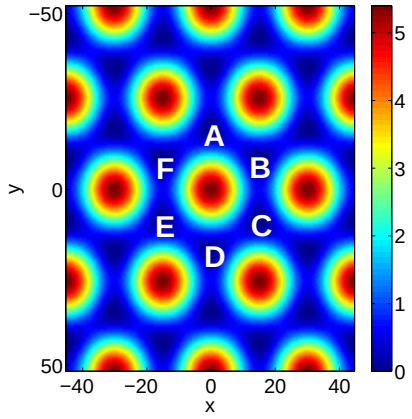

Figure 36. A spatial (x-y) contour plot of the ordinary polarization standing wave [lattice beam in Eq. (5.1)]. In this context, the light intensity maxima correspond to the minima of the resulting refractive index lattice (i.e., honeycomb lattice), as opposed to the focusing nonlinearity lattice field, where they correspond to the maxima (i.e., triangular lattice). Points A, B, C, D, E, and F are used for naming the various configurations. A is a "nearest-neighbor" minimum of B and F, a "next-nearest-neighbor" of C and E, and an "opposite" of D (with respect to the local maximum of the lattice). Because of the symmetry of the setup, this is a complete characterization of dipole configurations. We will refer to the configurations with the names given above.

Again, the localized states u of (1.6) were obtained using the Newton-GMRES fixed point solver nsoli from [43] and a pseudo arc-length continuation [44] was used to follow each branch and locate the bifurcations which occur at the edge of the first band. Since the parameter of interest is μ, diagnostics are plotted against μ.

Using a standard eigenvalue solver package implemented through MATLAB, we identify the spectral gap for our given parameters and gridspace to be $3.62 \lesssim \mu \lesssim$

4.94.

4.1.1 Nearest Neighbor Dipole Solitons

In this section, we report dipole solitons where the two lobes of the wave are located in two nearest neighbor (N) lattice sites in the 2D triangular potential shown in Figure 36. The lobes can have the same phase or π phase difference so we define them as in-phase (IP) dipoles and out-of-phase (OP) dipoles, respectively.

We have found IP dipoles in adjacent wells for values of the propagation constant μ throughout the entire Bragg reflection gap for a given E_0. We found that the solitons exist for μ between 3.62 and 4.94, and that the intensity of the dipoles cannot be arbitrary low, a result similar to the observed results of the focusing and defocusing cases for square lattices [15, 42, 65]. The relevant findings are summarized in Figure 37.

The top left panel of Figure 37 shows the stability of the dipoles against the propagation constant μ, by illustrating the maximal growth rate (maximum real part of all eigenvalues λ) of perturbations. When $\max(\mathrm{Re}(\lambda)) = 0$, this implies stability of the configuration, while the configuration is unstable if $\max(\mathrm{Re}(\lambda)) \neq 0$ in this Hamiltonian system. We found that this type of dipole may be stable for windows throughout the first spectral gap, as predicted above, although it is possible for small oscillatory Hopf instabilities to arise due to opposite signature eigenvalue collisions. The dipole configuration disappears in a saddle-node bifurcation at the edge of the first spectral band, depicted in the top panels of Figure 37, as $\mu \to 4.94$, and a real pair of eigenvalues emerges. At this point, the configuration collides with a configuration shown at the bottom panel of Figure 37 in which the adjacent well next to one of the populated ones becomes excited out-of-phase with the others. Consistent with our theoretical expectation from its having an out-of-phase set of

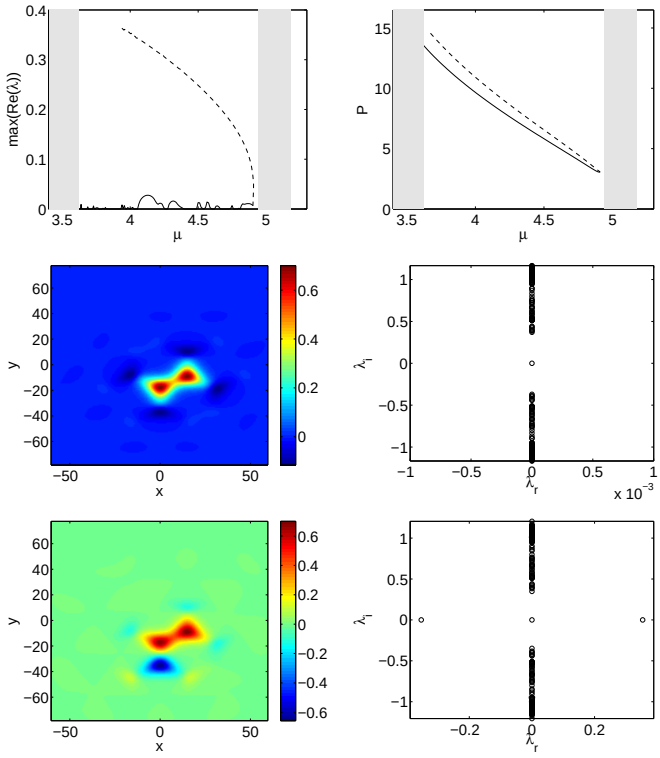

Figure 37. The top left panel shows the stability of the dipoles against the propagation constant μ. It is stable when the spectra is purely imaginary (i.e., when $\max(\mathrm{Re}(\lambda)) = 0$). The top right panel depicts the power of the dipoles against the propagation constant. In each of these images the solution branch is denoted by a solid line. The branch with which the dipole collides and terminates in a saddle-node bifurcation is shown by a dashed line. The shaded areas in both of these panels represent the bands of linear spectrum (1.9). The middle left and right panels show the profile u of the dipole at $\mu = 4$ and the corresponding complex spectral plane $(\mathrm{Re}(\lambda), \mathrm{Im}(\lambda))$ of $\lambda = \mathrm{Re}(\lambda) + i\mathrm{Im}(\lambda)$. Finally, the bottom panels show the same features for the unstable saddle solution corresponding to the dashed line.

nearest neighbors, the latter configuration always has a real pair of eigenvalues λ.

The middle left and right panels show the profile u of the in-phase nearest (IPN) neighbor dipole at $\mu = 4$ and the corresponding spectrum of linearization eigen-

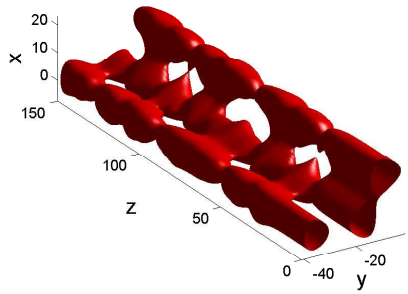

Figure 38. The typical time-dependent dynamics of an unstable configuration along the upper (dashed line) branch of the existence curve presented in the top panels of Figure 37. Depicted here is the isosurface of height 0.15 of the dynamics of the of the intensity, $|U|^2$, of the configuration shown in the bottom panel of Figure 37.

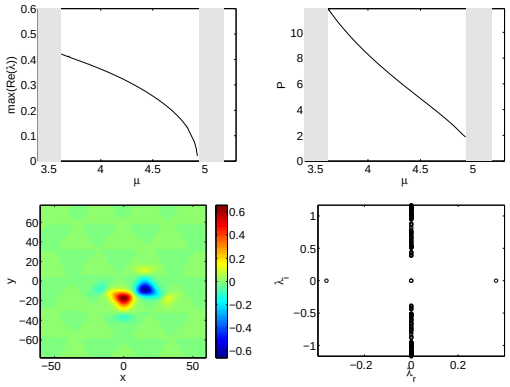

Figure 39. The top panels correspond to the same panels of Figure 37 but for OPN dipole solitons. The bottom panels show the profile u and the corresponding spectral plane of the dipoles at $\mu = 4$.

values $\lambda = \lambda_r + i\lambda_i$ in the complex plane (λ_r, λ_i), respectively. The corresponding profile and spectral plane for the saddle branch (that eventually collides with the IPN solution) at $\mu = 4$ is shown in the bottom left and right panel, respectively, of the same figure, illustrating the exponential instability of the latter.

We have simulated the dynamics of the solitary waves when they are unstable.

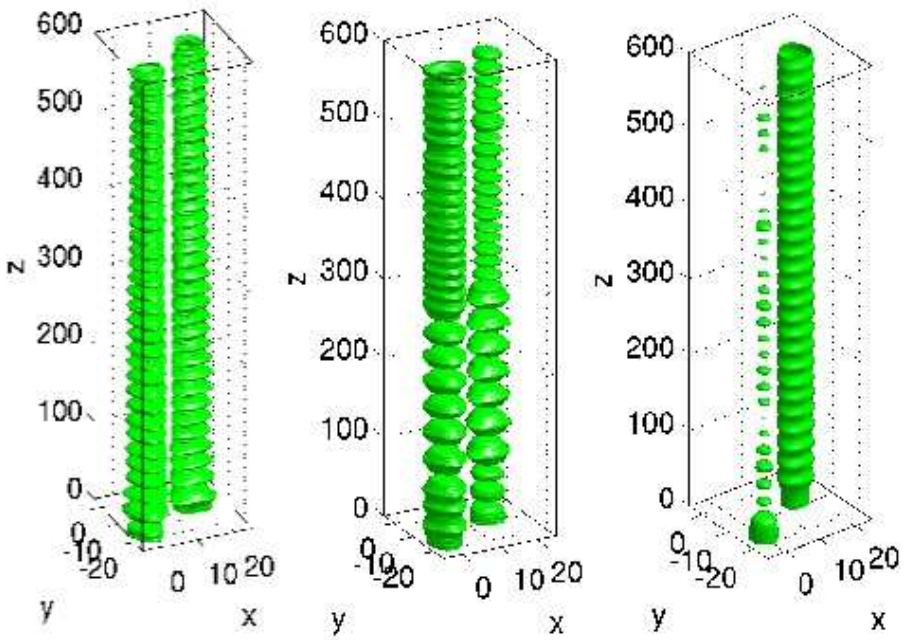

Figure 40. The typical dynamical evolution of an unstable out-of-phase nearest neighbor configuration from the family presented in Figure 39. Depicted is the isosurface at half the maximum of the intial intensity amplitude. Notice that the OPN appears to oscillate between two sites and one for the propagation constant $\mu = 4$ (center) of the solution presented in the bottom panels of Figure 39, as it does for smaller values ($\mu = 3.6$, left), although for a larger value of $\mu = 4.6$, right, the solution essentially transforms (due to the instability) into a single site mode.

The dipoles are perturbed by a random noise with maximum intensity 2×10^{-3}. It is interesting to note that an unstable IPN dipole turns out to be quite robust, even though it experiences only an oscillatory instability. It is remarkable that up to $z = 200$ we did not see any significant change in the configuration. Therefore, we do not depict our evolution simulation here; we simply note that this is consonant with the very weak growth rate of the relevant oscillatory instability.

For the solution branch shown in the bottom panel of Figure 37, we present its dynamics in Figure 38. We found that the instability is strong as predicted above

such that even after a relatively short propagation distance, the instability already sets in and leads to recurrent oscillations (for the remainder of our dynamical evolution horizon) between a dipole, two-site state and a three-excited-site state; see Figure 38.

We have also found OP dipoles arranged in nearest-neighboring lattice wells which we refer to as OPN. We summarize our findings in Figure 39 where one can see that the solitons exist in the whole entire region of propagation constant μ in the first Bragg gap, $\mu \in (3.62, 4.94)$. This smooth transition indicates that the OPN dipole solitons emerge out of the Bloch band waves; see e.g. [48] and [49] for a relevant discussion of the 1D and of the 2D problem respectively, in the case of the cubic nonlinearity. The OPN dipoles are unstable due to a real eigenvalue pair, as expected from our above theoretical predictions.

As the branch merges with the band edge, we observe an interesting feature, namely that the configuration begins to resemble a hexapole with a π phase difference between each well. This can be an indication that these structures bifurcate out of the Bloch band from the same bifurcation point.

In Figure 40 we present the unstable dynamics of OPN dipole solitons perturbed by similar random noise perturbation as in Figure 38. We display here three solutions for a range of chemical potentials to illustrate that the dynamical evolution of linearly unstable states is apparently correlated to the power of the solution. This type of dipoles is typically more unstable than its IP counterpart, as is illustrated in the figure. In particular, in all three examples of unstable evolution given, the instability already starts to manifest itself around $z = 20$. However, for small values of μ (large power) the OPN continues oscillating between a single site structure and a two site structure for the (longer) evolution distances investigated in this illustrative case, while for large enough μ (small enough power), one of the

sites decays and the power is concentrated on a single site.

4.1.2 Next Nearest Neighbor Dipole Solitons

We have also obtained dipole solutions that are not oriented along the two nearest-neighboring lattice wells, but rather where the two humps of the structure are located at two next-nearest-neighboring lattice sites. These humps can once again have the same phase or a π phase difference between them. We will again use the corresponding IP and OP designations for these next nearest neighbor waveforms.

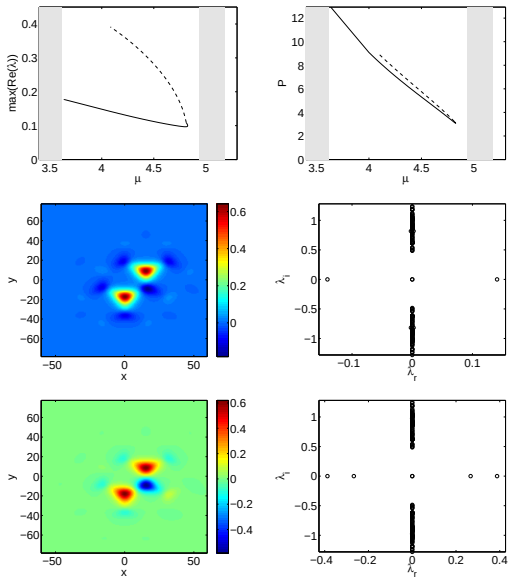

Figure 41. The top panels correspond to the same diagnostics as in Figure 37 but for IPNN dipole solitons. The middle panels show the profile U and the corresponding spectral plane of the IPNN dipole at $\mu = 4.1$, while the bottom row shows the same images for the solution branch corresponding to the dashed line in the top panel, shown at the same value of μ.

The in-phase next-nearest (IPNN) neighbor solitons exist only up to a marginal distance from the second band. The stability and power of these dipoles are shown

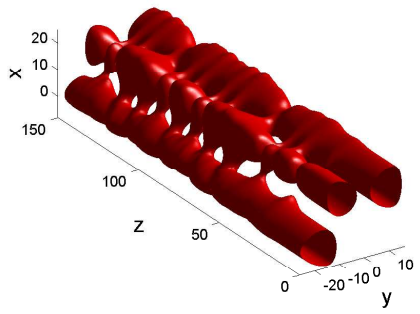

Figure 42. The same as Figure 38, but for the solution presented in the bottom panel of Figure 41. Depicted is the isosurface of height 0.05**.**

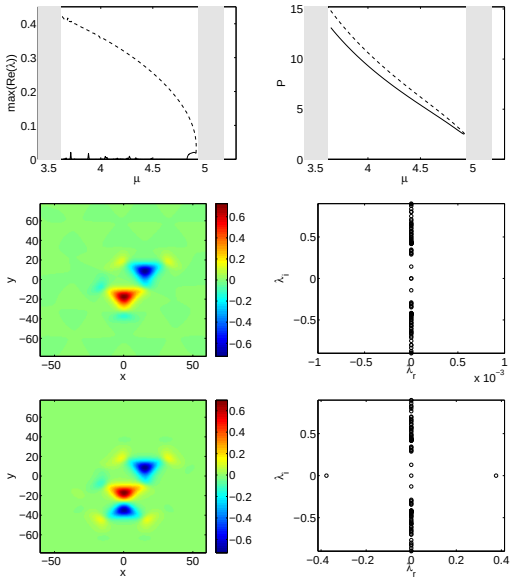

Figure 43. The top panels depict the largest real part of the critical eigenvalue, as well as the power of the OPNN dipole solitons. The middle panels show the profile u **and the corresponding spectra in the complex plane of the dipole at** $\mu = 3.9$**, and the bottom is the unstable saddle configuration at the same value of** μ**, where one of the sites has merged with a neighbor out of phase and become an OPN, accounting for the real eigenvalues.**

in Figure 41. In particular, the IPNN configuration always possesses a real eigenvalue pair; furthermore, the corresponding unstable "saddle" structure with which

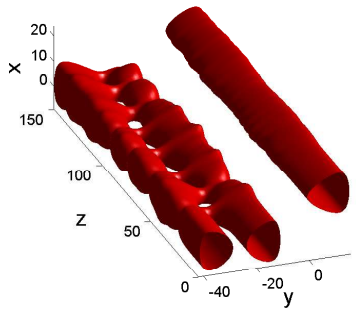

Figure 44. The same as Figure 38, but for the solution presented in the bottom panel of Figure 43. Depicted is the isosurface of height 0.05**.**

it collides and terminates through a saddle-node bifurcation has an additional such eigenvalue pair (two real eigenvalue pairs in total for the solution branch indicated by dashed line in Figure 41).

We have simulated also the dynamics of the unstable IPNN. Yet, we do not present our simulation here as the typical evolution of this configuration is quite in resemblance to the dynamics of an unstable OPN (see Figure 40) in the fact that the configuration recurrently oscillates between a two-soliton state and a one-soliton state. Such an oscillation persists even up to $z = 200$.

In Figure 42, we present the dynamical evolution of the bifurcating solution shown in the bottom panel of Figure 41 under similar random noise perturbation as above. One can note similarities in the typical evolution of this configuration and the evolution of the bifurcating IPN solution shown in Figure 38, one of which is the recurrent oscillation between a pattern with three pulses and one with just two peaks.

We have also obtained out-of-phase, next-nearest (OPNN) neighbor dipole solitons. A typical profile of this family of solutions for $\mu = 3.9$ is shown in Figure 43. The power diagram of these solitons is presented in the top panel of Figure 43.

Typically these structures are stable (as indicated again by the comparison with the theoretical discussion and by the numerical results shown in the middle right panel of Figure 43), suffering only windows of oscillatory instability due to the presence of a single eigenvalue with negative signature and its collision with the spectral bands In fact, we have found that a consistent stability range for $E_0 = 8$ exists between $4.5 \lesssim \mu \lesssim 4.85$.

For this solution we also observe that, similarly to the IPNN dipoles, the solution disappears at non-zero intensity because of the collision of this dipole with another (three-site) configuration shown in the bottom panels of Figure 43 in a saddle-node bifurcation. It is relevant to note that the point of the bifurcation is very close to the edge of the Bloch band, i.e., to $\mu \approx 4.94$.

The dynamics of the OPNN dipole do not manifest their very weak oscillatory instability for the evolution distances considered herein. On the other hand, the dynamics of the instability of the three-site solution (with which the OPNN branch collides in the saddle-node bifurcation) can be seen in Figure 44. More specifically, the instability manifests itself in the form of interactions between the closest out-of-phase pair of solitons (leading to recurrent oscillations between a three-peak and a two-peak state). Notice that the third peak is almost not affected by these interactions.

4.1.3 Opposite Dipole Solitons

We now address opposite (O) dipole solitons residing at the two sites along a diameter of a local maximum of the lattice. This is the final type of dipole configuration for a symmetric triangular lattice, exhausting the possibilities up to phase and rotational invariances. Again, we partition our considerations into in-phase and out-of-phase cases.

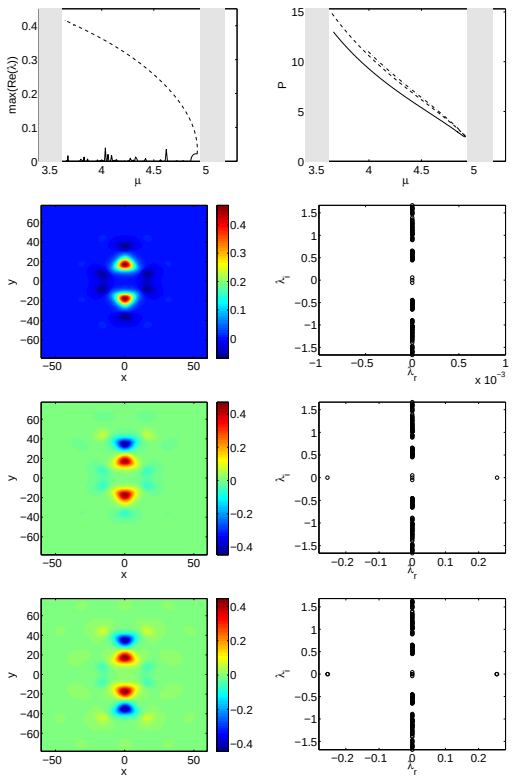

Figure 45. The top panels depict the largest real part of the critical eigenvalue, as well as the power and the peak intensity of the IPO dipole solitons. The panels in the second row show the profile u and the corresponding spectra in the complex plane of the dipole at $\mu = 4.5$, the third row shows the same images at the same value of μ for the middle branch (dashed line) of the bifurcation diagram and the bottom row is a solution along the top branch (dash-dotted line) at the same value.

We have found in-phase opposite (IPO) solitons throughout the first gap in the linear spectrum. Our numerical findings are presented in Figure 45.

Again, the solution branch is largely stable with small windows of Hopf quartets and again a saddle node bifurcation occurs as the branch approaches the first spectral band. Also, interestingly, the configuration with which this branch collides when it disappears resembles an OPN (or two pairs of OPNs– see the third and

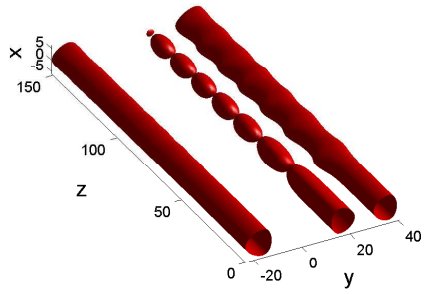

Figure 46. The same as Figure 38, but for the solution presented in the middle panel of Figure 45. Depicted is the isosurface of height 0.05**.**

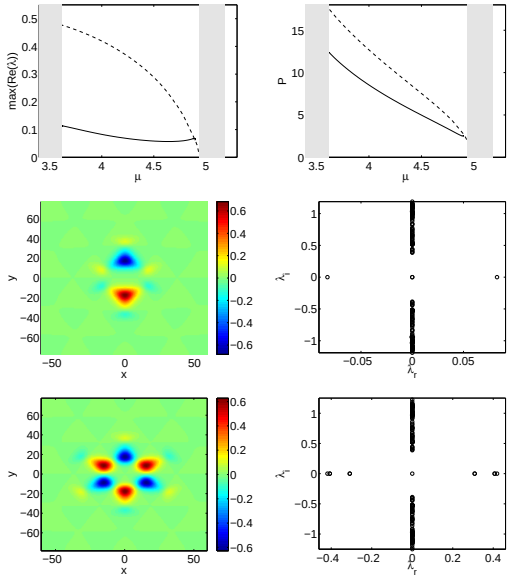

Figure 47. The top panels depict the largest real part and the power of the OPO dipole solitons. The middle panels again show the profile u **and spectra at** $\mu = 4$**, and the bottom is the more unstable saddle configuration, consisting this time of a hexapole configuration constructed out of three such OPOs.**

fourth row of the figure). The latter branches are naturally unstable due to one (or more) real pair of eigenvalues.

The dynamics of one of the bifurcating solutions, i.e. the configuration with a

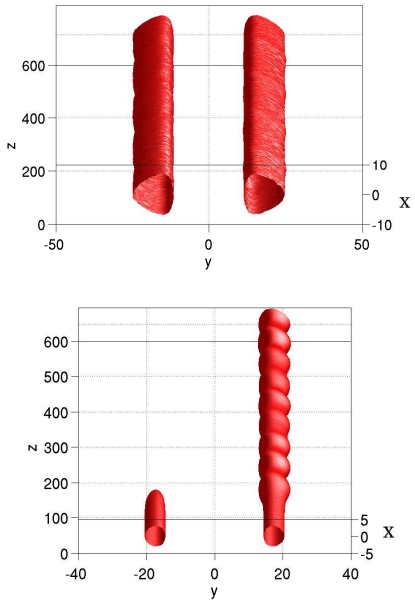

Figure 48. The top panel is the same as Figure 38, but for the solution presented in the middle panel of Figure 47, with isosurface of height 0.1**. The bottom row is the evolution of the solution from this branch, with a comparable instability growth-rate, for** $\mu = 4.88$

single OPN structure, is presented in Figure 46, where one can see that, as usual, only the pair of out-of-phase nearest neighbor dipole interacts, while the other soliton is almost uninfluenced.

Using the same reasoning, one can deduce as well that the dynamics of the other bifurcating solution, presented in the bottom panel of Figure 45, will be similar, except the fact that now there are two pairs of OPN interacting among themselves.

Lastly, as regards dipoles, we consider the out of phase opposite (OPO) dipole. The first interesting characteristic of the OPO is its strong instability stemming from a real pair of eigenvalues, seen in the top left and middle rows of Figure 47. On the other hand, the figure also reveals an interesting bifurcation structure in this case. The branch actually merges with a hexapole made of three copies of itself

close to the band, when solutions start becoming extended. This hexapole then intersects with the linear spectrum shortly thereafter and the solution transforms itself into a fully extended "checkerboard"-like configuration of all adjacent wells excited out-of-phase. As can be seen in the top left and the bottom right of Figure 47, the hexapole configuration is significantly more unstable, possessing five real eigenvalue pairs.

We have numerically monitored the full evolution to observe the dynamics of the unstable OPO dipoles. It is interesting to note that even though the state has a pair of real eigenvalues, our simulation reveals that the instability is barely detectable for the state depicted in the middle rows of Figure 47, presumably because of the spatial separation of the populated sites (top row of Figure 48); the solution oscillations are very mild (and almost indetectable) between similar structures with mass concentrated in one site or another. On the other hand, for significantly smaller power (larger μ) as seen in the bottom panel of Figure 48, one site decays fairly rapidly and a robust single site remains. This illustrates again (c.f. Figure 40) that the linear stability analysis is more predictive of the nonlinear dynamics for the solution with the larger value of $\mu = 4.88$ (and accordingly smaller amplitude) close to the intersection with the extended OP quadrupole branch (the isosurface is taken at half the maximum of the initial intensity amplitude). The growth rates for each solution are comparable, while the dynamical evolutions differ drastically.

Regarding the bifurcating solution, which is an out-of-phase hexapole, we will explore it as well as the other hexapole configurations in more detail in the following section.

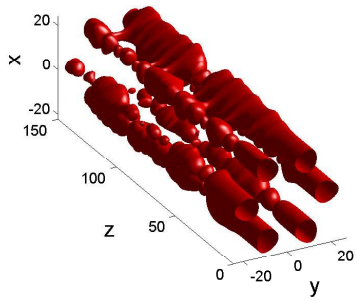

Figure 49. The same dynamical evolution figure as Figure 38, but for the out-of-phase hexapole depicted in the bottom panel of Figure 47. Depicted is the isosurface of height 0.1.

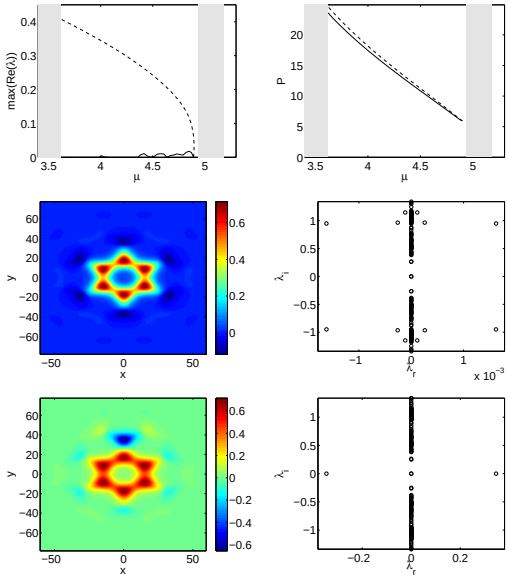

Figure 50. The top panels depict the largest real part and the power of the IP hexapole solitons. The middle panels again show the profile u and spectra at $\mu = 4$, and the bottom is the more unstable saddle configuration, which features an OPN sidekick.

4.1.4 Hexapole Solitons and Vortex Necklaces

First, we consider the out-of-phase hexapole. The existence and the stability of this configuration has been described in the preceding section. As the state has

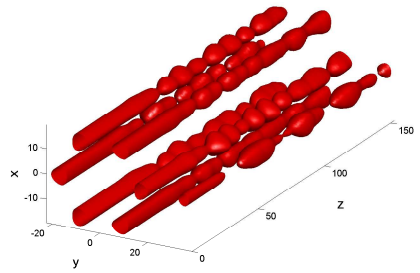

Figure 51. The same figure as Figure 38, but for the in-phase hexapole depicted in the bottom panel of Figure 50. Depicted is the isosurface of height 0.3**.**

multiple pairs of real eigenvalues, it is natural to expect that it should be prone to break up under the instability's dynamical evolution. A typical example of such a numerical experiment is presented in Figure 49.

We found IP hexapole configurations as well, which turn out to chiefly be stable within the first gap, although they may possess weak oscillatory instability inducing eigenvalue quartets.

This configuration also suffers a saddle-node bifurcation with an OPN-type pair emanating off of one of its lobes, when a neighboring well becomes populated out of phase near the first band. The latter configuration is unstable, always possessing a real eigenvalue pair in its linearization spectrum. We note in passing that this is among any of the six equivalent symmetric versions of this configuration. As for the dynamics of the instability, the solution along the main lower branch is quite robust to strong perturbation. Even though the solution suffers from an oscillatory instability, a random perturbation with a maximum intensity almost 10^{-1} cannot lead to a breakup of the configuration until propagation distances of the order of $z = 200$. On the other hand, the oscillatory dynamics leading to the break up of the configuration of the bottom panel of Figure 50 is shown in Figure 51.

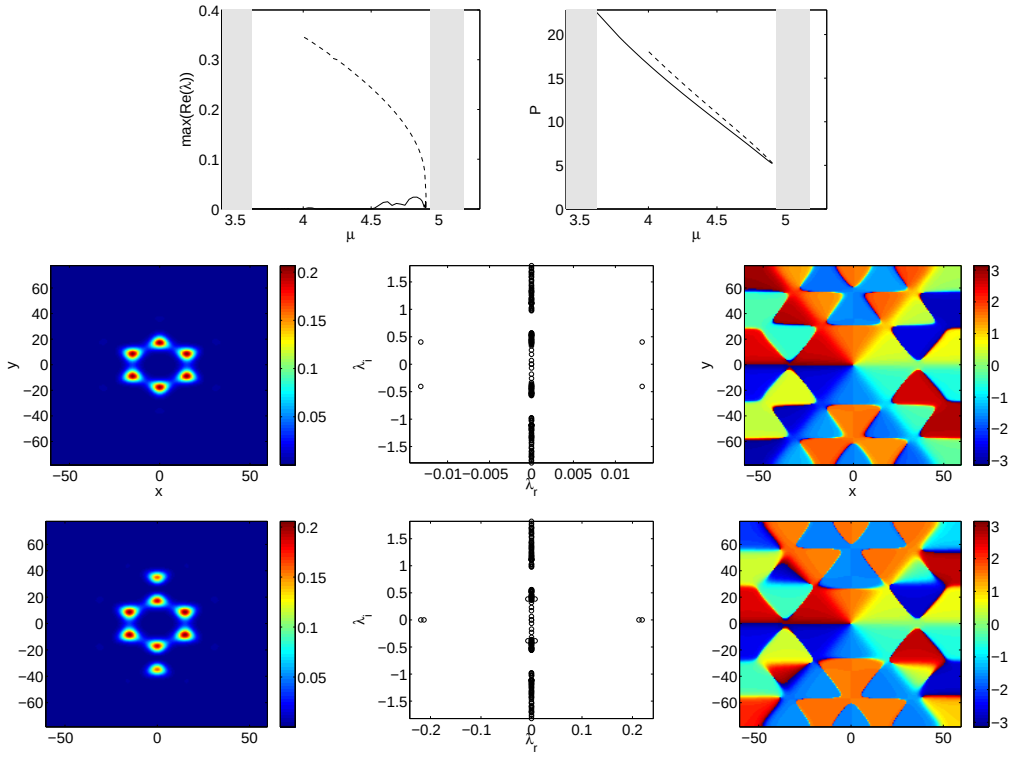

Figure 52. The top panels depict the largest real part and the power of the $S = 1$ vortex configuration. The second row depicts the modulus of the solution, corresponding spectrum when $\mu = 4.6$, and phase (from left to right). The third row shows the same properties as the second but for the unstable eight-site vortex configuration of the dashed line in the top panels.

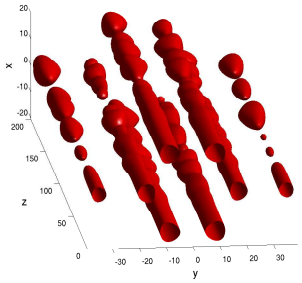

Figure 53. The same figure as Figure 38, but for the vortex structure with eight lobes depicted in the bottom panel of Figure 52. Depicted is the isosurface of height 0.1.

Finally, we investigate the complex-valued hexapole configuration for which each lobe has the same modulus and their phase increases counterclockwise in phase increments of $\pi/3$, yielding a vortex-necklace configuration. This configuration turns out to be stable for the most part within the first gap as well, with minor Hamiltonian Hopf-bifurcation induced oscillatory instabilities. We also found that this solution undergoes a saddle-node bifurcation near the first band, in which it collides with a waveform with two pairs of OPNs. The instability of the latter configuration in the presence of these additional OPN dipoles is consistent with that of their real counterparts from the previous sections, each appearing to contribute one real pair, rendering the relevant configuration quite unstable.

Similar to the case of in-phase hexapoles, even though vortex necklaces may be unstable, they are quite robust to perturbation, given the weak nature of the relevant oscillatory instabilities. We therefore only depict the dynamics of the solutions which have eight lobes as shown in the fourth and fifth row panels of Figure 52. The typical evolution of this state is shown in Figure 53, showcasing the oscillatory breakup of this structure into one with a smaller number of lobes.

4.2 Continuum hexagonal lattice

In this section, we study single- and double-charge discrete optical vortices in non-square periodic photonic lattices [24, 32, 25, 30, 33, 66]. In particular, in the framework of the continuous nonlinear model of optically-induced lattices generated in saturable nonlinear media, we analyze the existence, stability and dynamical properties of discrete optical vortices in the continuum for the case of hexagonal optical lattices. We verify that the double-charge vortex is indeed stable in the presence of a focusing nonlinearity, while the single charge one is unstable, as can

be easily understood based on the discrete results. We confirm this finding by demonstrating numerically the generation of a double-charge vortex with realistic experimental parameters.

It is particularly important to highlight that although our results will be given with a view towards applications in photorefractive crystals, they are not only relevant to that setting but also directly applicable to two-dimensional hexagonal waveguide arrays (e.g., in glass), showcased in recent experiments (see e.g., [31] and references therein). Furthermore, they are likely to have direct implications to other areas of physics, such as Bose-Einstein condensates (BECs) in triangular lattices, the first experiments of which have just been realized [67], or even Debye crystals in dusty plasmas [62].

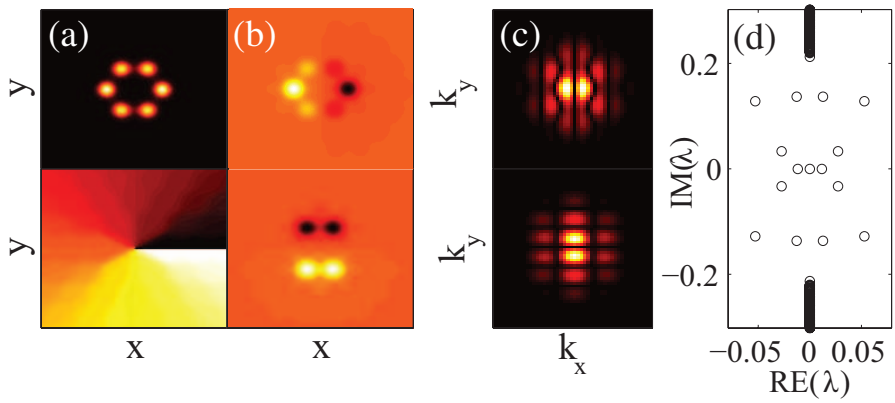

Figure 54. Example of an always unstable single-charge discrete optical vortex for $\beta = -0.76$ (marked by a circle in Figure 55). (a) Intensity (top) and phase (bottom); (b) real (top) and imaginary (bottom) components; (c) absolute value of the corresponding Fourier transforms; (d) spectrum of the linearized equation displaying the linear instability of the configuration due to the presence of positive real parts in a number of eigenvalues λ in the spectrum.

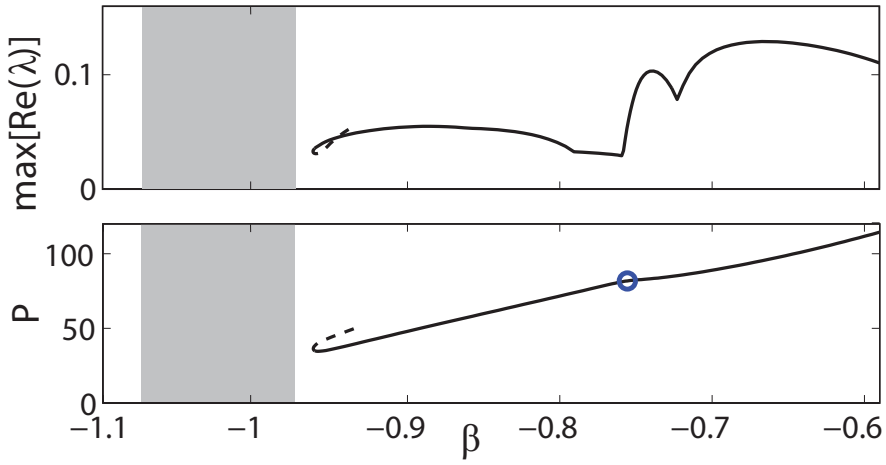

Figure 55. Family of single-charge vortices vs. propagation constant β. Top: maximum real part of the linear stability spectrum. Bottom: power $P = \int |U|^2 dxdy$. The circle corresponds to the discrete vortex given in Figure 54. The dashed line indicates another unstable branch which, for larger β bifurcates into different configurations.

4.2.1 Theoretical Setup

We study beam propagation through a self-focusing nonlinear medium in the presence of a two-dimensional hexagonal lattice by employing the continuum model with a saturable nonlinearity. To render our setting completely amenable to the experimentally accessible regime, we use the theoretical model of a photorefractive nonlinear medium, which is known to exhibit a strong saturable nonlinearity [25]. Polarization anisotropy of the nonlinear photorefractive response enables one to optically imprint various types of refractive index modulation (optical lattice) which can then be probed by an external beam [13]. Then the propagation of this beam in the presence of an optically-induced hexagonal refractive index pattern is governed by the normalized evolution Equation (1.1) with $\mathcal{N}(\mathbf{x}, |U|^2)$ defined in Eq. (1.4). The laser wavelength in vacuum is $\lambda = 532$nm, average refractive index of the

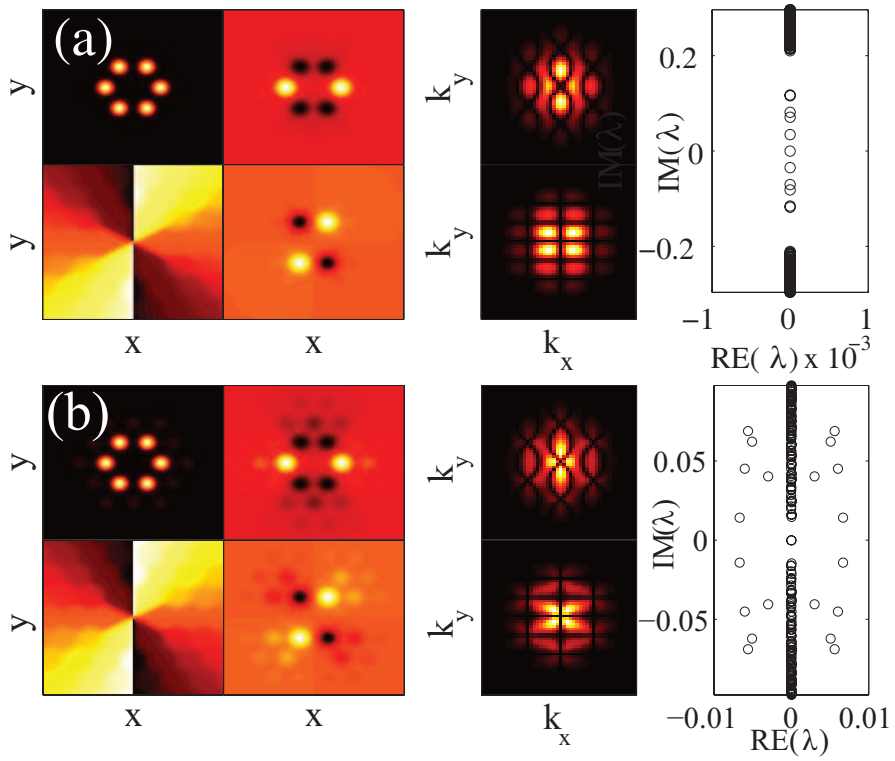

Figure 56. Examples of (a) stable and (b) unstable double-charge discrete optical vortices for $\beta = -0.76$ and $\beta = -0.96$ respectively (marked respectively by the circle and square in Figure 57). The layout of the panels is the same as in Figure 54.

medium $n_0 = 2.35$, $E_0 = 2.36$, $I_0 = 0.49$, and $k = 4\pi/3d$ with a lattice period $d = 30\mu$m.

We now look for stationary solutions in the form

$$U(x, y; z) = u(x, y) \exp(i\beta z) \exp(im\phi), \tag{4.1}$$

where u is real, β is the propagation constant, ϕ is the vortex phase, and m is the vortex charge. We solve the resulting nonlinear equation numerically, and the major results are summarized in what follows.

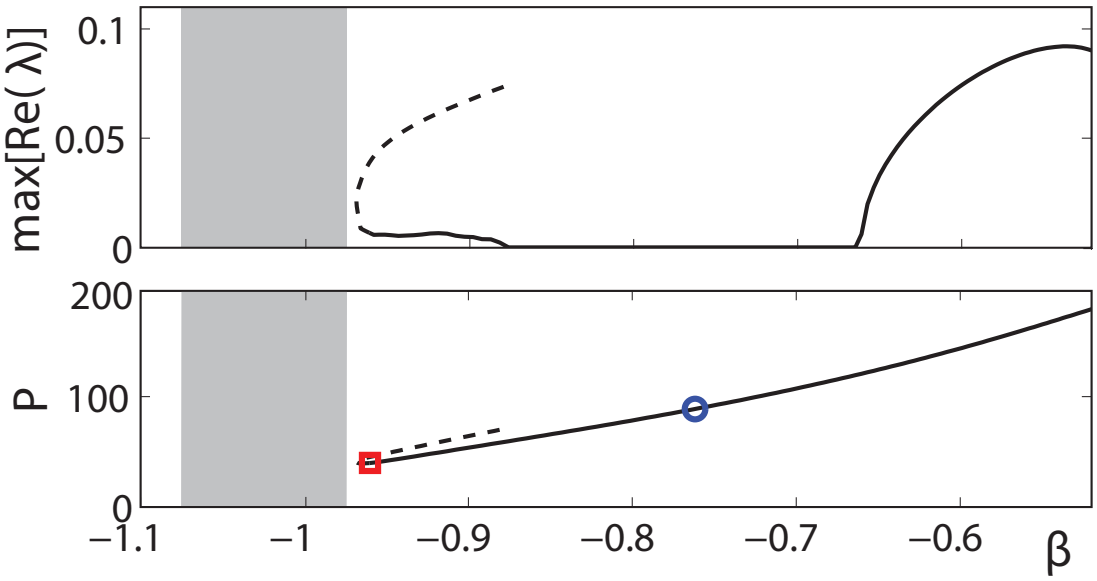

Figure 57. Family of double-charge vortices vs. propagation constant β. Top: maximum real part of linear stability spectrum [when nonzero, this denotes instability]. Bottom: power $P = \int |U|^2 dxdy$. The circle and square correspond to the stable and unstable discrete vortex configurations shown in Figure 56 ((a) and (b) respectively). The dashed line indicates an unstable branch which, for larger β bifurcates into different configurations.

4.2.2 Numerical Results

We begin by considering the simplest six-site vortex structure, that of a single-charge ($m = 1$) discrete vortex. Figure 54 illustrates a typical example, while Figure 55 shows the single-charge vortex linear stability (top) and power (bottom) as a function of the propagation constant in the semi-infinite band gap of the periodic potential. A positive real part of an eigenvalue in the linear stability spectrum leads to exponential growth of the corresponding linear excitation mode, and therefore to instability of the vortex. Somewhat surprisingly we can see in Figure 55(top) that the single-charge vortex has an eigenvalue with a positive real part across its entire region of existence, and therefore the single-charge vortex is

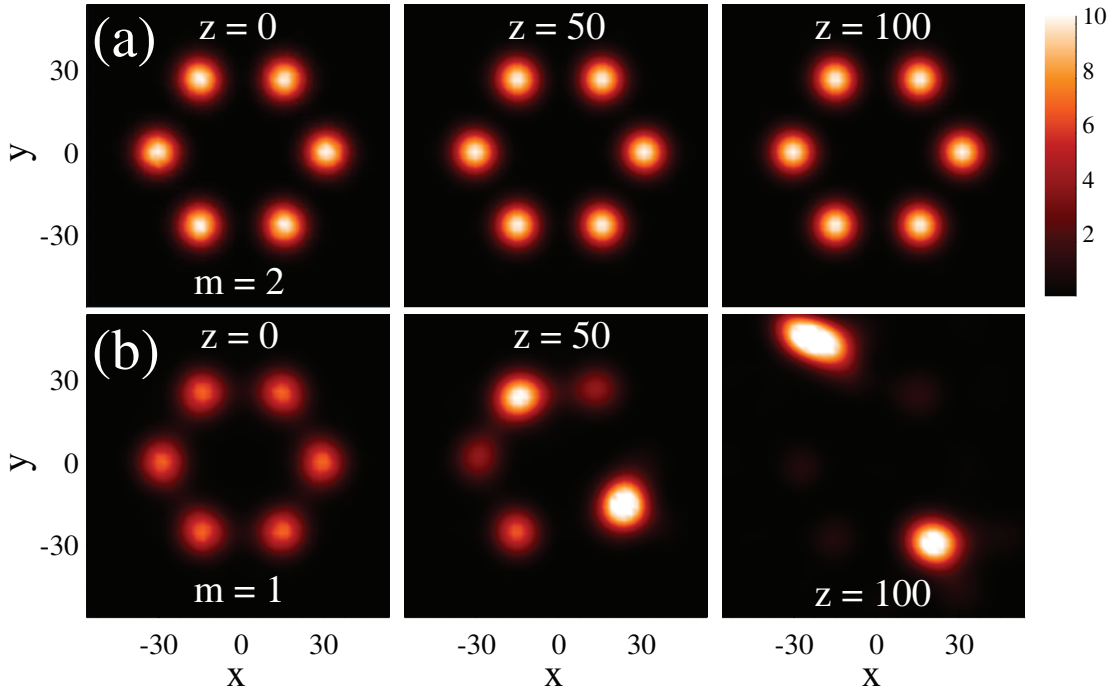

Figure 58. The top three panels (a) depict the evolution of a stable double-charge vortex configuration after a random perturbation with amplitude 5% of the initial amplitude. The bottom three panels (b) are the evolution of a single-charge vortex configuration. In both cases $\beta = -0.7$. The color bar on the right provides a scale of the intensity (note the intensities of the single-charge vortex are lower relative to (a) initially and saturated on this scale after break-up).

always unstable.

In contrast we find that double-charge vortices may be *stable* (see Figure 56(a)), and even where unstable the instability is weaker than the single-charge case (see Figure 57). In fact, as we can see in Figure 57(top) the double-charge vortex has a wide parametric interval where it is completely stable (from $-0.92 < \beta < -0.65$), while outside this range it is unstable due to weak oscillatory instabilities (complex unstable eigenvalues, as evidenced by the spectrum in Figure 56(b)). We note that neither the single- nor double-charge discrete vortex families degenerate into a

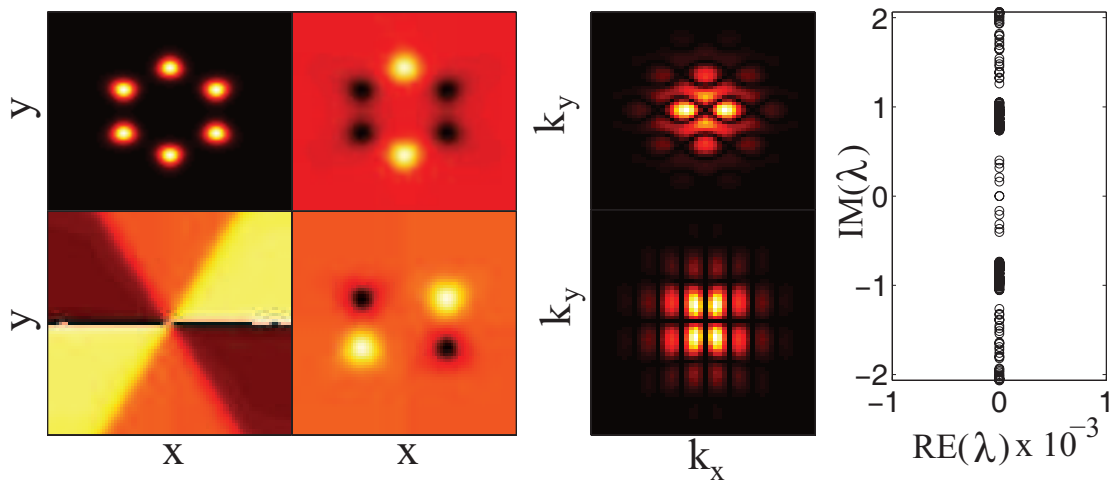

Figure 59. The same set of panels as in Figure 54 except for a stable double-charge vortex in a honeycomb lattice.

linear Bloch mode, as one can observe from the saddle-node bifurcation that occurs close to the edge of the first band of the linear spectrum in both Figure 55 and Figure 57. The various unstable single- and double-charge vortices which occur along the upper dashed branch in each figure are not discussed here. The typical evolution of the stable and unstable vortices is illustrated in Figs. 58(a,b). Even though the single-charge vortex is lower in power than the double-charge vortex, break-up of the former into single-site fundamental discrete solitons occurs around $z = 50$, while the double-charge vortex has been propagated to $z = 1000$ with no sign of instability.

To further our theoretical understanding, we recall the discrete model. In the latter the analytically tractable anti-continuum limit can be used, for which discrete vortex solutions can be explicitly constructed and a detailed stability analysis can be performed, as has been done for square lattices [12]. In such a setting we consider the six site configuration with topological charge m over the contour, which takes the form $u_j = \exp(in\phi_j)\exp(i\beta z)$, where $\phi_j = 2\pi jm/6$ and $j = 1, \ldots, 6$ for the

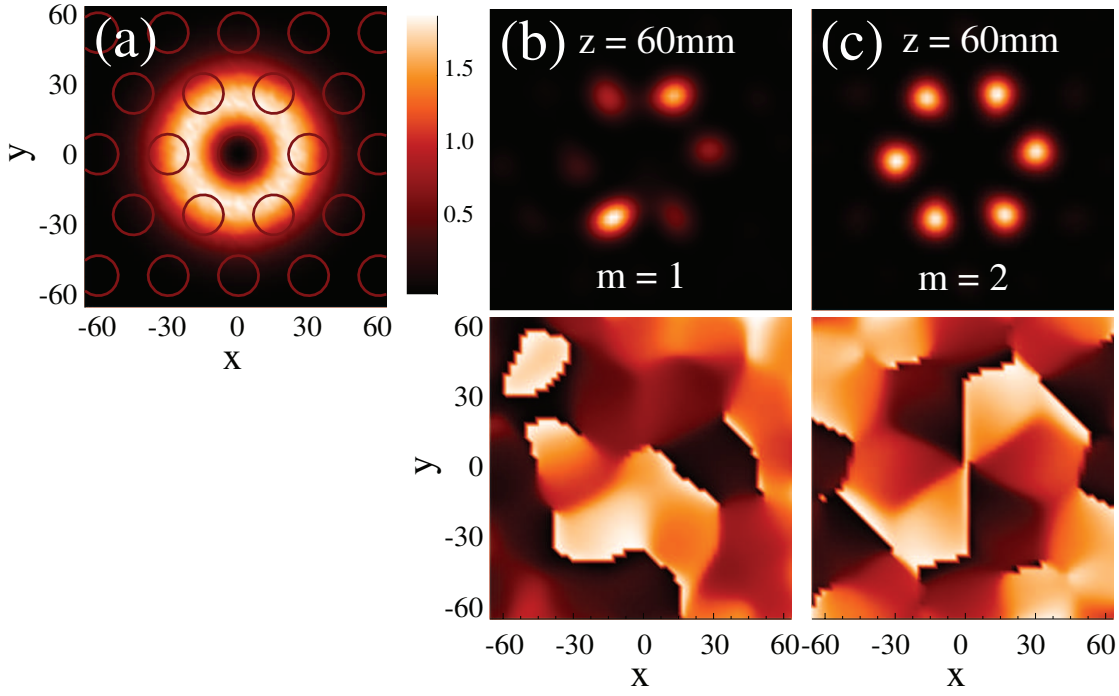

Figure 60. (a) Input beam intensity profile relative to the lattice (position of lattice intensity maxima are shown as rings). The intensity is given by the color-bar on the immediate right. Appearance of the beam at $z = 60$mm with different initial vortex phases (intensity not to scale of color-bar); (b) single-charge vortex, (c) double-charge vortex. Top panels: intensities; bottom panels: phase.

six sites constituting the relevant contour. It is straightforward to see that this configuration yields non-trivial phase profiles for $m = 1$ and $m = 2$. For these structures, according to the framework of [12], the fundamental vortex will be *unstable* due to two double real eigenvalue pairs and a single real eigenvalue pair whereas the $m = 2$ configuration may be *stable*. These general results may also be physically understood as a consequence of the 1D modulational instability (MI) results [68] along the 1D (with periodic boundary conditions) six-site contour of the vortex. Such MI considerations predict that configurations where adjacent sites have less than a $\pi/2$ phase difference (i.e. a single-charge vortex) will be unstable,

while those with more than a $\pi/2$ phase difference (the double-charge case) will be stable. Again, extending our consideration of the 1D six-site contour to the case of a defocusing nonlinearity, one can apply a so-called *staggering* transformation *along the contour*, $U_j = u_j(-1)^j$. Substitution of this expression in the discrete equation transforms the model from defocusing to focusing (and vice versa), as also discussed earlier for general square lattices. This amounts to translating the phase of every other node along the contour by π and, hence, transforming an $m = 1(m = 2)$ focusing vortex to an $m = 2(m = 1)$ defocusing vortex respectively, confirming again the stability observed in Section 4.1.4.

4.2.3 Experimental proposal

Finally, we consider the generation of double-charge vortices and suggest parameters for their experimental observation. For our particular lattice parameters we find that generation of stable double-charge vortices is possible over a wide range of input beam intensities and profiles, at least within our isotropic medium approximation. We consider a Laguerre-Gaussian input beam with the profile shown in Figure 60, kept as constant as possible as the input phase is changed, with maximum intensity $\sim 1.8I_b$. In the subsequent evolution we see break up of the beam into single-site discrete solitons if the initial phase corresponds to a single-charge vortex (Figure 60(b)), while with an initial double-charge vortex phase we see stable generation of the discrete double-charge vortex (Figure 60(c)). Output at $z = 60$mm is shown, however we have seen no sign of instability in the generated double-charge vortex at a distance of $z = 500$mm.

Based on the above considerations, we believe that inputs of the type associated with $m = 2$ should be sustained during propagation not only by hexagonal crystals in photorefractive media, but also by two-dimensional hexagonal waveguide arrays

(e.g., in glass), showcased in recent experiments [31]. Importantly also, similar results are theoretically expected and have been numerically confirmed (results in Chapter 3) to be valid in the case of honeycomb lattices in such media.

The next section will describe the investigation in a real experiment in hexagonal and honeycomb optical lattices in photorefractive crystals.

4.3 Experimental results, anisotropy, and lattice stretching

The main objective of this section is to demonstrate experimentally the numerical and theoretical results from previous sections about the stability of a double-charge vortex in contrast to the corresponding single-charge vortex state which is unstable under the same conditions. We extend the earlier theoretical work for isotropic systems and study the full anisotropic model of nonlinear media with the numerical results supporting our experimental observations [1]. To provide an additional theoretical insight on this stabilization effect, we employ a simpler discrete model to examine the effect of the lattice stretching on the vortex stability, and also showcase the inversion of the vortex stability picture (between single- and double-charge vortices) in the case of the defocusing nonlinear response.

4.3.1 Experimental results

First, we demonstrate experimentally the stable generation of a double-charge vortex in a photorefractive crystal in the presence of a hexagonal photonic lattice in the self-focusing regime, as predicted theoretically for an isotropic model in Chapter 3. The experimental setup is shown schematically in Figure 61, and it is similar

[1]The experiments in this section have been performed by the experimental group of Cornelia Denz at the Institut für Angewandte Physik and Center for Nonlinear Science (CeNoS), at Westfälische Wilhelms-Universität in Münster, Germany.

to that used earlier in [69]. A beam from a frequency-doubled Nd:YAG laser at a wavelength of 532 nm is split into two beams with a beam splitter, and the separate beams are used to illuminate two programmable spatial light modulators.

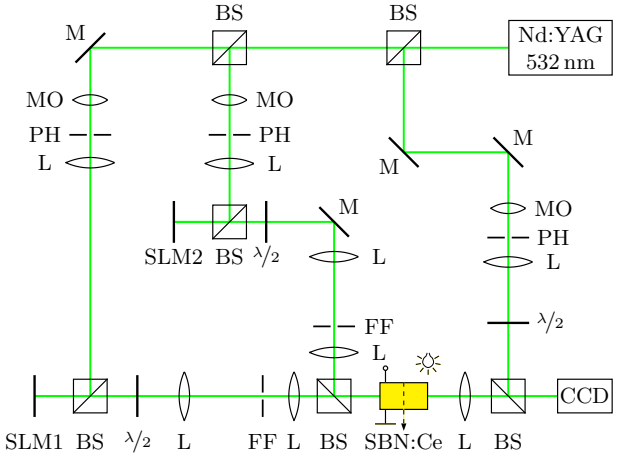

Figure 61. Schematic of the experimental setup. BS, beam splitter; CCD, camera; FF, Fourier filter; L, lens; M, mirror; MO, microscope objective; PH: pinhole; SLM, spatial light modulator.

The first spatial light modulator (SLM1, see Figure 61) converts the incoming beam into three interfering plane waves which are imaged onto the front face of a 20 mm long photorefractive $Sr_{0.60}Ba_{0.40}Nb_2O_6$ (SBN:Ce) crystal which is externally biased with a DC electric field directed along its optical *c*-axis. The resulting interference pattern is that of a two-dimensional hexagonal photonic lattice (Figure 62) with a lattice intensity of $I_{latt} \approx 75$mW. A half wave plate ensures the polarization of the lattice beam to be ordinary, so during the beam propagation through the crystal the nonlinear effects are negligible [13]. The lattice structure is oriented such that the light intensity maxima are aligned along the lines parallel to the optical axis of the crystal in the so called 'horizontal configuration'. The periodic light intensity distribution induces a corresponding refractive index pattern via the photorefractive effect [13] forming the optical lattice. Due to the anisotropic nature

of the nonlinear response of the crystal this optically induced refractive index does not preserve the symmetry of the lattice beam. In particular, the modulation of the refractive index is stronger along the optical axis than along the diagonals making the resulting optical coupling between refractive index maxima very asymmetric (see Figure 62, top row). To counteract the effect of the anisotropy, the lattice forming beams are tilted to induce a stretching of the lattice along the vertical direction such that the optical coupling between lattice maxima is closer to that of the original hexagonal symmetry of the lattice [70] yielding lattice constants of d_y= 62μm and d_x=27μm for the vertical and horizontal directions, respectively. This gives a ratio of $d_y/d_x \approx 2.2$ as opposed to the ratio $d_y/d_x = \sqrt{3}$ of a symmetric lattice. The importance of the lattice stretching for the vortex stability is examined theoretically below in Section 4.3.2.

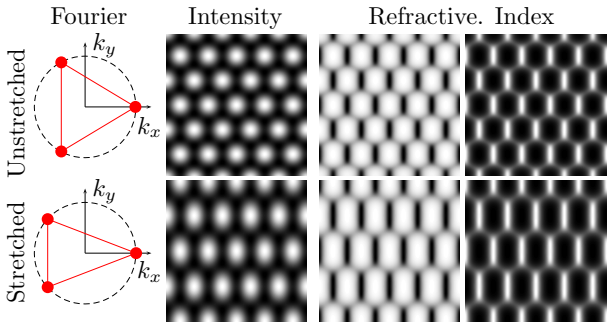

Figure 62. Sketch of the Fourier image and numerically calculated lattice intensity and refractive index profiles for the symmetric hexagonal lattice (top panels) and the stretched lattice (bottom panels). The lattice beams in Fourier space are indicated by red dots forming an equilateral triangle for the unstretched lattice and an isosceles triangle for the stretched lattice. The refractive index profiles are shown for focusing (left) and defocusing (right) nonlinearities.

The second spatial light modulator (SLM2, see Figure 61) combined with proper Fourier filtering [71, 72] is employed to achieve the desired amplitude and phase

structure of an incident Gaussian probe beam. The polarization of the probe beam is extraordinary, so it propagates through the crystal in the nonlinear regime. The strength of nonlinearity is controlled by varying an applied external dc electric field. In all our experiments the value of the bias potential was set to be approximately 2.2 kV/cm. In order to visualize the phase structure of the probe beam, a third beam is derived from the laser. It is passed through a half wave plate to ensure its extraordinary polarization and subsequently sent directly to the CCD camera to record a phase interferogram with the probe beam.

We use the phase modulator to impose either a 2π or 4π phase winding on an input modulated (six-site) beam for the generation of single- and double-charge vortices, respectively. The characteristics of the beams are otherwise identical, and thus any differences in the dynamics are due solely to the different input phases. We selectively vary the input beam intensity to effectively move from the linear regime (low power, $I_{probe} \approx 50$nW) to the nonlinear regime (high power, $I_{probe} \approx 550$nW).

The single-charge vortex input is shown in Figure 63(a). Its intensity distribution has a form of a necklace with six intensity peaks whose positions correspond to the lattice sites (index maxima). At low input power the beam undergoes discrete diffraction and a complete loss of the initial six site input state [Figure 63(b)]. At high power the initial six site intensity profile changes significantly after propagation [Figure 63(c)], showing strong intensity modulations and even filling in the central lattice site. Furthermore, in the phase profile multiple vortices are seen to appear, further indicating a breakdown of the single-charge state [circles in bottom panel of Figure 63(c)]. We were unable to find an example of stable propagation of the single-charge vortex in the high-power (nonlinear) regime, a result consistent with the isotropic case predictions of [73] (see also the analysis below for the anisotropic case).

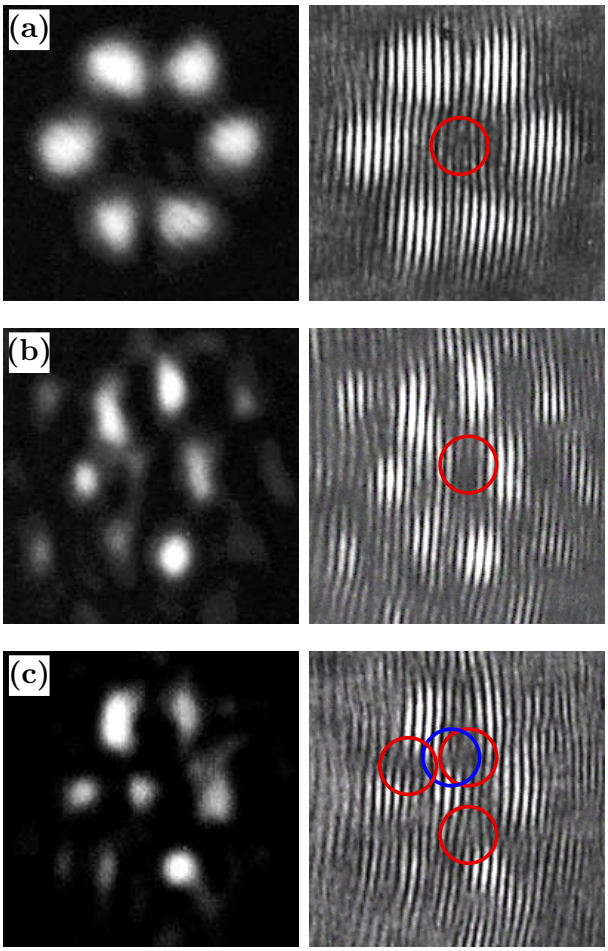

Figure 63. (a) An input single-charge vortex beam; (b) the beam profile and phase at the output crystal face for low input intensity; (c) the same as (b) except output for high input intensity. In both cases we see the break-up of the single-charge vortex. Here and below in experimental figures: left panels show intensity; right panels reveal phase structure; circles indicate positions of vortices with charge $m = +1$ (red) and $m = -1$ (blue).

In the case of the double-charge vortex input [see Figure 64(a)] we again observe a discrete diffraction with low input power [see Figure 64(b)], however the result changes dramatically when the power is increased [see Figure 64(c)]. We observe that now the six-site input structure is preserved in the nonlinear propagation. Interestingly, while the overall phase winding is still 4π, it is seen that the initial

double-charge singularity has split into two single-charge vortices [circles in the lower panel of Figure 64(c)]. This splitting of the higher-order singularity has been shown to be due to an inherent topological instability in the higher phase-winding [74]. This topological breakdown in the linear (low power) part of the field further indicates that the stability of the 4π phase winding across the six sites is due to the interplay of the nonlinearity and local phase of the high-power sites suppressing the development of a dynamical instability [73]. However, we find that this stability is critically dependent on the symmetry of the lattice, with a decrease in the lattice stretching (and thus a corresponding decrease in the symmetry of the underlying modulated refractive index) leading to a dynamical instability in the double-charge state as well. The phase interferogram in Figure 64(c) also indicates an additional pair of single-charge vortices of the opposite charge inside the vortex structure (not marked by circles). However, this additional pair does not affect the stability of the 4π phase winding, and it can be fully attributed to inevitable experimental noise in this region of low intensity of light.

4.3.2 Numerical simulations with anisotropy

In the earlier section examining double-charge vortex stability the isotropic nonlinear model was used [73] which does not take into account anisotropy of the photorefractive nonlinearity and the stretching of the lattice. Therefore, to corroborate our experimental results, here we use the full anisotropic model. The propagation of a scalar probe field A through a photorefractive crystal is given by,

$$2i\frac{\partial A}{\partial z} + \nabla_{\perp}^{2} A - \gamma_{nl} E_{sc}(I_{tot}) A = 0, \tag{4.2}$$

where $\nabla_{\perp}^{2} = \partial^2/\partial x^2 + \partial^2/\partial y^2$; $I_{tot} = |A_{latt}|^2 + |A|^2$, A_{latt} is the periodic lattice wave, and $\gamma_{nl} = k_0^2 w_0^2 n_0^4 r_{eff}$ is the photorefractive nonlinearity coefficient proportional to

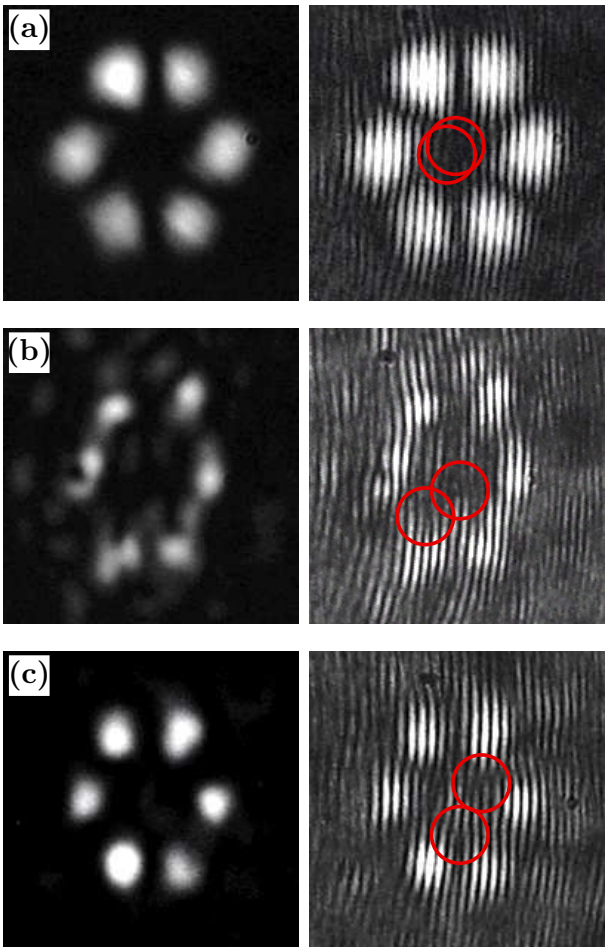

Figure 64. The same as in Figure 63, but for the case when the input beam (a) has a double-charge vortex phase. (b) Output at the crystal face demonstrates discrete diffraction for low power and (c) discrete double-charge vortex generation at high power.

the effective element r_{eff} of the linear electro-optic tensor. The electric screening field E_{sc} is generated by the separation of optically excited charges which drift in the external electric field. This directional drift is responsible for an anisotropy of the total electric field in the crystal and consequently an anisotropic refractive index change. A quantitative model describing the stationary dynamics has been proposed in terms of the scalar potential ϕ from which the screening field may be

found through $E_{sc} = -\partial_x \phi$. The equation describing the evolution of this potential is given by [75],

$$\nabla_\perp^2 \phi + \nabla_\perp \ln(1 + I_{tot}) \nabla_\perp \phi = E_{ext} \partial_x \ln(1 + I_{tot}), \tag{4.3}$$

where E_{ext} is the dc bias voltage applied along the optical axis of the crystal which is taken to be the x-axis. The transverse coordinates (x, y) and propagation coordinate z are measured in units of the characteristic lengths w_0 and z_0 respectively, where $z_0 = k_z w_0^2$ and $k_z = n_0 k_0$ with $k_0 = 2\pi/\lambda$. In particular, we use a transverse scale of $w_0 = 10\mu$m and λ and n_0 as for the experiment. The total intensity I_{tot} is normalized in units of the background illumination and we take $E_{ext} = 2.5$kV/cm. For the lattice wave we use the expression

$$\begin{aligned} A_{latt} &= \exp(2ik_x x/3) + \exp(-ik_x x/3 + ik_y y) \\ &\quad + \exp(-ik_x x/3 - ik_y y), \end{aligned} \tag{4.4}$$

leading to a diffraction-free hexagonal pattern with the horizontal orientational symmetry shown in Figure 62. We consider a stretched lattice with $k_x/k_y = 2.5$ and spatial separations of lattice maxima of $d_x = 2\pi/k_x = 2$ in x and $d_y = 2\pi/k_y = 5$ in y directions (lattice spacings of 20μm and 50μm respectively) [2].

First we consider the case of a six-site initial state with a single-charge vortex phase of the form shown in Figure 65(a) with either low or high power propagating a distance of $z = 20$mm in the lattice. For the low input power case [Figure 65(b)] we see that, as in the experiment, the vortex beam undergoes strong diffraction and break-up. If instead a high input power is considered [Figure 65(c)] the vortex maintains much of its form. Some intensity fluctuations are evident, and more importantly, the vortex phase has deteriorated showing breakdown of the initial

[2]Note there is symmetry here in case $k_x = \sqrt{3} k_y$.

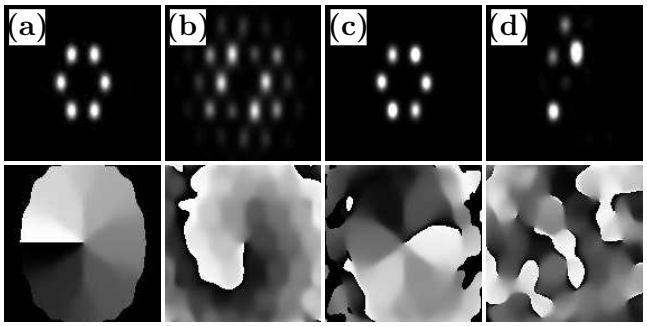

Figure 65. Numerical simulation of a single-charge vortex (E_{ext} = 2.5kV/cm, $I_{latt} = 1$, $\beta = 3$). (a) Initial vortex beam profile; (b) beam profile at $z = 20$mm for low input power; (c) beam profile at $z = 20$mm for high input power; (d) high power output at $z = 280$mm. Top panels: intensity; bottom panels: phase.

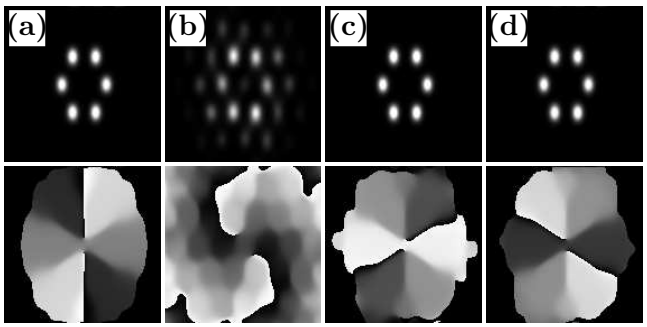

Figure 66. Numerical simulation of a double-charge vortex (E_{ext} = 2.5kV/cm, $I_{latt} = 1$, $\beta = 3$). (a) Initial vortex beam profile; (b) beam profile at $z = 20$mm for low input power; (c) beam profile at $z = 20$mm for high input power; (d) high power output at $z = 280$mm. Top panels: intensity; bottom panels: phase.

single-charge vortex circulation. It must be noted that the break-up is clearly less than that observed in the experiment and this discrepancy is attributed to the higher anisotropy of the experimental lattice leading to a larger instability growth rate. In our numerical simulations, the strong instability becomes evident for longer propagation distances as shown in Figure 65(d) for $z = 280$mm.

In Figure 66 we consider the same input beam intensities but change the phase to that of a double-charge vortex, as shown in Figure 66(a). The low power output in Figure 66(b) appears similar to the single-charge case, exhibiting diffraction and break-up of the vortex. In contrast, the high power output in Figs. 66(c,d) appears unchanged in the intensity profile with a well-pronounced double-charge vortex phase. Similar to the experimental results, the separation of the double-charge phase singularity into two single-charge singularities is observed, however the phase circulation around a contour tracing the six high intensity sites is well defined and equals 4π.

4.3.3 Effect of lattice stretching

A key new feature of the full model considered here, as compared to the isotropic case studied earlier [73], is the presence of anisotropy. In the experiment and in numerical simulations, we have sought to reduce the effects of the anisotropy by stretching the lattice. In this section we use a discrete model to obtain some further insight, based on semi-analytical considerations, on how the lattice stretching (or more generally the symmetries of the inter-site coupling) affects the discrete vortex stability.

Within the framework of the discrete approximation the stretched hexagonal lattice corresponds to a set of coupled ODEs for the complex amplitudes $u_{m,n}$ of the following form:

$$i\frac{du_{m,n}}{dz} = -\varepsilon \sum_{m',n'} C_{m',n'} u_{m',n'} + (4+2C)\varepsilon u_{m,n} - b|u_{m,n}|^2 u_{m,n}, \tag{4.5}$$

where the constant ε denotes the strength of linear coupling between waveguides, $b = 1$ for self-focusing and $b = -1$ for self-defocusing media. The set $\{m', n'\}$

indexes the six nearest neighboring sites to the site (m, n), a pair in each of the three principal directions. The parameters $C_{m',n'}$ account for the coupling anisotropy and are equal C for the neighbors lying along the $(1, 0)$ direction and 1 otherwise.

In the anticontinuum limit $\varepsilon \to 0$, i.e. for very weak interaction between neighboring waveguides, the solutions of Eq. (4.5) can easily be found in the general form $u_{m,n} = \sqrt{\beta} \exp\{-i\beta z + i\theta_{m,n}\}$ for arbitrary $\theta_{m,n} \in [0, 2\pi)$ [12]. Letting $\beta = 1$ without loss of generality and using j to index the sites along the six-site one-dimensional contour shown in Figure 67(a), the condition for existence of solutions with $\varepsilon > 0$ reduces to the vanishing of the total power flow at each site

$$c_{j,j-1} \sin(\theta_j - \theta_{j-1}) + c_{j,j+1} \sin(\theta_j - \theta_{j+1}) = 0, \tag{4.6}$$

subject to periodic boundary conditions $\theta_{j+6} = \theta_j$ for $j = 1, \ldots, 6$ [12]. Similar to $C_{m',n'}$ above the constants $c_{j,k}$ account for the coupling anisotropy,

$$c_{j,k} = \begin{cases} C, & (j,k) \in \{(2,3),(3,2),(5,6),(6,5)\}, \\ 1, & \text{otherwise.} \end{cases} \tag{4.7}$$

We consider first the focusing medium with $b = 1$. In the case $C = 1$, the single and double-charge vortex solitons exist close to the anticontinuum limit as defined by the phase vectors $\theta_j = Sj\pi/3$, where $S = 1, 2$, respectively. An analytical approximation for the stability of the discrete solitons can be made for small ε based on an appropriate modification of the theory originally developed in [12] for the isotropic square lattice. The stability can be determined from the eigenvalues γ_j of the 6×6 Jacobian of Eq.(4.6),

$$(\mathcal{M})_{j,k} = \begin{cases} b[c_{j,j+1}\cos(\theta_{j+1} - \theta_j) + \\ c_{j,j-1}\cos(\theta_{j-1} - \theta_j)], & j = k, \\ -b[c_{j,k}\cos(\theta_j - \theta_k)], & j = k \pm 1, \\ 0, & |k - j| \geq 2. \end{cases} \tag{4.8}$$

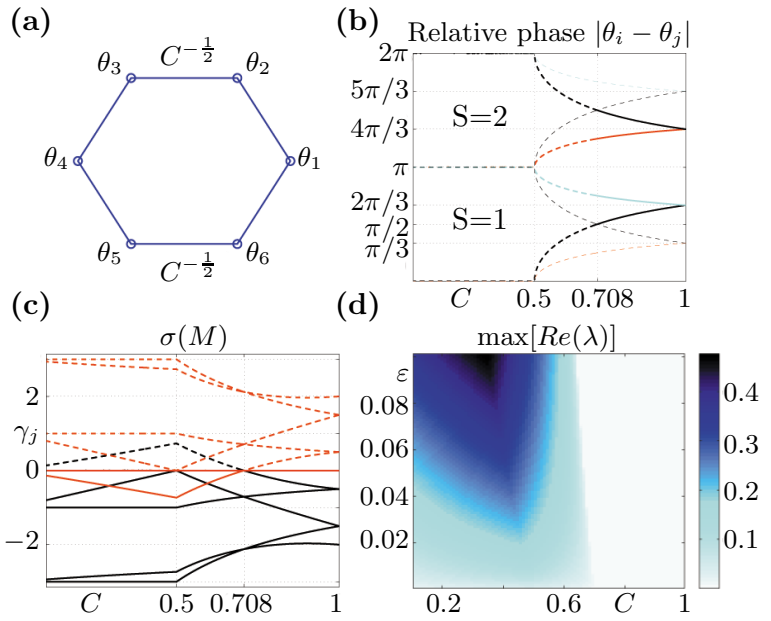

Figure 67. The hexagonal cell is approximated by a contour shown in (a). The image in (b) shows the relative phases for the single- (thin lines) and double- (thick lines) charge vortices distinguishing stable (solid lines) and unstable (dashed lines) solutions. For $C = 1$ the phases are equidistant and all are a distance $\pi/3$ or $2\pi/3$ from one another. These are the isotropic single and double-charge vortices. For smaller C, the phases of θ_2 and θ_3 become closer for the double-charge (thick black) solution (and further for the single-charge, thin black), and when $|\theta_2 - \theta_3| < (>)\pi/2$, for $C < C_{\rm cr} = 0.708$, one corresponding eigendirection becomes unstable (stable). This can be observed in (c), in which the 6 eigenvalues of the linearization matrix $\mathcal{M}$ are presented as a function of C. When they are all negative the solution is stable close to the anticontinuum limit. Notice the smallest magnitude black one becomes positive for $C < C_{\rm cr}$, leading to instability. (d) The bifurcation of the relevant eigenvalue of the $S = 2$ vortex through the origin is represented by the maximum real part of the linearization spectrum, $\max[\mathrm{Re}\,\lambda]$ as a function of both the anisotropy parameter, C, as well as the coupling ε. Notice the critical point (in C) shifts only very slightly from the first order prediction for the wide range of parameter values $0 < \varepsilon < 0.1$.

For each eigenvalue γ_j, the full linearization around a stationary solution will have eigenvalue pairs λ_j given, to leading order, by $\lambda_j = \pm\sqrt{2\gamma_j\varepsilon}$. Therefore, the sign of the eigenvalues of $\mathcal{M}$ determines whether the eigenvalues of the bifurcating solution will be real or imaginary. In particular, positive eigenvalues of $\mathcal{M}$ will indicate real eigenvalues of the full linearization problem, and, hence, instability for this Hamiltonian system.

The results for the existence and stability of single and double-charge vortex configurations are presented in Figure 67(b,c) for $C \in [0.1, 1]$. The results for $1 < C < 10$ are not shown since no new instabilities arise in that setting. These results can be summarized as follows:

- The $S = 2$ vortex is stable for $C > C_{\rm cr} = 0.708$, as it is in the isotropic case presented in section 4.1.4.

- As two of the relative phase pairs decrease below $\pi/2$ due to the stretching, the $S = 2$ vortex becomes destabilized for $C < C_{\rm cr} = 0.708$, due to an effective modulational instability 4.1.4 (see also [76] for a general analysis of the instability) along the one-dimensional six-site contour.

- Below a stretching of $C = 0.5$, the $S = 2$ configuration becomes real [its profile is shown in Figure 67(b)] and bears four sites with phase of π, and two with a phase of 0 (or vice versa).

- On the other hand, the vortex with $S = 1$ is unstable throughout the considered interval of stretching parameter, but also degenerates into a real solution with 3 adjacent sites of 0 phase, while the remaining adjacent 3 sites have a phase of π.

A continuation of solutions for the double-charge family was performed in the

coupling parameter ε and the critical value $C_{\rm cr}$, represented by the front of real eigenvalues, was found to deviate very weakly from the first order prediction, when ε was varied in the interval $[0, 0.1]$. The stability results are detailed in Figure 67(c-d).

We can use the full anisotropic model (4.2), (4.3) to estimate the relative coupling values typically used in experiments. In the unstretched case we calculate the anisotropy parameter to be $C \approx 0.22$, while with the lattice stretching this becomes $C \approx 0.82$. These values have been calculated for the particular case of the high input beam intensity although they depend strongly on both the lattice depth and the beam intensity. It is evident however that the unstretched value places the lattice in a regime where no stable vortex formation is expected from the discrete model analysis, in agreement with experiment. Furthermore, in the stretched case we can see that again in accordance with the analysis of the discrete model a stretching parameter of $C = 0.82$ is within the stable region of double-charge vortex formation, as was also confirmed experimentally. We thus illustrate a very good agreement between the predictions of the discrete model, the parameters calculated from the full anisotropic model, and the actual experimental results.

One of the advantages of the discrete model is that the relevant theoretical analysis can be straightforwardly extended to the case of the defocusing nonlinearity. In particular, it is well-known that a so-called *staggering transformation* along the contour of such a solution for a given b, i.e. $\tilde{U}_j = (-1)^j U_j$, yields a solution to the problem with $\tilde{b} = -b$; this illustrates that a mere staggering transformation suffices to extend the focusing results above to the defocusing case. More specifically, the staggering transformation of the $S = 1$ focusing solution leads to the $S = -2$ (or equivalently $S = 2$) solution for the defocusing case, while that of the $S = 2$ focusing vortex leads to the $S = -1$ (or equivalently $S = 1$) defocusing vortex.

Importantly also, the stability results for single and double-charge solutions for the focusing case immediately translate to their defocusing counterparts, namely the double and single-charge solutions (respectively). Since the stability predictions are exactly reversed in the defocusing case (between the single- and double-charged vortex), numerical and experimental studies have also been performed in this setting to test the theoretical prediction.

4.3.4 Defocusing nonlinearity

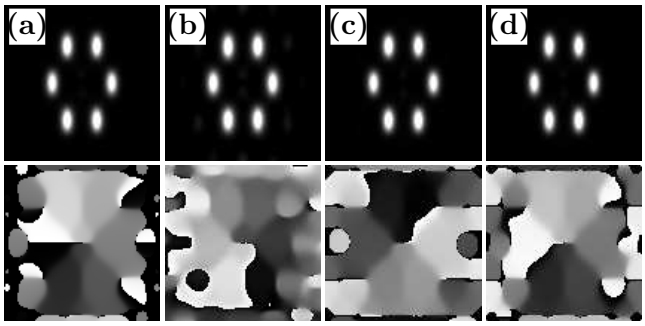

Figure 68. Numerical simulation of a single-charge vortex for defocusing nonlinearity ($E_{ext} = -2.5$kV/cm, $I_{latt} = 4$, $\beta = 2$). (a) Initial vortex beam profile; (b) beam profile at $z = 20$mm for low input power; (c) beam profile at $z = 20$mm for high input power; (d) high power output at $z = 280$mm. Top panels: intensity; bottom panels: phase.

As discussed above, the stability properties of single- and double-charge vortices with focusing nonlinearity are expected to be inverted when the nonlinearity is changed from focusing to defocusing. For completeness of our analysis, we examine this situation numerically as well as experimentally and confirm this general theoretical prediction.

Similar to the focusing case, we perform numerical simulations using the full anisotropic model (4.2), (4.3) but reverse the sign of the nonlinearity by using

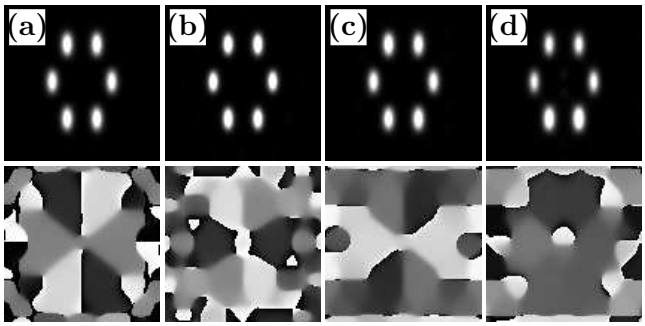

Figure 69. Numerical simulation of a double-charge vortex for defocusing nonlinearity ($E_{ext} = -2.5$kV/cm, $I_{latt} = 4$, $\beta = 2$). (a) Initial vortex beam profile; (b) beam profile at $z = 20$mm for low input power; (c) beam profile at $z = 20$mm for high input power; (d) high power output at $z = 280$mm. Top panels: intensity; bottom panels: phase.

$E_{ext} = -2.5$kV/cm.

Figure 68 summarizes the results for the single-charge vortex and it clearly demonstrates the inverted stability properties caused by the defocusing nonlinearity. In contrast to the focusing case (Figure 65), intensity and phase profile of the input structure are preserved and a stable single-charge discrete vortex soliton is formed. It should be noted however, that in the low intensity regime (Figure 68) the diffraction is much less pronounced than in the presence of a focusing nonlinearity and hardly visible for propagation distances of 20 mm (Figure 68). The same result is obtained for the low intensity double-charge vortex shown in Figure 69(b). Moreover, compared to the focusing case, the instability is weaker and more evident in the phase than in the intensity [Figs. 69(c), (d)]. Overall, however, the numerical simulations well confirm the theoretical prediction of inverted stability properties in the defocusing case resulting in a stable single-charge vortex soliton and an unstable double-charge vortex.

Experimentally, the nonlinearity can also be made defocusing by simply invert-

ing the external bias voltage. We consider a bias voltage of ~ 1.6kV/cm antiparallel to the optical axis. Our photonic lattice beam is 50μW; we produce a stretched lattice with the same lattice constants as in the self-focusing case. Notice that now the lattice acquires a honeycomb structure, i.e., light intensity maxima of the lattice forming beams lead to minima of the corresponding refractive index pattern; see bottom panels in Figure 62. It is important to note here that as the theoretical stability results of the discrete model are obtained from the consideration of the one-dimensional six-site contour with periodic boundary conditions, these results are unaffected by the honeycomb structure of the defocusing photorefractive crystal lattice. For each vortex input we consider two different input beam powers, low power ($I_{probe} \approx 30$nW) and high power ($I_{probe} \approx 160$nW). Output intensity and phase are then recorded on the beam exit of the crystal.

First, we consider the single-charge vortex input shown in Figure 70(a). In a good agreement with our numerical simulations, we see only very weak diffraction in the low power (linear) regime [see Figure 70(b)]. More importantly, the single-charge vortex phase breaks up, and we observe the emergence of other vortices indicating that the input beam profile is not stable at low powers. In contrast, at high powers we find that both the intensity and phase profile are well preserved [see Figure 70(c)], in stark contrast to the observations in the self-focusing nonlinearity case.

In the case of a double-charge vortex input [see Figure 71(a)], we observe a diffraction pattern similar to that in the single-charge case at low input powers [Figure 71(b)]. At high input powers, the output shows some diffraction but, more importantly, the vortex phase is again no longer preserved as we are able to identify only a single vortex singularity. This is again in stark contrast to the self-focusing case.

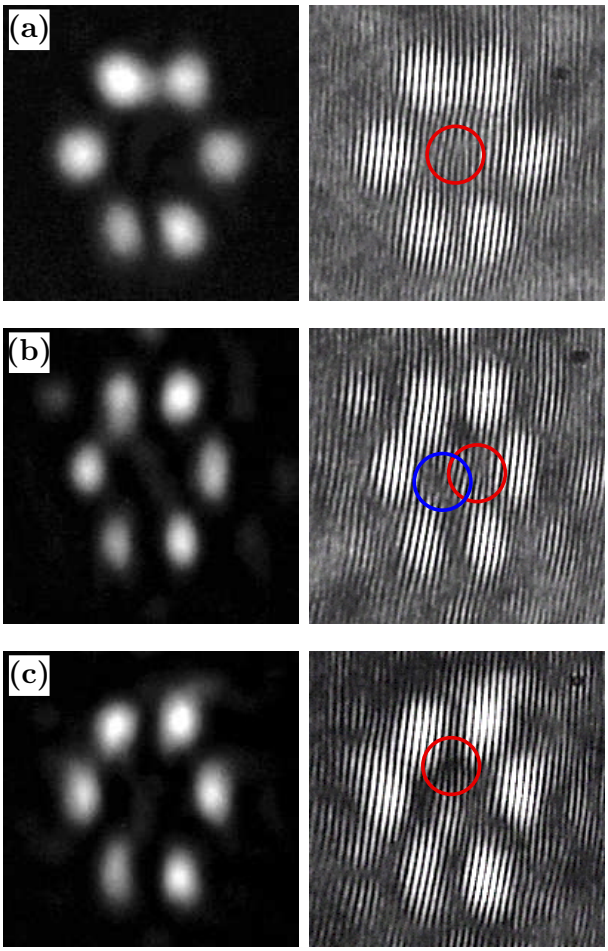

Figure 70. (a) An input single-charge vortex beam in the defocusing regime; (b) the beam profile and phase at the output crystal face for low input intensity; (c) output for high input intensity showing generation of a stable single-charge vortex.

We would like to stress again here that while the stability of the single- and double-charge vortices has been swapped in the defocusing case, with the former now stable, the appearance of the instability is somewhat different between the self-focusing and self-defocusing cases. In the former case, we observed strong intensity modulations which made it clear that the single-charge vortex is unstable. In the defocusing case, the instability development appears to be weaker and to be more

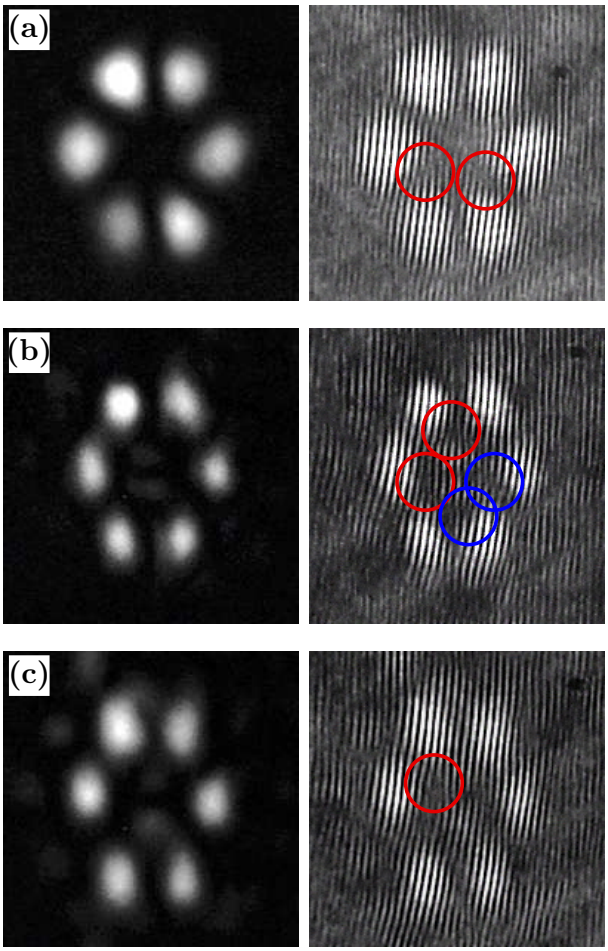

Figure 71. (a) An input double-charge vortex beam in the defocusing regime; (b) the beam profile and phase at the output crystal face for low input intensity; (c) output for high input intensity showing instability of the double-charge vortex.

evident in the phase than in the intensity. However, we can conclude that the stability properties of the vortices in the defocusing case are inverse to those in the focusing case, as illustrated theoretically above (see also [73]).

CHAPTER 5

KAGOMÉ LATTICE

In this Chapter we will focus on the so-called *Kagomé* lattice, which is encountered often in nature and has a very rich structure. In the solid-state community and other areas of physics and science these lattices and many others have been explored for decades [77], but are becoming more prevalent recently [78, 79]. Furthermore, low temperature properties of atomic quantum (ultracold Bose and Fermi) gases have been studied in the trimerized Kagomé lattice [77].

Motivated by recent advances in optically-induced lattices in SBN, we will explore a Nonlinear Schrödinger (NLS) model in both its discrete (DNLS) manifestation as a set of difference equations adhering to the symmetry of the lattice and modeling coupled oscillators, and in the analogous continuum setting using a partial differential equation with an external potential having the appropriate symmetry. In particular, since the continuum model is motivated by experiments with SBN, the nonlinearity will be *saturable* [28, 29]. We will investigate prototypical contours (or paths) of localized structures in this lattice, consisting of six sites as well as four sites, and being both real, and complex valued with continuous phase (modulo 2π).

In this section we consider strictly defocusing interactions. Our main findings in what follows are that

- Certain structures are stable, such as the in-phase gap hexapole and single-charge six-site gap vortex on the honeycomb cell, and the in-phase/out-of-phase quadrupole on the "hourglass cell" (see Figure 72). Other configurations are unstable, such as out-of-phase hexapoles, vortices, etc.

- In the continuum model, continuations of solutions in the first band-gap pass through the second band as quasi-localized structures and then become fully extended in the second band-gap. However, discontinuous extensions, i.e. new continuations of the localized structures, are found to exist in the second band-gap simultaneously with the extended states.

- The result of the evolution of the dynamical instability in these lattices is more complex than in the square lattice case, and may involve not only degeneration to single-site solitons but possibly to multi-site solitary wave structures, and, in the discrete case, often the formation of robust breathing states, consisting of multiple sites (possibly even as many as in the original configuration). In fact, we have found some clear breather formations recurring in multiple simulations:

  - Two nearest-neighbor or opposite sites in-phase with each other and with oscillating amplitudes of comparable magnitude.

  - Two next-nearest-neighbor sites out-of-phase with each other and with oscillating amplitudes of comparable magnitude.

  - Two nearest-neighbor sites having different amplitudes and oscillating between the same phases and opposite phases depending on whether the amplitudes are further from or closer to each other, respectively.

  And, in the continuum version, either all or most of the initially populated

wells remain populated for long propagation distances, with the instability manifesting itself only as phase reshaping (something seen also in the previous chapter for hexagonal and honeycomb symmetries with a defocusing nonlinearity.).

5.1 Setup

To translate our general considerations from Chapter 1 into the setting of a Kagomé lattice, we take G in the definition of $\mathcal{L}_\varepsilon$ to be one of a site dependent subset of two of the principal lattice vectors $\mathbf{a}_1 = (1, \sqrt{3})/2$, $\mathbf{a}_2 = (-1, \sqrt{3})/2$, or $\mathbf{a}_3 = (1, 0)$ (in both positive and negative directions) of the discrete Kagomé lattice presented in Figure 72.

The simulations for the static results in the discrete model were performed in the domain $D_h \backslash K$, where $D_h = [1, \ldots, 33] \times [1, \ldots, 33]$ is the discrete lattice domain corresponding to a triangular lattice and $K = \{(2m + 1, 2n + 1) | (m, n) \in [0, 16]^2\}$. For dynamical evolution, the solutions were buffered with 40 (or more) nodes on all sides to prevent radiation scattering from the boundaries.

Now we take the intensity of the lattice in Eq. (5.1) to be of the slightly modified form

$$I(\mathbf{x}) = I_0 \left| f_1(\mathbf{x}) e^{ik\mathbf{b}_1 \cdot \mathbf{x}} + e^{ik\mathbf{b}_2 \cdot \mathbf{x}} + e^{ik\mathbf{b}_3 \cdot \mathbf{x}} \right|^2, \tag{5.1}$$

where the optical lattice intensity function formed by three (p=0) or four laser beams with $f_1(\mathbf{x}) = e^{ikpx/(1+4p/3)} \cos[pkx/(1 + 4p/3)]$, $\mathbf{b}_1 = (1/(1 + 4p/3), 0)$, $\mathbf{b}_2 = (-\frac{1}{2(1+4p/3)}, -\frac{\sqrt{3}}{2})$, $\mathbf{b}_3 = (-\frac{1}{2(1+4p/3)}, \frac{\sqrt{3}}{2})$. It is presented in this form to highlight that it exists as a continuous transformation of the honeycomb lattice ($p = 0$). Then

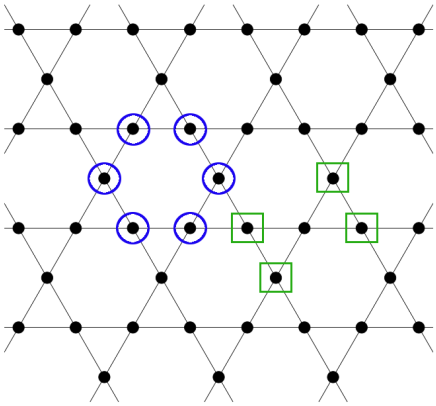

Figure 72. The discrete Kagomé lattice structure is presented above. The six-site contour is given by the blue circles, while the four-site "hourglass" contour is given by the green squares.

as $p \to 3/2$ the lattice transforms from the well-known honeycomb interference pattern into the richer Kagomé lattice. The latter lattice features both the hexagons from the honeycomb lattice and the equilateral triangles from the triangular one, and each node has four neighbors similar to the square lattice. We choose the lattice intensity $I_0 = 1$, and (d, E_0, λ, n_e)=(90,8,532,2.35), consistent with a typical experimentally accessible situation [37]. These parameters remain fixed for our investigation of the continuum problem. A plot of the potential intensity field created by the optical lattice is shown in Figure 73 to illustrate the locations where our localized configurations will live. The non-dimensional value $D = 18.01$.

The numerical simulations are performed in a rectangular 120×120 grid corresponding to the domain size $4d \times 8d/\sqrt{3}$ (i.e. four periods of the lattice in each direction), using a rectangular spatial mesh with $\Delta x = 1.5$ and $\Delta y \approx 1.732$. Regarding the typical dynamics of a solution when it is unstable, we simulate the z-dependent evolution using a Runge-Kutta fourth-order scheme with a step size $\Delta z = 0.01$.

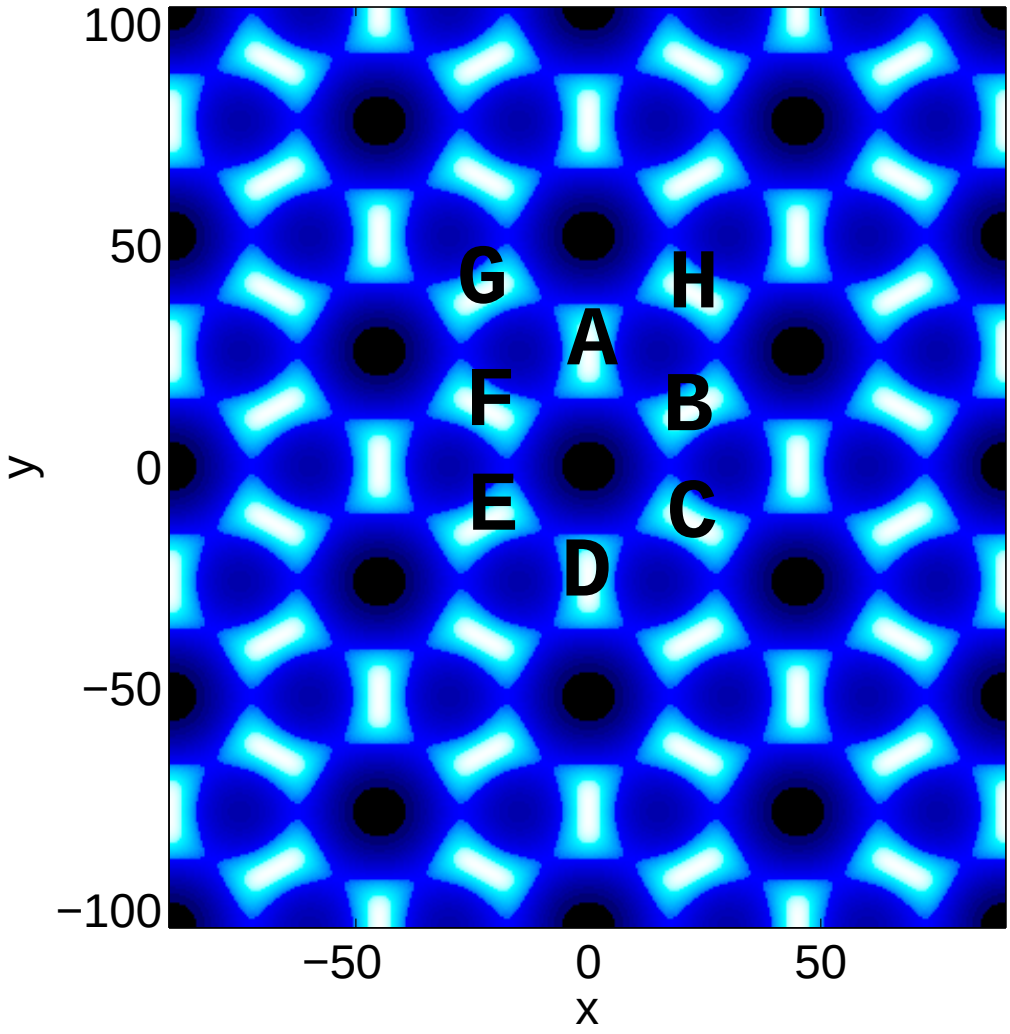

Figure 73. A spatial (x-y) contour plot of the effective potential created by the ordinary polarization standing wave [lattice beam in Eq. (5.1)]. Points A, B, C, D, E, F, G and H define the relevant potential minima for the various configurations we will consider. The contour $\{A, B, C, D, E, F\}$ is the honeycomb cell, which can be considered to tile part of the lattice. The set of sites $\{B, F, G, H\}$ comprise the "hourglass" cell contour we will consider. Together with A, these sites comprise another cell which tiles the remaining part of the lattice.

Continuations in the propagation constant μ can be found with a fixed-point solver and an initial guess of a collection of Gaussian wave-packets in the appropriate configuration. Using a standard eigenvalue solver package implemented through MATLAB, we identified the first two spectral gaps for our given parameters and grid size to be $G_1 \approx (3.545, 4.9454)$ and $G_2 \approx (2.178, 3.515)$. It is worth noting that the bands and gaps remain very close to the same widths for much smaller discretizations (i.e. much larger grids). For instance, with 300 nodes in each direction we have $\tilde{G}_2 = (2.125, 3.463)$, so the change in width of the band-gaps is an order of magnitude closer to convergence than the position (modulo translation). We use the bands appropriate to the discretization in order to compare them with the bifurcation structure of solutions.

The localized states u of the continuum version of (1.6) were obtained using the Newton-Krylov fixed point solver nsoli from [43], which utilizes a GMRES iterative algorithm, based on residual reduction in successive Krylov subspaces, in order to minimize the memory necessary for the linear solver within each step of the Newton algorithm. Some care has to be taken to handle the large size of the representation of a 2D continuum domain. A pseudo-arclength continuation [44] was used to follow each branch and locate the bifurcations which occur at the edges of the bands.

5.2 Numerical results

Now, the extension of theoretical predictions from previous chapters will be matched against systematic numerical simulations. First, for the discrete model, we will perform continuations in the coupling parameter from the AC limit in order to compare the resulting relevant eigenvalues from the linearization spectrum with the corresponding prediction. Next, we will test these results against the contin-

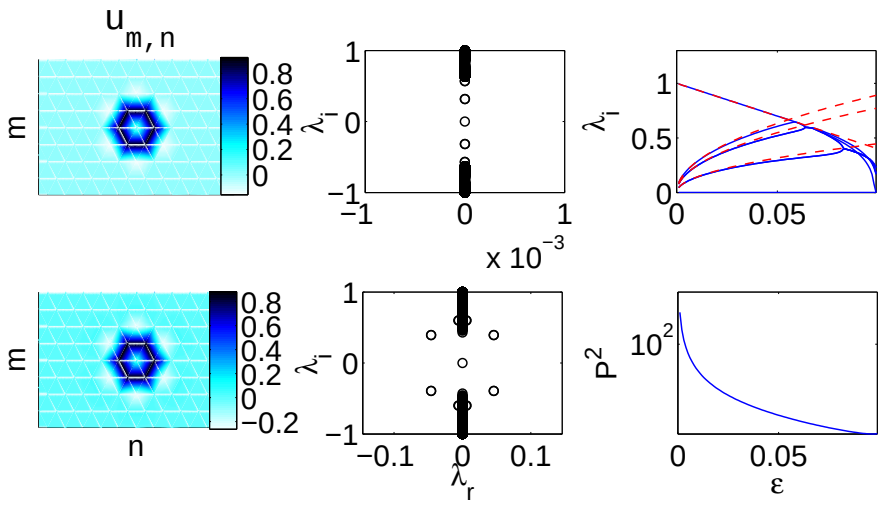

Figure 74. The discrete in-phase hexapole solutions are presented. In the first two columns the profiles (left) and linearization spectra are given before (top, $\varepsilon = 0.061$) and after ($\varepsilon = 0.085$) the first Hamiltonian Hopf (HH) bifurcation. The top right panel depicts the theoretical predictions of the linearization eigenvalues bifurcating from the AC limit (dashed) as well as the actual numerically computed ones (solid). The bottom right panel is P^2 (see Eq. (1.10)), shown on a log scale, where we can observe the decrease in the effective power, as the coupling strength increases.

uum model. The stability results from the discrete case are expected to hold in the sense that there will either be real eigenvalue pairs in the spectrum of the solutions whose discrete analog is unstable close to the AC limit, or else there will be intervals of stability and quartets of eigenvalues due to HH and inverse HH bifurcations. The continuum model reveals not only gap soliton solutions in both the first and the second gaps, but also solitons from where the branch of solutions from the first gap passes through the second band and subsequently becomes extended. Unstable solutions were evolved in time in order to observe their dynamical behavior. Most solutions in the discrete case decompose into breathing configurations with

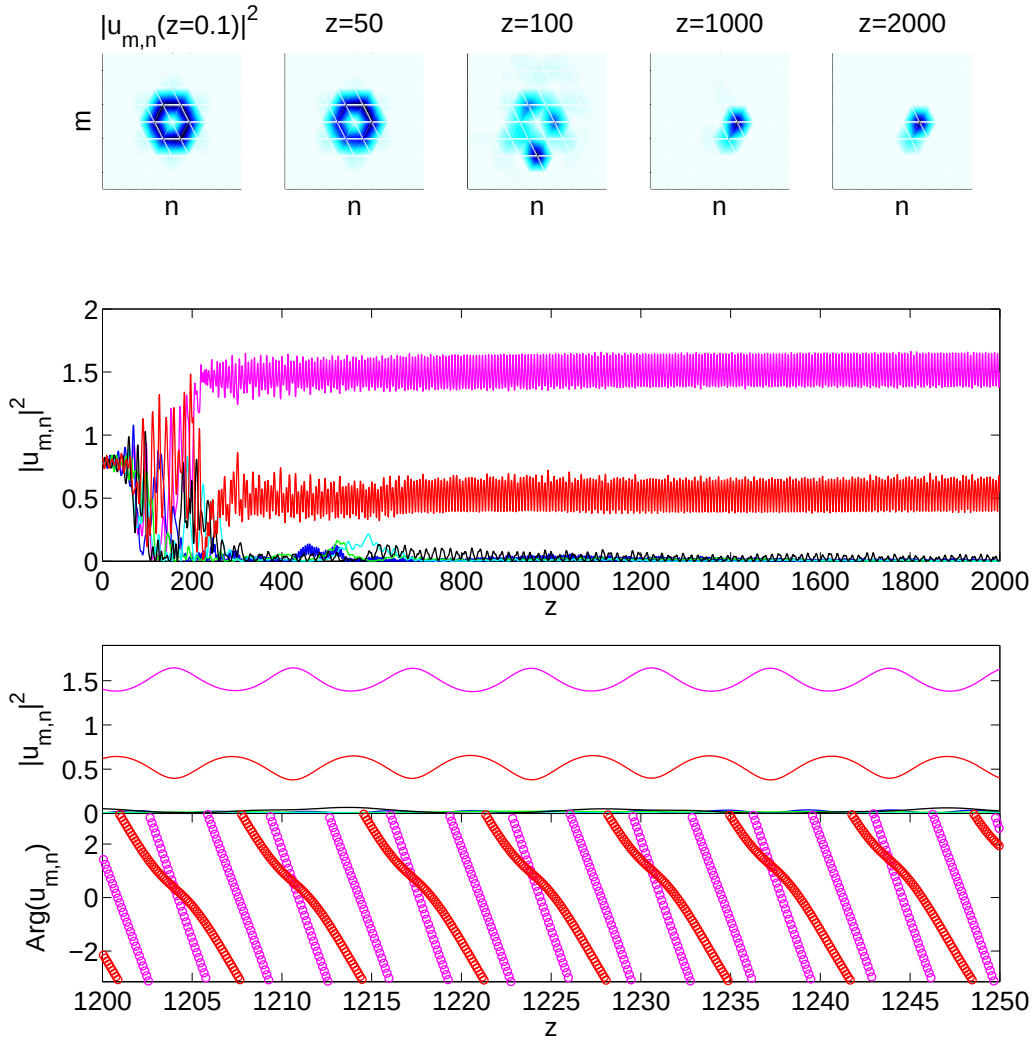

Figure 75. The dynamics of the solution given in the bottom row of Figure 74 is presented. The top row shows snapshots of the modulus for various z, while the next row shows the individual amplitudes at the relevant sites. The structure survives for a while but ultimately disintegrates, due to the instability, into two populated nearest-neighboring sites whose amplitudes breathe closer and further from one another while the phases oscillate between opposite and same, respectively (see the bottom two rows).

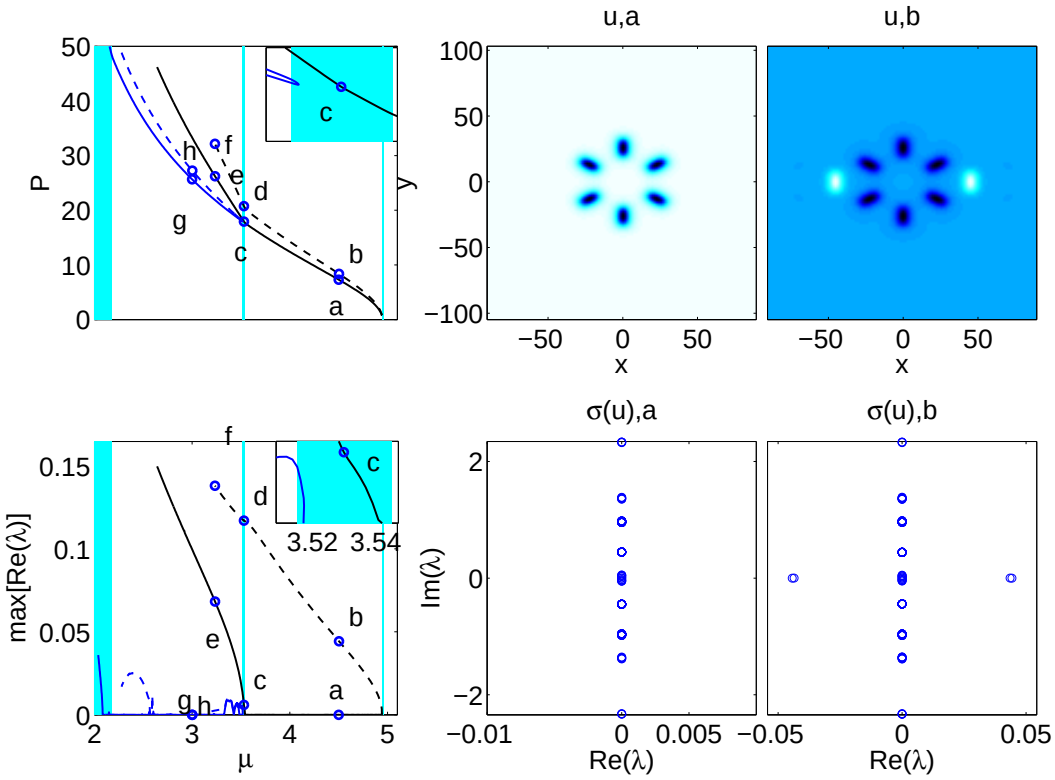

Figure 76. The continuum in-phase hexapole is presented in these panels. The top two left panels show the power, P (top) and instability growth rate (bottom) as given by the maximum real part of the linearization spectrum. The first band is given to the right, beyond which is the semi-infinite gap (it is displayed wider than it actually is for visibility, because its actual width is narrower than a pixel at this scale), the second band is in the middle, and the third band is at the far left. The blue branches in the second gap are actually discontinuous extensions of the localized modes from the first gap, which collide in a saddle-node bifurcation and disappear as can be observed in the inset panels in the upper right corners (this is consistent throughout the following images).The second and third columns of the top set display the principal two solutions a and b, respectively, with full panels of their linearization spectra below them.

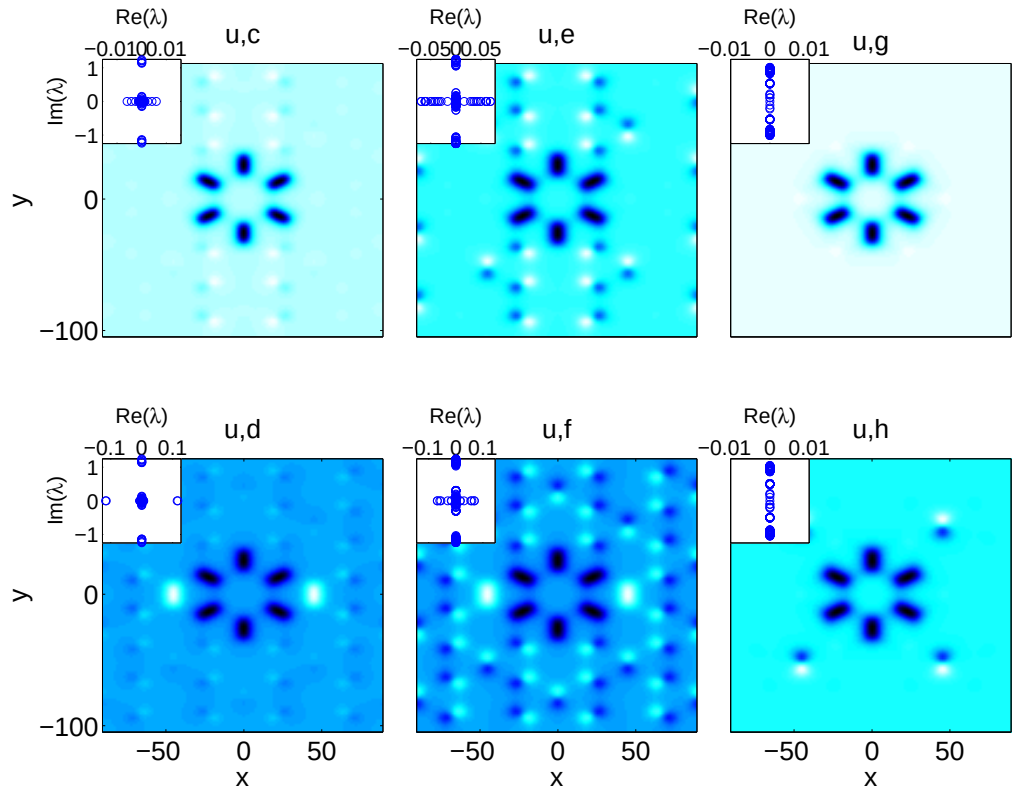

Figure 77. Solutions marked on these plots with the letters c,d,e,f,g and h are presented in the remaining panels with insets of the corresponding spectra embedded in them. There are stable first (a), and also second (g and h) gap soliton structures. The solitons (c,d), with energy in the second band, are unstable.

fewer populated sites and some interesting phase correlations. In the continuum case, most configurations survive for a long propagation distance, with instabilities manifested only as phase reshaping.

This section will be composed of two parts, the first of which will address configurations with six neighbors on the hexagonal cell, the results of which are consistent with recent results in the continuum honeycomb defocusing case [35] and both honeycomb and hexagonal [36] focusing cases (translated with the appro-

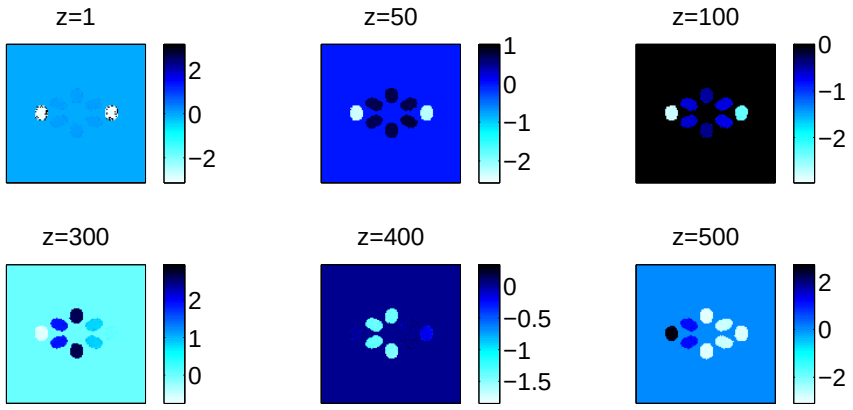

Figure 78. The evolution of the unstable solution given in Figure 76 (b) is shown. The phase is shown as $\arg(u)\chi\{(x,y)||u|^2 > 0.5\max_{(x,y)}(|u|^2)\}$ at various times because the original configuration is preserved for a very long propagation distance (χ is the indicator function which annihilates the field outside of the set on which it is defined). The relative phases of the configuration break up after $z = 100$.

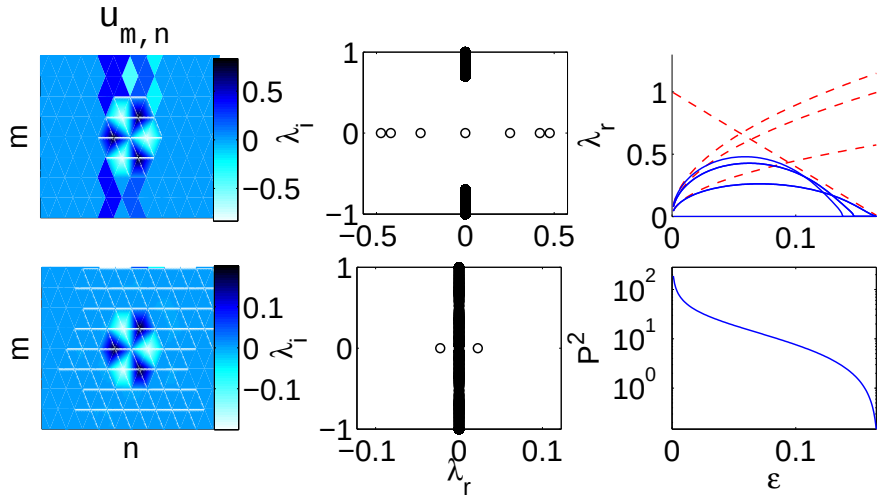

Figure 79. The same panels as Figure 74 except for the unstable out-of-phase hexapole. The top row solution is for $\varepsilon = 0.05$, while the bottom one is for $\varepsilon = 0.16$.

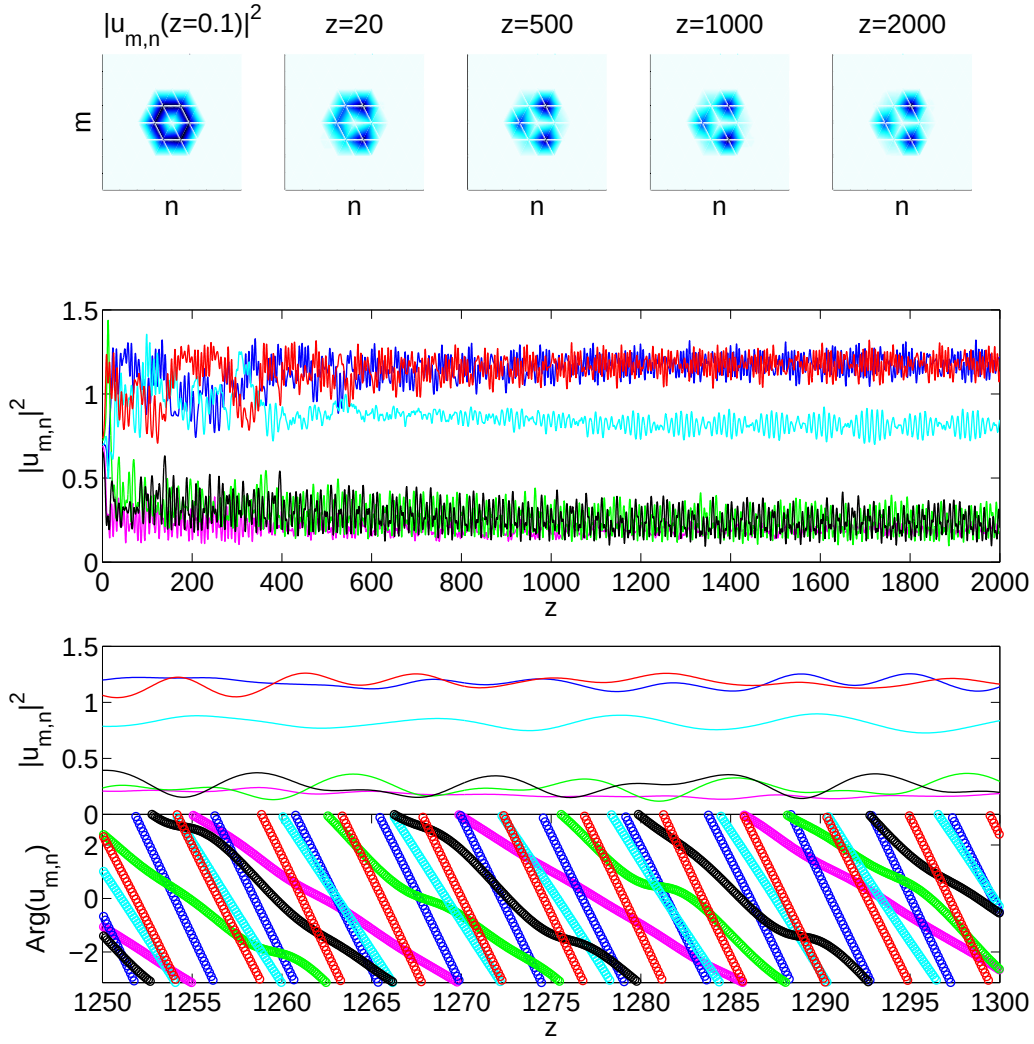

Figure 80. The same as Figure 75 for the out-of-phase solution given in the top row of Figure 79. The original configuration clearly shifts very rapidly, although the different sites remain populated for a long propagation distance. The largest amplitude pair which is separated by one node (i.e. next-nearest neighbors) remains very close to exactly out-of-phase, while the next smallest, which is also next-nearest neighbor to both, passes from the phase of one to the other. The other three sites do not exhibit any phase correlation, although at times two have matching phase and are out-of-phase with the other.

priate staggering transform along the contour). In the second part we will look at quadrupoles along the four corners of the "hourglass" cell which is unique to the Kagomé lattice.

5.2.1 Vortices and hexapoles in the hexagonal cell

The results for the six-site configurations in the hexagonal cell are presented in this section. First we will consider the real-valued configurations of $\Delta\theta = 0$ and $\Delta\theta = \pi$ and then the complex-valued ones where $\Delta\theta = \pi/3$ and $\Delta\theta = 2\pi/3$.

First we will consider the results of the predictions from the previous section for the six-site in-phase configuration (i.e. $\Delta\theta = 0$). This configuration has been predicted to be *stable*. In the discrete model close to the AC limit, Eq. (1.14) predicts, to first order in ε, two double pairs of eigenvalues $i\sqrt{2\varepsilon}, i\sqrt{6\varepsilon}$ and single pairs at $i\sqrt{8\varepsilon}$ and 0. Here we digress slightly to discuss the bound of the phonon band. We consider plane waves of the form $w = e^{i(pn+qm)}$, in each of 2 (of the 3) principal directions, which are used to index the two-dimensional lattice [32], (m, n). Since there are 3 types of nodes in this case, each having neighbors in 2 of the 3 principal directions (that are the same for the hexagoinal lattice), we must consider a linear combination of equal 1/3 weights of the corresponding dispersion relation for each type. This is equivalent to 2/3 of the dispersion relation of the hexagonal lattice, i.e.

$$\mathcal{L}_\varepsilon w = (4 - \frac{4}{3}[\cos(q) + \cos(p) + \cos(p+q)])\varepsilon < 6\varepsilon. \tag{5.2}$$

So, the smallest eigenvalue of the phonon band is given by $i(1 - 6\varepsilon)$, and upon its collision with the eigenvalues which bifurcated from the origin, a cascade of HH bifurcations ensues. The numerical results are presented in Figure 74. The

left column displays two solutions, before (top) and after (bottom), the continuous spectrum intersects with the bifurcation eigenvalues. The middle column has the corresponding linearization spectra. The top right panel depicts the imaginary component of the bifurcation eigenvalues as given numerically (solid line) and by the first order theoretical approximation (dashed line).

The dynamical evolution of the unstable solution from the bottom row is displayed in Figure 75. Eventually the instability manifests itself and the original configuration is destroyed. Two nearest-neighbor sites remain with different amplitudes that oscillate. When they are closer in amplitude they are out-of-phase while when they are further apart, they are in-phase. It is worth noting here that a similar phenomenon was found in the hexagonal as well as the honeycomb lattices with a focusing nonlinearity in [36], except with the relative phases reversed, i.e. the sites were in-phase when closer and out-of-phase when further apart, presumably due to the nature of the nonlinearity (focusing versus the defocusing one here).

Next we investigate the in-phase hexapole in the continuum setting. The solution is stable in the entire first band-gap (see Figure 76).When it reaches the first band it collides with an unstable branch (b) which has two neighboring wells populated out-of-phase and disappears in a saddle-node bifurcation. When these branches reach the second band, they immediately become unstable as they reshape into extended solutions (see Figure 77 e,f). There does exist a second-gap soliton solution which is stable, (g). This solution disappears in a bifurcation with a marginally stable solution that has next-nearest-neighbor wells on four sides populated with intra-site dipoles. The evolution of solution (b) is represented in Figure 78 by the phase of the sites via the following quantity $\arg(u)\chi\{(x,y)||u|^2 > 0.5\max_{(x,y)}[|u|^2]\}$, where χ is the indicator function of the set that annihilates the field outside that set. All sites remain for a long propagation distance, although

the phase correlation is lost by $z = 300$.

Now, we consider the *unstable* out-of-phase hexapole ($\Delta\theta = \pi$). First, in the discrete case presented in Figure 79 the theoretical prediction of linearization eigenvalues, which are exactly a factor $-i$ times those for the in-phase solution, are confirmed for small ε. The dashed line $1 - 6\varepsilon$, which represents the smallest phonon eigenvalue, is included here to show that the actual linearization eigenvalues remain bounded by this line, similarly to what was observed for square lattices in [39]. A solution is shown for small coupling and large gap, as well as one when the gap is closing and the solution decaying. The dynamics of Figure 80 reveal that all sites survive for a long propagation distance, and, while there is no clear phase correlation between all sites, there is some correlation. For instance, the largest amplitude two next-nearest-neighbor lobes remain out-of-phase. This is again consistent with a feature that was recently observed in [36], since next-nearest-neighbor interactions are expected to be the same for focusing and defocusing non-linearities due to the staggering transformation [12]. The middle amplitude site next-nearest to both of these oscillates between in-phase with one and then the other, while there is no apparent correlation of the other three smaller amplitude sites.

The same panels as the in-phase case, Figures 76 and 77, are shown for the continuum version of the out-of-phase hexapole in Figure 81. The solution this time actually collides with a four-well structure, which is slightly more stable, due to fewer unstable pairs of populated wells. Again there are continuations through the second band to extended states and again there exists a disjoint branch of second gap states. All states here are unstable. Under dynamical evolution, again all six sites remain for a long propagation distance (not shown). However, the phase correlation breaks down as early as $z = 20$, due to the instability.

Next we look at the *stable* single charge vortex solution ($\Delta\theta = \pi/3$). The

discrete problem is predicted to be stable with double pairs of eigenvalues at $\pm i\sqrt{\varepsilon}$ and $\pm i\sqrt{3\varepsilon}$, and single pairs at $\pm 2i\sqrt{\varepsilon}$ and 0. The prediction is confirmed in Figure 82 and there is good agreement until the HH bifurcations set in with the continuous spectrum when $2\sqrt{\varepsilon} \approx \lambda_i = 1 - 6\varepsilon$ (or, when the largest eigenvalue intersects the continuous spectrum). A cascade of such bifurcations follows and an example profile and spectrum after this time are shown in the bottom left. The evolution of the unstable solution from the bottom row was investigated (not shown) and four sites decompose into essentially background radiation, while two cells opposite to one another inherit most of the power and remain close in amplitude and in-phase for a long distance. This is again in agreement with the results of [36], since in-phase opposite sites on the honeycomb cell are next-to-next-nearest-neighbors, so with a defocusing nonlinearity it is equivalent to an out-of-phase pair with a focusing nonlinearity. Many comparable amplitude out-of-phase breathers were found in [36].

The continuum version of this configuration given in Figure 83 (a) collides in a saddle-node bifurcation with an unstable configuration with additional populated sites on the perimeter, (b). The second gap version (e) collides with an unstable state (f) having two intrasite dipoles populated outside the original vortex. However, this state appears to stabilize closer to the third band. In the dynamical evolution of (b, not shown) again the original configuration of "mass" survives for a long propagation distance, while the phase correlation decomposes by $z = 100$.

The last of the six-site configurations we consider is the double-charge vortex ($\Delta\theta = 2\pi/3$). The stability predictions are again confirmed for small ε. However, due to the instability of the branch throughout its existence range, we do not present the details here for the sake of brevity. The continuum model admits similar branch structure for this solution as for previous cases. Here also, the solution is unstable

for all the cases examined. Its dynamics showed the principal sites surviving for long propagation distances, although the structure eventually disintigates. Again due to the generic instability of this branch, numerical details are omitted here.

5.2.2 Quadrupoles in the hourglass cell

Next, we consider configurations around the outer 4-site contour of the hourglass cell. Now, in this case, the five sites comprising the hourglass are not a simple curve, i.e. the curve crosses itself, and since some nodes are nearest-neighbors, while others are next-nearest, the analysis must be taken to second order for accurate predictions of all the bifurcating eigenvalues. Instead, we consider only nearest neighbors analytically and extend previous results about higher-order interactions to make qualitative predictions there.

First, we consider the in-phase quadrupole. The prediction of the discrete model to first order, i.e. for nearest neighbors, is that this configuration will have double eigenvalue pairs at $\pm 2i\sqrt{\varepsilon}$ (due to the in-phase nearest neighbors predicted to be stable). On the other hand, next-nearest neighbors which are in-phase are expected to be unstable [39, 35] and indeed a real pair does bifurcate as well. The real pair comes at higher order because it is a higher-order splitting. The results are presented in Figure 84. The panels are the same as for Figure 74. The evolution in Figure 85 reveals a unique structure with three sites very close in phase and intensity, two nearly identical and one slightly different with its intensity oscillating with larger amplitude opposite to the others. One of the sites is the originally unpopulated center site, which becomes populated when the other two disintegrate around $z = 100$.

The continuum version of this configuration disappears at the first band edge when it collides with a more unstable solution having the center site populated out-

of-phase to the others (see Figure 86). The main branch is only weakly unstable from the higher order interactions and, in fact, the second-band solution actually becomes stable for $\mu \lesssim 3$. In the dynamical evolution of the structure from Figure 86 (b), the unstable five site in-phase structure remains very robust for a long distance with reshaped phase; see Figure 87.

Next we consider the out-of-phase quadrupole. The predicted eigenvalues are the same as those of the in-phase case, multiplied by i. They are fairly accurate for small ε as one can see in the top right panel of Figure 88. The dynamical evolution of the solution given in the top row of Figure 88 reveals two pairs of uneven amplitude breathers with phases and amplitudes oscillating opposite to each other as in Figure 74 (not shown).

This solution in the continuum version, as seen in Figure 89, is always unstable. It collides with a structure that has a similar phase pattern, but which is surrounding rather than including the original configuration. At the point of bifurcation the common structure they share is two rows of opposite phase. Again the unstable configuration persists for a long propagation distance, suffering merely a reshaping of the relative phase (see Figure 90).

Finally, we turn to the quadrupole solution which has its nearest-neighbors in-phase and the next-nearest ones out-of-phase. The theoretical prediction for the discrete model based on the set of all possible dipole configurations always implies stability. Of course, as with the other stable solutions, stability here is conditional, in the sense that there do exist eigenvalues of negative Krein signature which lead to Hamiltonian-Hopf bifurcations upon collision with the phonon band. Indeed the precise first order calculation predicts this configuration will also be stable with two pairs of eigenvalues at $\pm i2\sqrt{\varepsilon}$. Moreover, previous results [39, 35] predict that next-nearest neighbors which are out-of-phase will be stable, and all those in

this configuration (except the ones which are also nearest) are out-of-phase. The agreement is very good again as given in the top right panel of Figure 91.

The dynamical evolution of an unstable solution in this configuration (from the bottom panels of Figure 91) (shown in Figure 92), again reveals the usual in-phase to out-of-phase uneven intensity breather pair, as shown first in Figure 75.

The continuum version is presented in Figure 93. Stable first and second band versions of the solution are identified and again there are bifurcations at the first and second bands, and also intermediate as well as extended solutions. The solution that collides with the main branch at the first band-edge (b) was propagated (not shown) and again the original sites persist and the relative phase reshapes after $z = 50$.

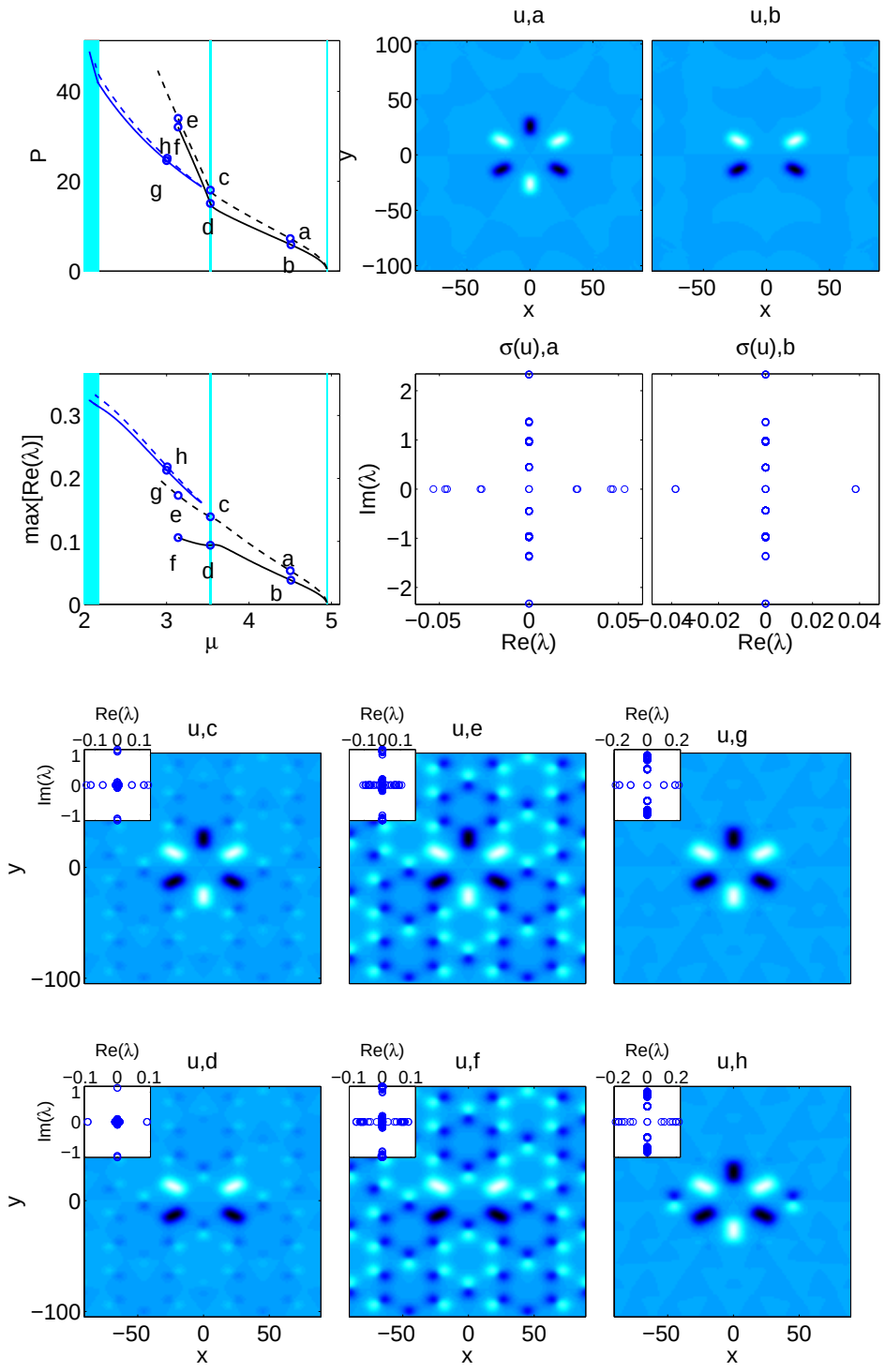

Figure 81. The same panels as Figures 76 and 77, but for the unstable out-of-phase hexapole.

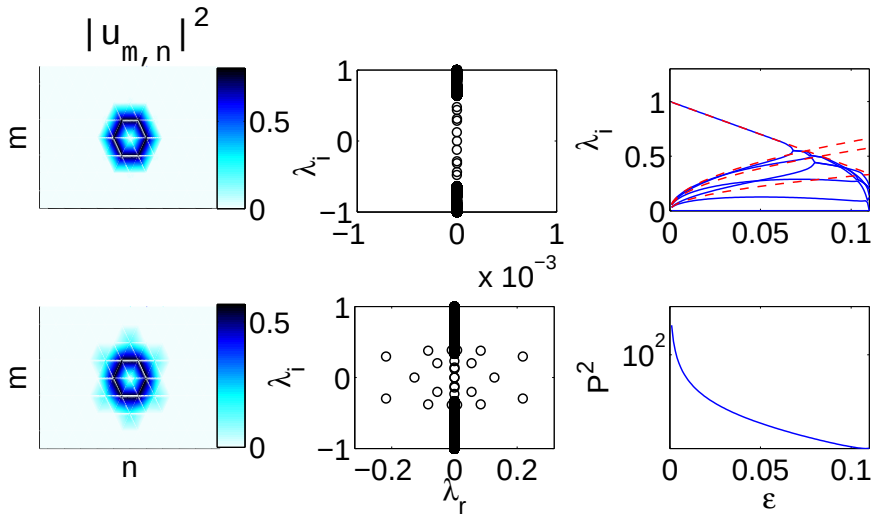

Figure 82. The same panels as Figure 74 except for the stable single charge vortex solution and the modulus of the profiles are given, i.e. $|u|^2$ instead of u. The particular solutions are for $\varepsilon = 0.06$ (top) and $\varepsilon = 0.11$ (bottom).

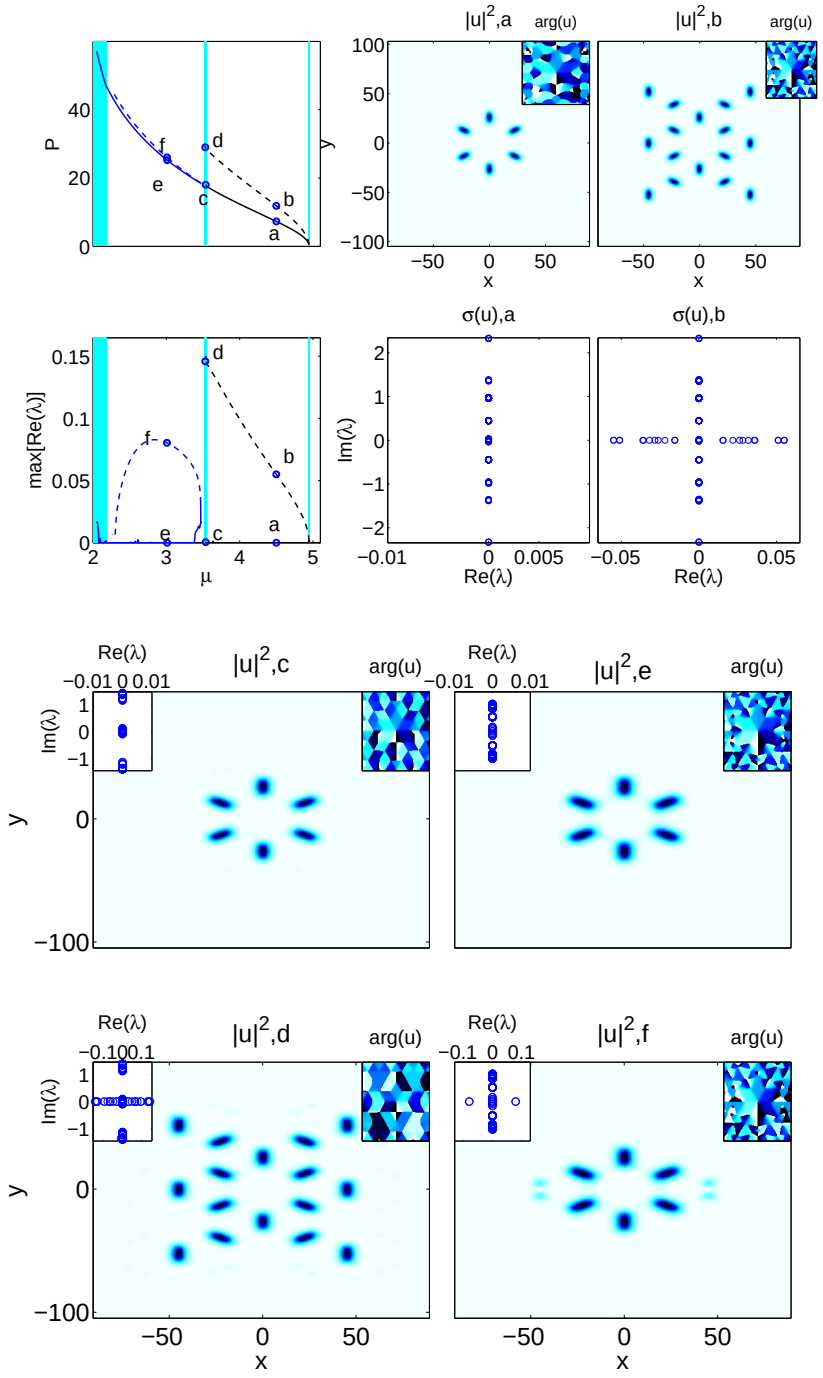

Figure 83. The same panels as Figure 81, but for the single charge vortex solution and again the modulus is given in lieu of the field itself. Here there are small embedded panels in the top right corners of the profile images with the phase of the solution.

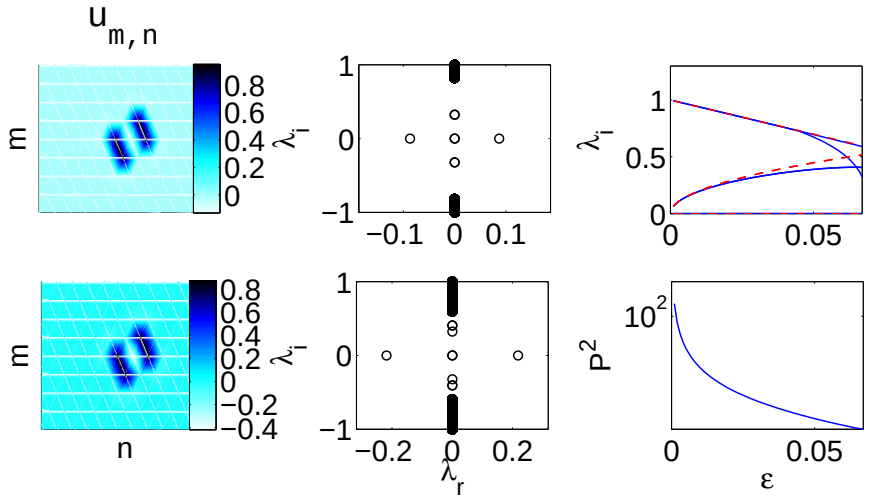

Figure 84. The same panels in the left two columns as Figure 74 except for the unstable in-phase quadrupole in the hourglass cell. The particular solutions shown are for $\varepsilon = 0.03$ (top) and $\varepsilon = 0.067$ (bottom).

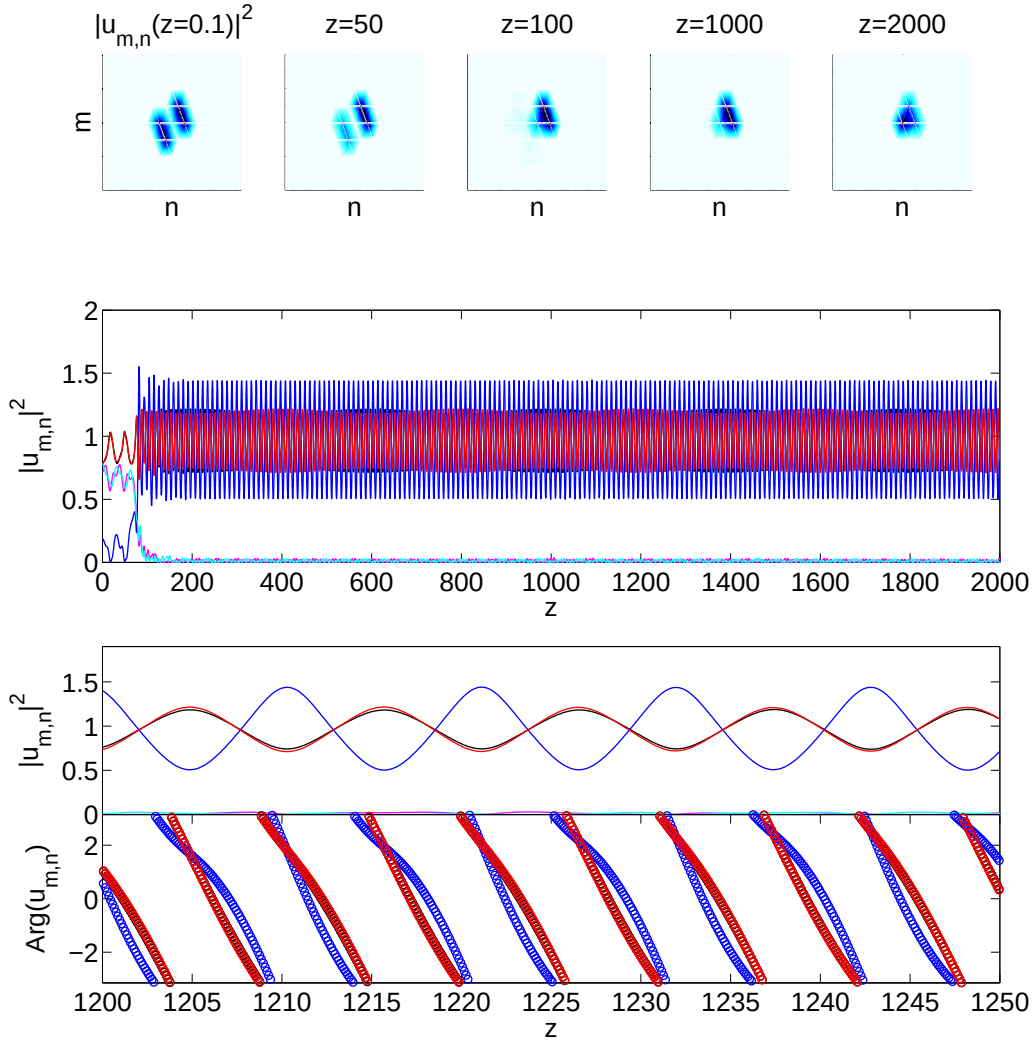

Figure 85. The same as Figure 75 for the in-phase quadrupole given in the bottom row of Figure 84. The center site becomes populated around $z = 100$ and the remaining in-phase tripole (expected to be stable) persists for a long distance with two sites almost exactly in-phase, and with equal amplitudes, while the other has much larger oscillations in amplitude opposite to the other two, but has very similar phase.

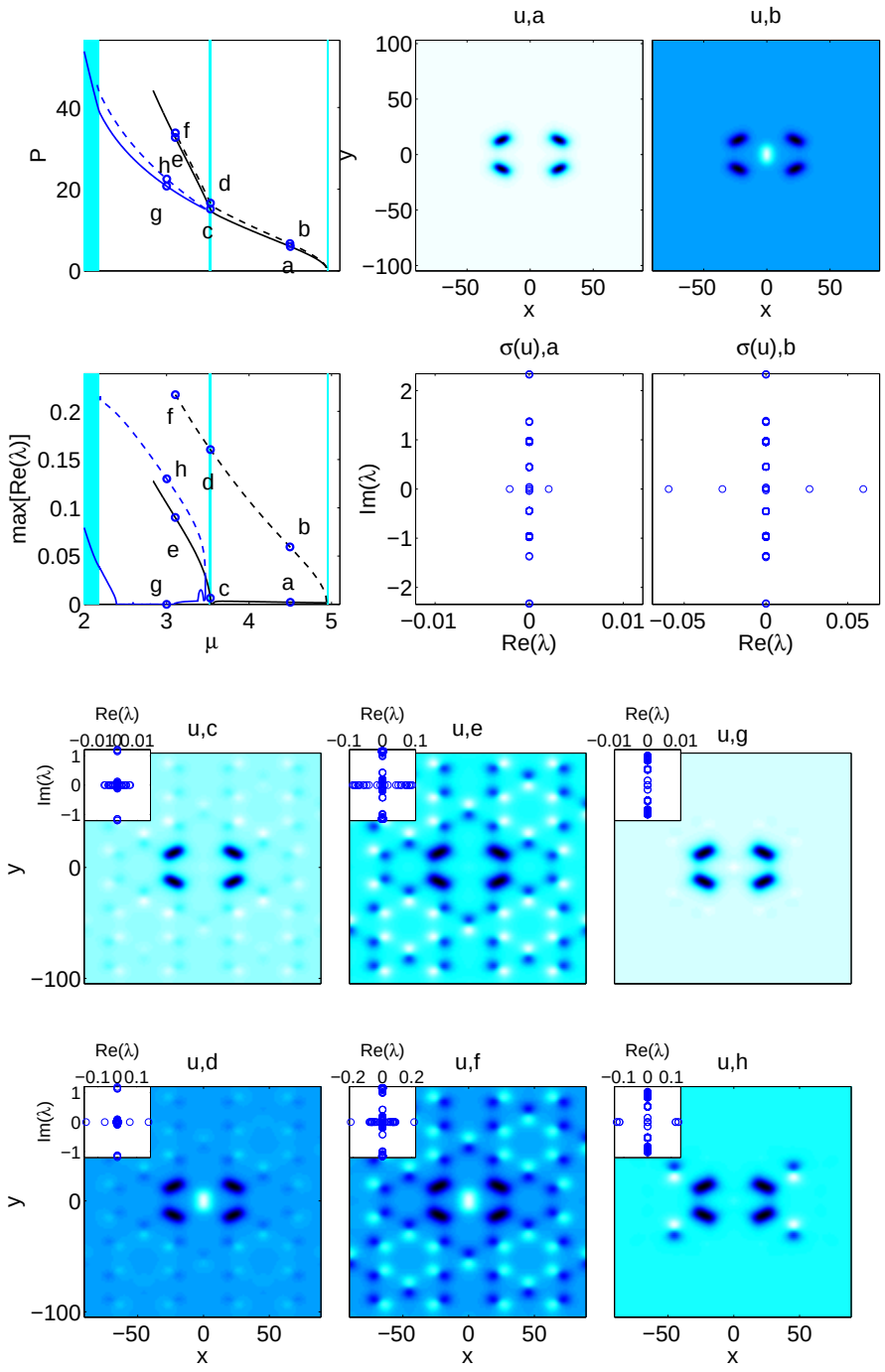

Figure 86. The same panels as Figure 81, but for the in-phase quadrupole. A more unstable configuration with the center well populated out-of-phase collides with this one close to the first band-edge.

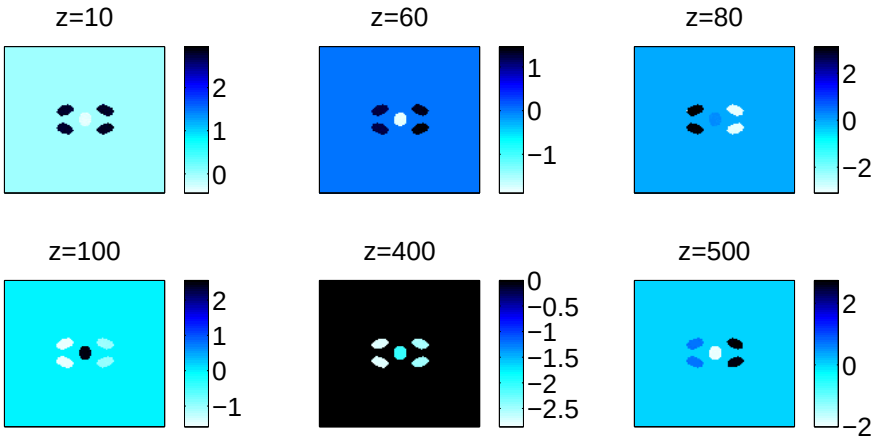

Figure 87. The same as Figure 78 but for the in-phase quadrupole from Figure 86 (b). The initial relative phase loses the correlation after $z = 60$ and the structure again persists for a long distance.

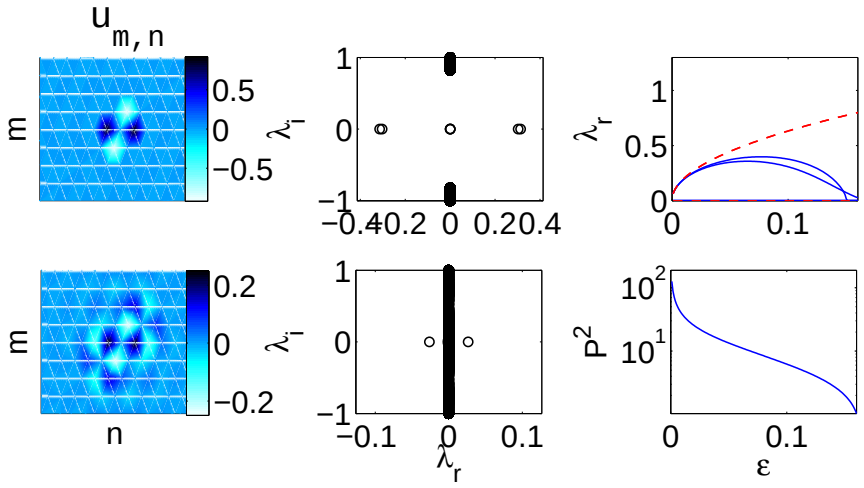

Figure 88. The same panels as Figure 84 except for the unstable out-of-phase quadrupole. The particular solutions shown are for $\varepsilon = 0.03$ (top) and $\varepsilon = 0.16$ (bottom).

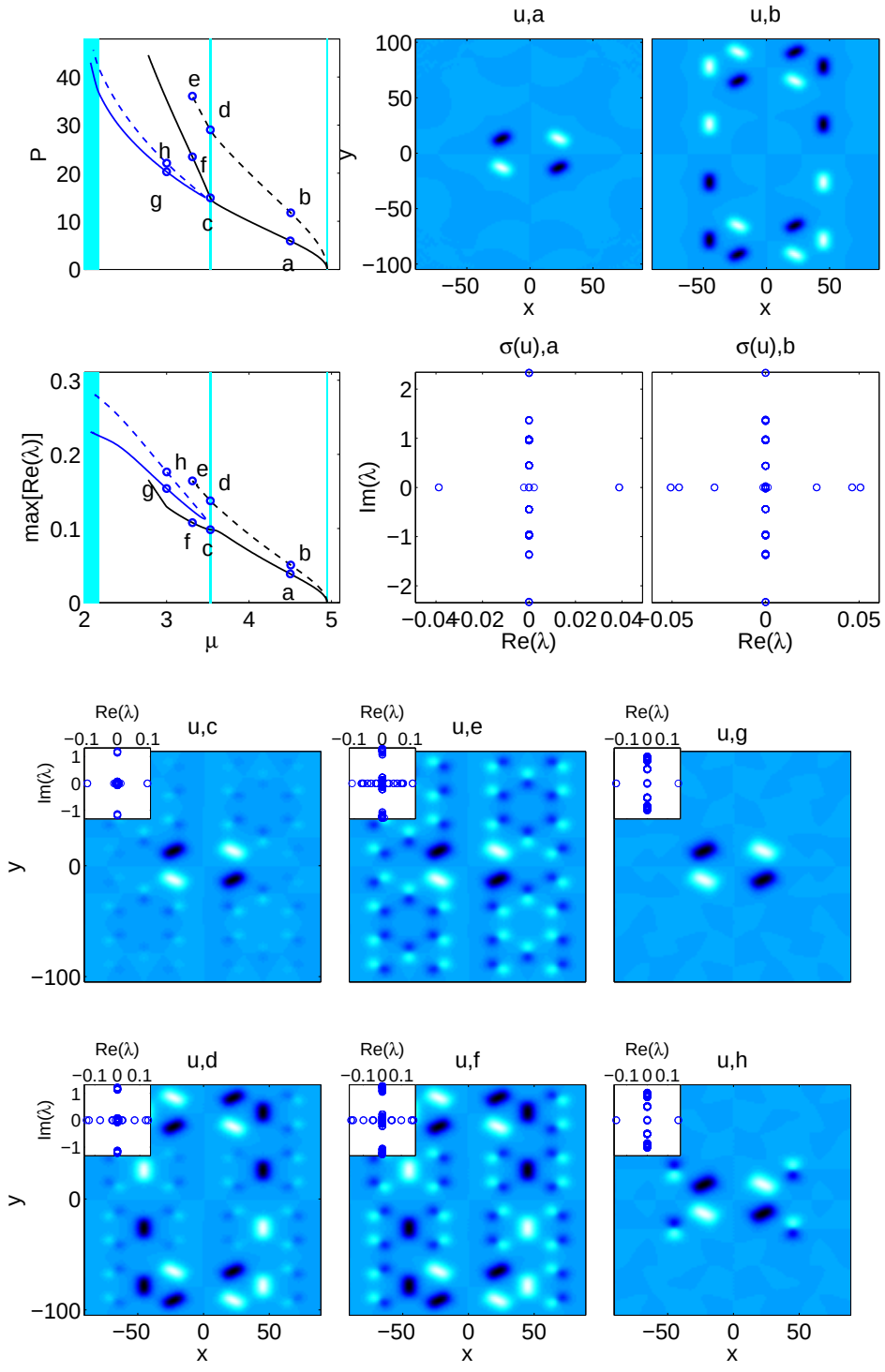

Figure 89. The same panels as Figure 81, but for the out-of-phase quadrupole. It collides with a branch that has a similar phase pattern as the original configuration.

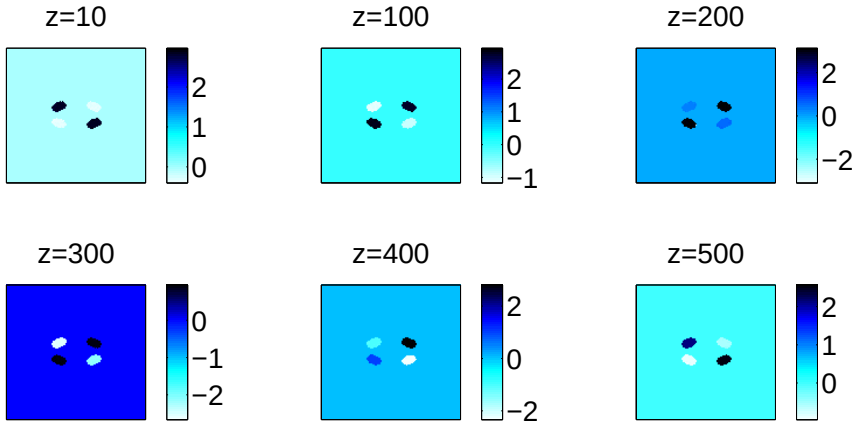

Figure 90. The same as Figure 78 but for the unstable out-of-phase quadrupole given in Figure 89 (a).

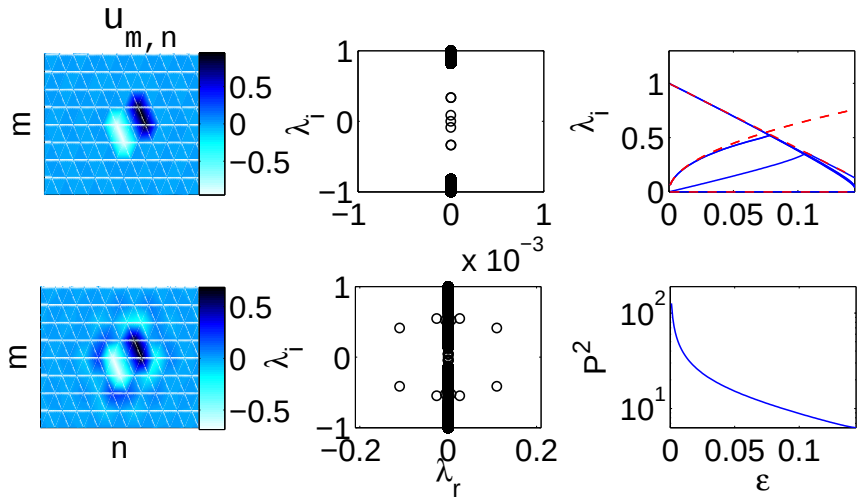

Figure 91. The same panels as Figure 74 except for the stable in-phase/out-of-phase quadrupole. The particular solutions shown are for $\varepsilon = 0.03$ (top) and $\varepsilon = 0.144$ (bottom).

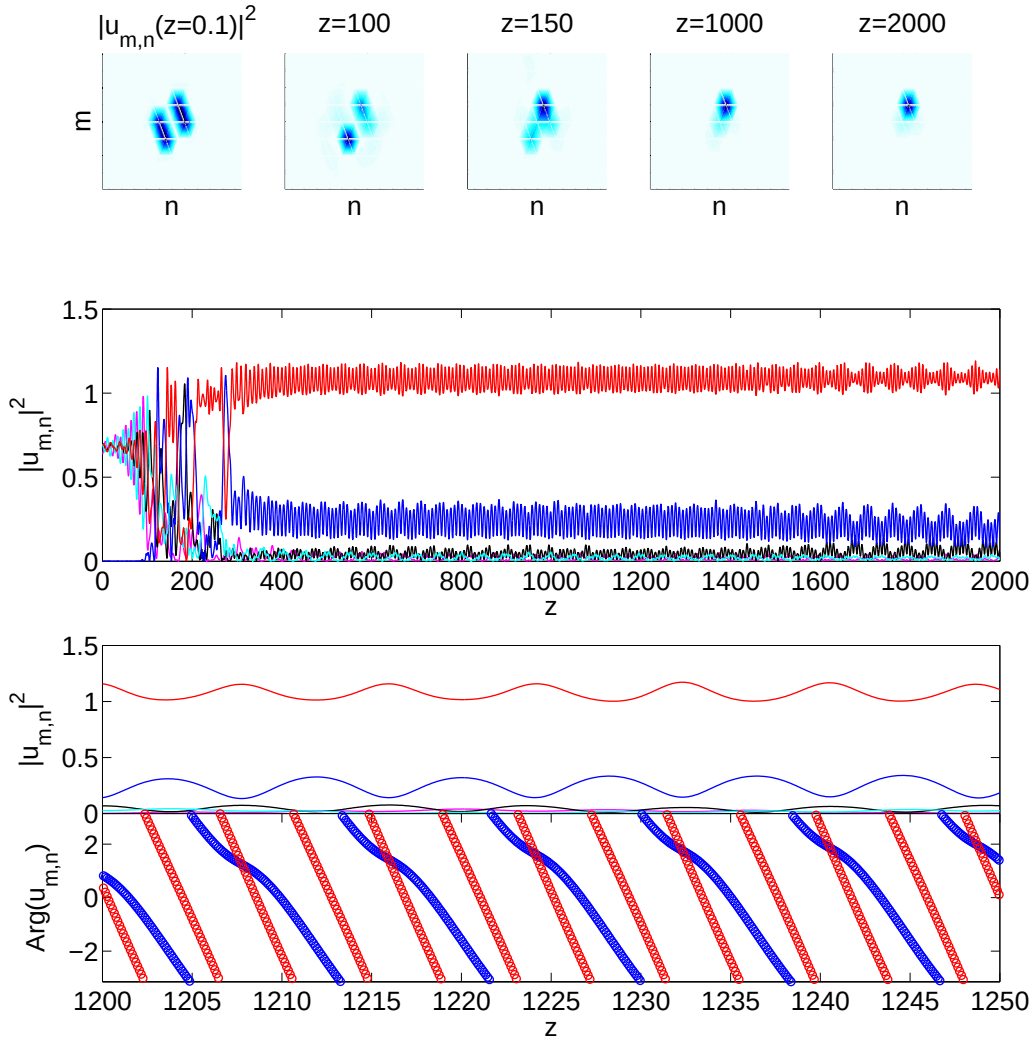

Figure 92. The same as Figure 75 for the in-phase/out-of-phase solution with $\varepsilon = 0.144$ from the bottom panels of Figure 91. Notice the instability takes a considerable distance to develop due to the small magnitude of the complex quartet of eigenvalues.

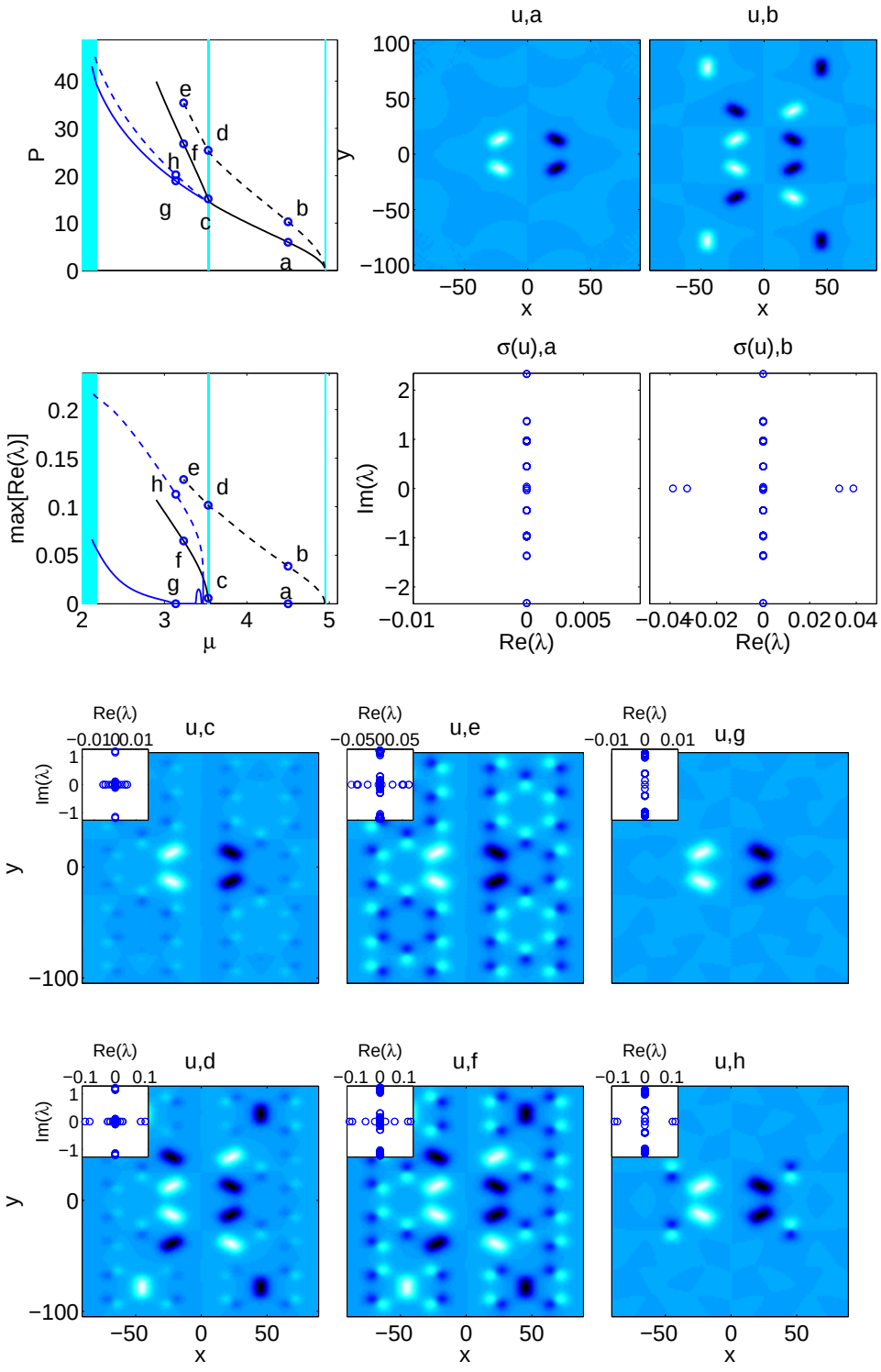

Figure 93. The same as Figure 81 for the in-phase/out-of-phase solution.

CHAPTER 6

CONCLUSIONS AND FUTURE DIRECTIONS

To conclude, I have systematically extended studies of the existence, stability, and dynamics of NLS systems in the presence of periodic external potentials to various different 2D geometries, including hexagonal, honeycomb, and Kagomé and nonlinearities including cubic and saturable, and both focusing and defocusing. In particular, qualitative, and indeed quantitative where relevant, comparisons of existence and stability have been made between analytical results based on expansion around a discrete reduced model close to the integrable zero-coupling limit, numerical results for the full discrete model, and numerical results for an approximation to the full continuum model relevant to experiments of nonlinear pulse propagation in photonic lattices in photorefractive crystals. Furthermore, direct comparison to actual experiments with SBN have been presented with good agreement. Additionally, dynamical evolution of unstable solutions is examined and compared with experiments, again with good agreement.

Further directions are numerous, but obvious candidates include investigating different lattice symmetries, including various anisotropic varieties and quasiperiodic structures, and higher dimensional extensions, such as the 3D hexagonal close-packed lattice, for which the applicability to nonlinear optics is limited, but for which application may be found in other areas of science, such as solid-state physics.

Of course, exploration of the application of the results obtained herein to various particular examples of the enumerable possibilities would be another interesting avenue to explore. Also, it would be interesting to investigate deeper the theoretical framework underlying all Hamiltonian systems, in terms of theories of Krien and Morse, and also to investigate further the numerical framework considered here possibly in the context of the more general problem of optimization which is ubiquitous throughout Applied Mathematics.

APPENDIX A

NUMERICAL COMPUTATIONS USING FULL MATRICES

In this Section, we briefly discuss the numerical methods that have been used extensively throughout this thesis to obtain the numerical solutions discussed herein, as well as to analyze their linear stability and to propagate them in time (for example, to examine their dynamical instability, or to confirm their numerical stability).

Our tool of preference, regarding the numerical identification of solutions consists of the so-called Newton-Raphson (or simply Newton) method. We choose the Newton method because of its quadratic convergence, upon the provision of a suitably good initial guess [80]. It should be clearly indicated here that different groups use different methods to obtain stationary solutions. For instance, methods based on rewriting the standing wave problems of interest in Fourier space and applying Petviashvili's iteration scheme have been proposed [81, 82] and shown to converge for nonlinear Schrödinger type problems under suitable conditions [83]. Also, methods based on imaginary time integration have been proposed and suitably accelerated [84]; finally, also methods based on constrained minimization of appropriate (e.g., energy) functionals have been developed [85]. However, for the standing wave DNLS problem, given the existence of the anti-continuum limit of zero coupling, and its analytical tractability (which provides an excellent initial guess and

a starting point for parametric continuations), the Newton method posed on the lattice works extremely efficiently. Notice that although the Newton method will be presented herein in a simple parametric continuation format, with respect to the coupling parameter ϵ, it is straightforward to combine it also with pseudo-arclength ideas such as the ones discussed in [44], in order to be able to continue the solution past fold points (and to detect relevant saddle-node bifurcations). Although for one-dimensional problems (and even for two-dimensional discrete problems), it is straightforward to use the direct Newton algorithm with full matrices and then perform the linear stability analysis with full eigensolvers, in three-dimensions (or e.g., in two-dimensional multi-component systems), the relevant computations become rather intensive. To bypass this problem, we offer a possibility to perform the Newton method (and the subsequent eigenvalue computations) using sparse iterative solvers and sparse matrix eigensolvers that considerably accelerate the computation, based on the work of Kelley [43].

As concerns the direct numerical integration of the DNLS model, our tool of choice for the time stepping herein will be the 4th-order Runge-Kutta method [80]. Although both lower order methods (such as the efficient split-step Fourier method [86]), as well as higher order methods (including even the 8th-order Runge-Kutta method [87]) have been presented and used in the literature, our use of the 4th order method, we feel, represents a good balance between a relatively high-order local truncation error (accuracy) and stability properties that allow a relatively high value of the time-step ($dt = 10^{-3}$ or higher for most cases of interest here) without violating stability conditions.

All of the above methods (existence, linear stability and direct integration) will be presented by means of MATLAB [88] scripts in what follows. The scripts will be vectorized to the extent possible to allow for efficient numerical computation and

will also be set up to provide "on the fly" visualization of the relevant parametric continuations (for our bifurcation calculations) and the time-stepping evolution (for our direct integrations).

We start with a numerical implementation of the one-dimensional Newton algorithm. We recall that the algorithm assumes the simple form $x^{m+1} = x^m - f(x^m)/f'(x^m)$ for approximating the solution x^s such that $f(x^s) = 0$ [m here denotes the algorithm iteration index]. The N-dimensional vector generalization for a lattice of N-sites in our one-dimensional problem reads:

$$\mathbf{J} \cdot \left(\mathbf{x}^{m+1} - \mathbf{x}^m\right) = -\mathbf{F}(\mathbf{x}^m), \tag{A.1}$$

where $\mathbf{J}$ is the Jacobian of the (vector of) N equations $\mathbf{F}$ with respect to the (vector of) N unknowns $\mathbf{x}$, i.e., $J_{ij} = \partial F_i/\partial x_j$. We are writing Eq. (A.1) as indicated above for a reason, namely to highlight that it is far less expensive to perform the Newton algorithm iteration step as a solution of a linear system (for the vector $\mathbf{x}^{m+1}$), rather than through the inversion of the Jacobian. The vector $\mathbf{x}$ in the computations below consists of the lattice field variables u_n, satisfying the vector of equations

$$F_n = \epsilon\Delta_2 u_n + u_n^3 - u_n = 0 \tag{A.2}$$

where we have taken advantage of the real nature of the 1d solutions (although the algorithm can be straightforwardly generalized to complex solutions as needed in higher dimensions). Once the solutions of Eq. (A.2) are identified to a prescribed accuracy (set below to 10^{-8}), linear stability analysis is performed around the solution. The code detailing these bifurcation computations, along with relevant commenting of each step is given below.

```
clear; format long;
```

```
% number of sites;
n=100;
% initial coupling;
% for discrete version, typically at AC-limit eps=0;
eps=0;
% for continuum, eps ∝ 1/(Δx)^2 >> 1 as follows;
dx=0.1; eps=1/dx/dx;
% and the continuation is in the propagation constant, l below
% propagation constant; typically set to 1;
% continuation is in this parameter for the continuum problem.
l=1;
% above depends on the sign of the nonlinearity
% (±1 for the discrete version and any value for the continuum)
sgn=-1;
% field initialization
u1=zeros(1,n);
u1(n/2)=sqrt(l);
u1(n/2+1)=sqrt(l);
% iteration index
it=1;
% lattice index
x=linspace(1,n,n)-n/2;
%for continuum version, this is space:  x → x/(Δx)
x=dx*x;
% external potential for continuum version
% d, lattice period, should be chosen such that d ≪ L = dx * n
d=30;
```

```
k=2*pi/d;
V = cos(k*x).^2;
% the initial guess for the continuum version will of course be different.
% typically an appropriately arranged collection of Gaussian wavepackets
% of the following form are used
cx=d/2;a=1;b=1;
u=a*exp(-(x-cx).^2*b);
% continuation in coupling epsilon
% discrete version, no external potential
V=0;
while (eps<0.101)
u=zeros(1,n);
while (norm(u-u1)>1e-08)
u=u1;
% evaluation of second difference with free boundaries
sd2=diff(u,2); sd1=u1(2)-u1(1); sdn=u1(n-1)-u1(n); sd=[sd1,sd2,sdn];
% equation that we are trying to solve
f=-l*u-V+eps*sd+(u1.^2).*u1;
% auxiliary vectors in Jacobian
ee = eps*ones(1,n);
ee0=ee; ee0(1)=ee(1)/2; ee0(n)=ee(n)/2;
ee1=(-2*ee0-l*ones(1,n)-V+3*(u1.^2));
%tridiagonal Jacobian
jj1 = spdiags([ee' ee1' ee'], -1:1, n, n);
% Newton correction step
cor=( jj1 \ f' )'; u1=u-cor;
% convergence indicator:  should converge quadratically
```

```
norm(cor)
end;
% auxiliary vector for stability
ee1=(-2*ee0-l*ones(1,n)-V+2*abs(u1.^2));
% construction of stability matrix
jj2=spdiags([ee' ee1' ee'], -1:1, n, n);
jj3=diag(u1.^2);
jj4=[ jj2, jj3;
-conj(jj3) -conj(jj2)];
% eigenvalues d and eigenvectors v of stability matrix
[v,d]=eig(full(jj4));
d1=diag(d);
% store solution and stability
u_store(:,it)=u';
d_store(:,it)=d1;
e_store(it)=eps;
% visualize the continuation profiles and stability on the fly
subplot(2,1,1)
plot(x,u,'-o')
drawnow;
subplot(2,1,2)
plot(imag(d1),real(d1),'o')
drawnow;
% increment indices and epsilon
it=it+1;
eps=eps+0.001;
end;
```

```
% save the profiles and other data
save('sol_eps_1d.mat','u_store','d_store','e_store')
```

A prototypical result of the continuation of the above code has been given below (the code addresses the unstable case with two excited sites –the intersite mode–) using the command

```
imagesc(0.001*linspace(0,100,101),linspace(1,100,100)-50,u_store)
```

to spatially visualize the branch for different values of ϵ. Also the dominant stability eigenvalues of this unstable branch are shown (more specifically, λ^2) via the commands

```
d2=sort(real(d_store.^2));
plot(e_store,d2(1,:),e_store,d4(3,:),'b--',e_store,d4(5,:),'b-.')
```

We now turn to the numerical integration of one of the unstable solutions of the above branch (namely, of the solution for $\epsilon = 0.1$) that we saved at the end of the previous bifurcation code. As indicated above, we use the 4th order Runge-Kutta method whose four steps and subsequent integration step, we now remind, for the solution of the vector of ordinary differential equations $\mathbf{x}' = \mathbf{f}(t, \mathbf{x})$ with initial

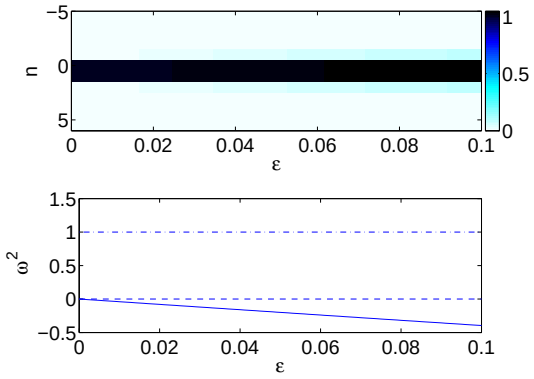

Figure 94. The top panel shows the result of continuation as a function of ϵ of the solution profile (shown in contour plot). The bottom panel shows the result of the linear stability analysis, indicating the instability of this inter-site mode, through the presence of a negative squared eigenfrequency (solid line). The dashed pair of eigenvalues at the origin is due to the phase invariance, while the dash-dotted pair at 1 (due to the choice of propagation constant $\Lambda = 1$) indicates the lower edge of the continuous spectrum.

condition $\mathbf{x}(t_0) = \mathbf{x}^0$

$$\mathbf{k}^{(1)} = dt\ \mathbf{f}\left(t^m,\ \mathbf{x}^m\right) \tag{A.3}$$

$$\mathbf{k}^{(2)} = dt\ \mathbf{f}\left(t^m + \frac{dt}{2},\ \mathbf{x}^m + \frac{dt}{2}\ \mathbf{k}^{(1)}\right) \tag{A.4}$$

$$\mathbf{k}^{(3)} = dt\ \mathbf{f}\left(t^m + \frac{dt}{2},\ \mathbf{x}^m + \frac{dt}{2}\ \mathbf{k}^{(2)}\right) \tag{A.5}$$

$$\mathbf{k}^{(4)} = dt\ \mathbf{f}\left(t^m + dt,\ \mathbf{x}^m + dt\ \mathbf{k}^{(3)}\right) \tag{A.6}$$

$$\mathbf{x}^{m+1} = \mathbf{x}^m + \frac{1}{6}\left(\mathbf{k}^{(1)} + 2\mathbf{k}^{(2)} + 2\mathbf{k}^{(3)} + \mathbf{k}^{(4)}\right) \tag{A.7}$$

The commented version of the MATLAB script that implements this algorithm for the DNLS equation is given below.

```
% parameters
% (shown is discrete example with sgn=-1)
```

```
n=100; eps=0.1;
% load solutions from Newton
load sol_eps_1d.mat
u_num=10
u=u_store(:,u_num)'+1e-04*rand(1,n);
x=real(u); y=imag(u);
% spatial lattice index
sp=linspace(1,n,n)-n/2;
% iteration indices and time step
it=1;
dt=0.001;
it1=1;
it2=1;
% integration up to t=100
while ((it-1)*dt<100)
% computation of second differences and 1st RK integration step
d2y=diff(y,2); ad1y=(y(2)-y(1)); ad3y=(y(n-1)-y(n));
d2x=diff(x,2); ad1x=(x(2)-x(1)); ad3x=(x(n-1)-x(n));
p1=[ad1y,d2y,ad3y]; p2=[ad1x,d2x,ad3x];
k1x=dt*(-eps*p1-y.*(x.^2+y.^2));
k1y=dt*(eps*p2+x.*(x.^2+y.^2));
a=x+k1x/2;
b=y+k1y/2;
% computation of second differences and 2nd RK integration step
d2y=diff(b,2); ad1y=(b(2)-b(1)); ad3y=(b(n-1)-b(n));
d2x=diff(a,2); ad1x=(a(2)-a(1)); ad3x=(a(n-1)-a(n));
p1=[ad1y,d2y,ad3y]; p2=[ad1x,d2x,ad3x];
```

```
k2x=dt*(-eps*p1-b.*(a.^2+b.^2));
k2y=dt*(eps*p2+a.*(a.^2+b.^2));
a=x+k2x/2;
b=y+k2y/2;
% computation of second differences and 3rd RK integration step
d2y=diff(b,2); ad1y=(b(2)-b(1)); ad3y=(b(n-1)-b(n));
d2x=diff(a,2); ad1x=(a(2)-a(1)); ad3x=(a(n-1)-a(n));
p1=[ad1y,d2y,ad3y]; p2=[ad1x,d2x,ad3x];
k3x=dt*(-eps*p1-b.*(a.^2+b.^2));
k3y=dt*(eps*p2+a.*(a.^2+b.^2));
a=x+k3x;
b=y+k3y;
% computation of second differences and 4th RK integration step
d2y=diff(b,2); ad1y=(b(2)-b(1)); ad3y=(b(n-1)-b(n));
d2x=diff(a,2); ad1x=(a(2)-a(1)); ad3x=(a(n-1)-a(n));
p1=[ad1y,d2y,ad3y]; p2=[ad1x,d2x,ad3x];
k4x=dt*(-eps*p1-b.*(a.^2+b.^2));
k4y=dt*(eps*p2+a.*(a.^2+b.^2));
% completion of integration from t -> t+dt
x1=x+(k1x+2*k2x+2*k3x+k4x)/6;
y1=y+(k1y+2*k2y+2*k3y+k4y)/6;
% square modulus profile
uu=x1.^2+y1.^2;
% evaluate energy and (l^2 norm)^2 & visualize the solution every few steps
if (mod(it,100)==0)
% time counter
tim(it1)=(it-1)*dt;
```

```
% square l^2 norm; should be conserved
l2(it1)=sum(uu);
% energy calculation; energy should also be conserved
% although to lower accuracy than l2
gr=[diff(x1,1),0]; gr1=[diff(y1,1),0];
ener(it1)=sum(eps*(gr.^2+gr1.^2)-uu.^2/2);
% plot the solution and its energy and l2 norm
subplot(2,1,1)
plot(sp,uu,'-')
drawnow
subplot(2,1,2)
plot(tim,l2,tim,ener,'--')
drawnow
if (mod(it,1000)==0)
u_store(:,it2)=x1+sqrt(-1)*y1;
it2=it2+1;
end;
it1=it1+1;
end;
it=it+1;
x=x1;
y=y1;
end;
```

The result of the integration for the unstable evolution of the solution is shown in Figure 95 (notice that in the initial condition the exact solution was perturbed by a random uniformly distributed noise field of amplitude 10^{-4} in order to seed

the instability). It can be seen how the two-site solution transforms itself into a breathing mode oscillating between a two-site and a single-site solution. On the other hand, the bottom panel of the figure shows the deviation from the relevant (for the DNLS) conservation laws of the energy and the squared l^2 norm. Both of these deviations are of $O(10^{-13})$ as can be seen in the panel while the means of these quantities are of O(1) for the presented simulation. This confirms the good preservation by the proposed scheme of the important conservation laws of the underlying physical model. The above panels are created in MATLAB through the use of the commands:

```
subplot(2,1,1)
imagesc(linspace(1,100,100),sp,abs(u_store.^2))
subplot(2,1,2)
plot(tim,l2-mean(l2),'--',tim,ener-mean(ener))
```

Extending the above type of numerical considerations to higher dimensions is conceptually straightforward, although both computationally tedious and obviously far more numerically intensive. We briefly indicate how the above considerations would generalize in two-dimensions (three-dimensional generalizations would naturally extend along the same vein), however we focus in the next section on how to render these computations more efficient in higher dimensional settings by means of the use of sparse matrix computations and iterative linear solvers.

In the 2d case, the Newton iteration has to extend over a grid of $N \times N$ points, hence the relevant vectors have N^2 elements (more generally N^d for d-dimensional computations). The key realization concerning the performance of operations such as those of Eq. (A.1) with such vectors stemming from higher dimensional grids

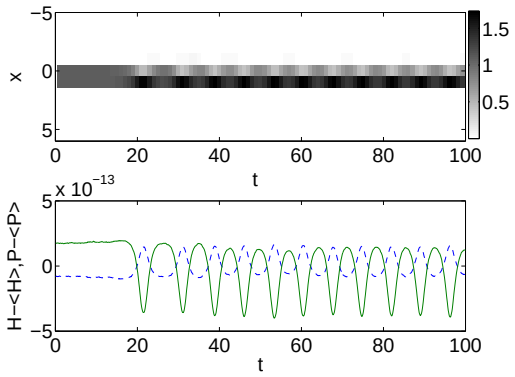

Figure 95. The top panel shows the result of the direct integration of the unstable inter-site centered solution for $\epsilon = 0.1$, with the instability being seeded by a random (uniformly distributed) perturbation of amplitude 10^{-4}. The space-time contour plot of the solution shows how t results into a breathing mode oscillating between the initial condition and a single-site centered mode. The bottom panel of the figure shows the deviation from the energy H (solid line) and the squared l^2 norm P (dashed line) conservation. The average energy during the simulation is ≈ -1.007, while the mean of the squared l^2 norm is ≈ 2.199. In both cases, we can see that the deviations from this conservation law are of $\mathbf{O}(10^{-13})$.

is that not all points should be treated on the same footing. Taking perhaps the simplest case of vanishing Dirichlet boundary conditions at the edges of our two-dimensional domain, it should be appreciated that while the "inner" $(N-2)\times(N-2)$ nodes of the domain are "regular" points possessing all 4 of their neighbors, there exist an additional $4\times(N-2)$ "edge" points with only 3 neighbors, while the 4 corner points only have 2 neighbors. That is to say, these points should be treated separately regarding both the equation they satisfy and the nature of their corresponding Jacobian elements. Upon this realization, one can treat the two-dimensional grid as a one-dimensional vector whose elements $(1,1),\ldots,(1,N)$ become elements $1,\ldots,N$, elements $(2,1),\ldots,(2,N)$ becomes $N+1,\ldots,2N$, and

so on. Then, when constructing the full Jacobian, one should test whether the vector index i running from 1 to N^2 lies at the corners (1, N, N^2-N+1 and N^2), or at the edges $1 < i < N$, $N^2-N+1 < i < N^2$, $\mathrm{mod}(i,N) = 1$ or $\mathrm{mod}(i,N) = 0$). This testing can be constructed through appropriate if statements, or equivalently by more clever vector manipulations particularly well suited for MATLAB. If none of the above happens, then one has all 4 neighbors (which for the element i are $i+1$, $i-1$, $i+N$ and $i-N$ in the quasi-1d vector implementation of the grid). Using these considerations one can construct the corresponding Jacobian and perform the same bifurcation computations as above.

As regards 2d Runge-Kutta simulations, things are in fact a bit simpler, as no Jacobian evaluations are needed. Then assuming that the field (and its second differences) are vanishing at the boundaries, which is a reasonable assumption, for the vast majority of the configurations considered in this book, we can construct the 2nd difference operators in a simple vectorized manner as follows:

```
e=zeros(n,1);
Dxmm = diff([e';x;e'],2,1);
Dxnn = diff([e,x,e],2,2);
Dymm = diff([e';y;e'],2,1);
Dynn = diff([e,y,e],2,2);
```

Using these second differences along the two lattice directions, it is straightforward to again perform the steps used to obtain the intermediate integration vectors $\mathbf{k}^{(j)}$ $j = 1, \ldots, 4$, e.g., as follows:

```
k1x=dt*(-eps*(Dymm+Dynn)-y.*(x.^2+y.^2));
```

```
k1y=dt*(eps*(Dxmm+Dxnn)+x.*(x.^2+y.^2));
```

Modulo this small modification, the one-dimensional Runge-Kutta realization given above can be essentially immediately transferred into a 2d integrator, upon suitable provision of $N \times N$ vector initial conditions $\mathbf{x}_0$, $\mathbf{y}_0$. The same type of considerations can be immediately extended to 3d computations with Dxmm, Dxnn and Dxll computed similarly using the diff command.

APPENDIX B

NUMERICAL COMPUTATIONS USING SPARSE MATRICES AND ITERATIVE SOLVERS

We discuss two among the many methods for efficiently computing the solution of the Newton fixed point in two-dimensions using finite difference derivatives. The more straightforward method is to utilize the sparse banded structure of the Jacobian and the efficiency of the MATLAB command "backslash", which will automatically recognize the banded structure and use a banded solver. If memory is not the main consideration, this method is faster. However, one can save a fraction of the memory (this becomes exaggerated as the system size grows) at the cost of a slightly slower computation utilizing a Newton-Krylov GMRES scheme as implemented by the MATLAB script nsoli [43]. The memory is minimized by using an Arnoldi iterative algorithm to solve the linear system at each iteration of the Newton method and approximating the Jacobian only in the direction of the Krylov subspace. We note that beyond the standard case outlined here this has far-reaching benefits, particularly when the explicit form of the Jacobian is unknown, or when employing a pseudo-arclength method, for instance, which spoils the banded structure of the Jacobian.

First, we will outline the analogous two-dimensional standard Newton solver (without the tedium of if statements) utilizing the structure and sparsity of the

Jacobian.

```
clear; format long;
% number of sites;
n=100;
% initial coupling; typically at AC-limit eps=0;
eps=0;
% propagation constant; typically set to 1.
l=1;
% above depends on the sign of the nonlinearity
% (±1 for the discrete version and any value for the continuum)
sgn=-1;
% field initialization
u1t=zeros(n,n);
u1t(n/2,n/2)=sqrt(l);
u1t(n/2+1,n/2)=sqrt(l);
% reshape the field into a column vector with real and
% imaginary parts separated for solving
u1=[reshape(real(u1t),n*n,1);reshape(imag(u1t),n*n,1)];
% iteration index
it=1;
% lattice indices as vectors
x=linspace(1,n,n)-n/2;
y=linspace(1,n,n)-n/2;
% lattice indices as matrices
[X,Y]=meshgrid(x,y);
% external potential for continuum (X,Y → X/Δx,Y/Δy)
```

```
d=30;
k=2*pi/d;
V=0;NV=3
for j=1:NV
V=V+exp(i*(k*(cos(2*pi*j/NV)*XX+sin(2*pi*j/NV)*YY)));
end
% the initial guess for the continuum version will of course be different.
% typically an appropriately arranged collection of Gaussian wavepackets
% of the following form are used (for a single site in a square lattice)
cx=d/2;cy=d/2;a=1;b=1;
u=a*exp(-((x-cx).^2+(y-cy).^2)*b);
% continuation in coupling epsilon
% (for continuum version we continue in a different parameter,
% usually the propagation constant, l)
eps=0; V=0;
% define increment
inc = .001;
while (eps<0.101)
eps=eps+inc;
u=zeros(2*n*n,1);
% BEGIN - see alternative method below
%
while (norm(u-u1)>1e-08)
u=u1;
% fill in the real and imaginary parts of the original 2d field
uur = u(1:n*n);
ur = reshape(uur,n,n);
```

```
uui = u(n*n+1:2*n*n);
ui = reshape(uui,n,n);
% evaluation of second difference with zero fixed boundaries
e=zeros(n,1);
Durmm = diff([e';ur;e'],2,1);
Durnn = diff([e,ur,e],2,2);
Duimm = diff([e';ui;e'],2,1);
Duinn = diff([e,ui,e],2,2);
Dur = Durmm + Durnn;
Dui = Duimm + Duinn;
% Other boundary conditions can be implemented similarly,
% for instance use the following for free boundaries
% diff([ur(1,:);ur;ur(n,:)],2,1); ...  etc.
% equation that we are trying to solve (vectorized)
f=[reshape(-(l+V)*ur+eps*Dur-sgn*(ur.^2+ui.^2).*ur,n*n,1); ...
   reshape(-(l+V)*ui+eps*Dui-sgn*(ur.^2+ui.^2).*ui,n*n,1)];
% auxiliary vectors for Laplacian
ee = eps*ones(n,1);
ee0 = ee; ee0(1) = ee(1)/2; ee0(n) = ee(n)/2;
ee1 = -2*ee0;
% tridiagonal Laplacian for 1d
jj1 = spdiags([ee ee1 ee], -1:1, n, n);
% quick conversion of the 1d n × n tridiagonal
% into the 2d n^2 × n^2 quintidiagonal via the Kronecker product.
% [ note that the linear part of the Jacobian only needs to be
% constructed once at the beginning of the code, but is left here
% for clarity.  ]
```

```
jj22 = kron(speye(n),jj1) + kron(jj1,speye(n))-(V+l)*speye(n*n,n*n);
% nonlinear and external components of the Jacobian
n1 = sparse(n*n,n*n);
n2 = sparse(n*n,n*n);
n3 = sparse(n*n,n*n);
n1 = spdiags(uui.^2 + 3*uur.^2,0,n1);
n2 = spdiags(uur.^2 + 3*uui.^2,0,n2);
n3 = spdiags(2*uur.*uui,0,n3);
nn = -sgn*[n1 n3;n3 n2];
clear n1 n2 n3
% completion of the Jacobian
jj2 = nn + [ jj22, sparse(n*n,n*n);sparse(n*n,n*n), jj22];
clear nn
% Newton correction step
cor = jj2 \ f ;
clear jj2
u1 = u-cor;
% convergence indicator:  should converge quadratically
norm(cor)
end;
% END - see alternative method below
%
% Now, the way that makes sense to compute the
% linear spectrum is to remain in the
% real-imaginary basis as above.  Then,
% we construct the canonical symplectic form
% which transforms it into the linearization.
```

```
Z=sparse(n^2,n^2);I=speye(n^2);J=[Z I;-I Z];
d1=eigs(J*jj2+3*speye(2*n*n),100,'SM')-3;
% alternatively, one can use the rotated complex basis
% as follows:
% convert back into a complex valued vector
uu1 = u1(1:n*n)+sqrt(-1)*u1(n*n+1:2*n*n);
% and it's 2d representation
uu2 = reshape(uu1,n,n);
% construct nonlinear part of stability matrix
n1 = sparse(n*n,n*n);
n2 = sparse(n*n,n*n);
n1 = sgn*spdiags(uu1.^2,0,n1);
n2 = sgn*spdiags(2*abs(uu1).^2,0,n2);
jj2 = jj22 + n2;
jj3=[ jj2, n1;
-conj(n1) -conj(jj2)];
% smallest magnitude ('SM') 100 eigenvalues d and
% eigenvectors v of stability matrix
% (utilizing a shift in order to improve stability of the algorithm)
d1=eigs(jj3+sqrt(-1)*3*speye(2*n*n),100,'SM')-sqrt(-1)*3;
% store solution and stability
u_store(:,it)=uu1;
d_store(:,it)=d1;
e_store(it)=eps;
% visualize the continuation profiles and stability on the fly
subplot(2,2,1)
imagesc(x,y,abs(uu2).^2)
```

```
drawnow;
subplot(2,2,2)
imagesc(x,y,angle(uu2))
drawnow;
subplot(2,2,3)
imagesc(x,y,imag(uu2))
drawnow;
subplot(2,2,4)
plot(imag(d1),real(d1),'o')
drawnow;
% increment indices and epsilon
it=it+1;
eps=eps+0.001;
end;
% save the data
save('sol_eps_2d.mat','u_store','d_store',e_store');
```

We should make a few comments here about the code given above. We have illustrated in the existence portion (the Newton method) and the stability section the respective formulations of the complex-valued problem in terms of the real and imaginary components of the field and the field and its complex conjugate (rotation of the former), respectively The formulations can be interchanged, and it is unnecessary to represent both components in the existence section for real valued solutions (as with 1d solutions) or equivalently any constant phase solution ($\theta \in [0, 2\pi)$, not necessarily 0), while it is always necessary in the linearization problem because we must consider complex valued perturbations even of real solutions. There are many alternative options in eigs other than 'SM', which the interested

readers should perhaps explore. On the other hand, the latter is particularly efficient here because in the discrete setting, the relevant eigenvalues bifurcate from the origin in the anticontinuum limit. For the continuum, they bifurcate from lower energy modes, close to the origin. The reader should beware, however, that eigs uses an Arnoldi iterative method to calculate the eigenvalues and the (unshifted) linearization system is singular due to phase invariance. Therefore, some care has to be taken, by a shift or otherwise.

Now, we briefly outline the alternative method using the MATLAB script nsoli [43] for the existence portion of the above routine. The reader should note that in addition to the benefits mentioned above, it may be attractive as a black box since it slims down the code. Please consult the help file or [43] for more details about it.

```
% setup the parameters for nsoli
max_iter=200;
max_iter_linear=100;
etamax=0.9;
lmeth=1;
restart_limit=20;
sol_parms=[max_iter,max_iter_linear,etamax,lmeth,restart_limit];
error_flag=0;
tolerance=1e-8*[1,1]
% solve with nsoli the equation F(u_)
[u1,iter_hist,error_flag]=nsoli(u1,@(u_)F(u_,eps,n,l),tolerance,sol_parms);
if error_flag==0
else
```

```
disp('there was an error')
iter_hist
break
end
% Now define the function F as a new script F.m in the
% same directory.  (Functions cannot be defined within scripts,
% but can be defined within functions, so if the whole code is
% made into a function, then this routine can be embedded.)
function f = F(u,eps,n,l)
ur = reshape(u(1:n*n),n,n);
ui = reshape(u(n*n+1:2*n*n),n,n);
% evaluation of second difference with zero fixed boundaries
e=zeros(n,1);
Durmm = diff([e';ur;e'],2,1);
Durnn = diff([e,ur,e],2,2);
Duimm = diff([e';ui;e'],2,1);
Duinn = diff([e,ui,e],2,2);
Dur = Durmm + Durnn;
Dui = Duimm + Duinn;
% equation that we are trying to solve (vectorized)
f(1:n*n)=reshape(-(l+V)*ur+eps*Dur-(ur.^2+ui.^2).*ur,n*n,1);
f(n*n+1:2*n*n)=reshape(-(l+V)*ui+eps*Dui-(ur.^2+ui.^2).*ui,n*n,1);
```

We now briefly explore alternative variations of the above codes which appear in this thesis. First, the nonlinearity for the continuum models is typically saturable. This is quite easily accounted for, as the only thing that is affected is the nonlinear term above. The V appearing in the linear term is set to 0. Then, the nonlinear

parts change as follows

```
% the function :
f=[reshape(-l*ur+eps*Dur+sgn./(1+V+ur.^2+ui.^2).*ur,n*n,1); ...
   reshape(-l*ui+eps*Dui+sgn./(1+V+ur.^2+ui.^2).*ui,n*n,1)];
% its linearization :
n1 = spdiags((1+V-uur.^2 + uui.^2)./((1+V+u.^2+v.^2).^2,0,n1);
n2 = spdiags((1+V-uui.^2 + uur.^2)./((1+V+u.^2+v.^2).^2,0,n2);
n3 = spdiags(-2*uur.*uui./((1+V+u.^2+v.^2).^2,0,n3);
nn = sgn*[n1 n3;n3 n2];
```

For the continuum version, the domains are taken to be an integer multiple of the periods of the lattice and the boundary conditions are typically taken as periodic, although this is typically inconsequential since the fields are typically essentially zero at the boundary and all boundary conditions yield the same results. (This is not the case for embedded and extended solutions from Chapter 5)

For the computation of linear spectra (which determine admissible intervals of the propagation constant l in the continuum setting with periodic external potential), we generally employ the method outlined in [47] with the finite difference Laplacian. Sometimes, instead we scan through some number of shifts with a large domain (noting that eigenvalues from the continuous spectrum are limited to intervals of $2\pi/L$ by our computationally truncated domain, extending through the interval $\{\pm\pi/\Delta x\}$, and so the size of the domain dictates how finely we resolve the linear spectrum). With the non-square lattices, for instance, it is more delicate to define a proper cell, periodic in x and y, and so the latter method is preferred.

For the non-square lattices, the discrete Laplacian is generalized to account for

the symmetry of the lattice. For instance, for the hexagonal lattice it becomes

```
% hexagonal discrete Laplacian
a=ones(n^2,1);
Lap=spdiags([1*a,1*a,1*a,-6*a,1*a,1*a,1*a], ...
    [-n-1,-n,-1,0,1,n,n+1],Lap);
k=1:n-1; Lap(k*n,k*n+1)=0; Lap(k*n+1,k*n)=0;
% Kagome discrete Laplacian (note the Kagome lattice
% is a sub-lattice of the hexagonal one)
% set up a characteristic matrix to delete selected nodes
% (rows and columns) from hexagonal arrangement.
A=ones(N,N);
for k=0:(n-1)/2;
for m=0:(n-1)/2;
A(2*k+1,2*m+1)=0;
end
end
aa=reshape(A,n*n,1)';
AA=repmat(aa,n*n,1);
AB=repmat(aa',1,n*n);
a=ones(n^2,1);
% create hexagonal matrix with modified main diagonal
% and delete specified nodes.
Lap=spdiags([1*a,1*a,1*a,-4*a,1*a,1*a,1*a], ...
    [-n-1,-n,-1,0,1,n,n+1],Lap).*AA.*AB;
k=1:n-1; Lap(k*n,k*n+1)=0; Lap(k*n+1,k*n)=0;
```

For the case of parametric continuation, many methods are available. The simplest and most intuitive involves solving the equation, stepping forward the parameter and solving once again with the solution from the previous step as the initial guess. This method is presented above and is guaranteed to work for a small enough step size, provided such a solution exists. On the other hand, in the case of turning branches, which occur from the collision and disappearance of 2 solution branches (as occurs for certain solutions in all the continuum cases investigated herein), no step size is small enough because the solution ceases to exist. Hence, methods have been developed which step forward some other parameter other than the continuation parameter. The most famous such method is the pseudo-arclength method, coined by Doedel [44], in which one adds a constraint that the arclength of the branch is a specific length, allowing the parameter in the continuation to be another unknown. With an additional equation, the constraint, and an additional unknown, the continuation parameter, the situation is the same, except a continuation in this parameter has no restriction of continuing in any particular direction. So, in the case of the collision and disappearance of 2 or more branches, the continuation will simply follow a colliding branch, solving for the colliding family of solutions over the same parameter values as for the initial branch, provided the arc-length parameter is chosen small-enough. This way, we are able to identify the saddle-node bifurcations.

BIBLIOGRAPHY

[1] P.G. Kevrekidis (ed), *The Discrete Nonlinear Schrödinger Equation Mathematical Analysis, Numerical Computations and Physical Perspectives'*, Springer-Berlin (Heidelberg, 2008).

[2] C. Sulem and P.L. Sulem, *The Nonlinear Schr odinger Equation*, Springer-Verlag (New York, 1999).

[3] L.P. Pitaevskii and S. Stringari, *Bose-Einstein Condensation*, Oxford University Press (Oxford, 2003).

[4] P.G. Kevrekidis, D.J. Frantzeskakis, and R. Carretero-González (eds). *Emergent Nonlinear Phenomena in Bose-Einstein Condensates: Theory and Experiment* (Springer-Verlag, Heidelberg, 2008).

[5] G.P. Agrawal, *Nonlinear fiber optics (4th ed)*, Academic Press (London, 2003).

[6] Y.S. Kivshar and G.P. Agrawal, *Optical Solitons: From Fibers To Photonic Crystals*, Academic Press (London, 2003).

[7] J.D. Joannopoulos, S.G. Johnson, J.N. Winn, and R.D. Meade, *Photonic Crystals: Molding the Flow of Light (2nd ed.)*. Princeton University Press (Princeton NJ, 2008).

[8] H.S. Eisenberg, Y. Silberberg, R. Morandotti, A. R. Boyd and J. S. Aitchison, Phys. Rev. Lett. **81**, 3383 (1998).

[9] R. Morandotti, U. Peschel, J. S. Aitchison, H. S. Eisenberg and Y. Silberberg, Phys. Rev. Lett. **83**, 2726-2729 (1999); H. S. Eisenberg, Y. Silberberg, R. Morandotti and J. S. Aitchison, Phys. Rev. Lett. **85**, 1863 (2000).

[10] D. Mandelik, R. Morandotti, J. S. Aitchison, and Y. Silberberg, Phys. Rev. Lett. **92**, 093904 (2004).

[11] D. N. Christodoulides, F. Lederer, and Y. Silberberg, Nature **424**, 817 (2003); A. A. Sukhorukov, Y. S. Kivshar, H. S. Eisenberg, and Y. Silberberg, IEEE J. Quant. Elect. **39**, 31 (2003).

[12] S. Aubry, Physica **103D**, 201 (1997); S. Flach and C. R. Willis, Phys. Rep. **295**, 181 (1998); D. K. Campbell, S. Flach, and Y. S. Kivshar, Phys. Today, January 2004, p. 43; P.G. Kevrekidis, K.Ø. Rasmussen and A.R. Bishop, Int. J. Mod. Phys. B **15**, 2833 (2001); D.E. Pelinovsky, P.G. Kevrekidis and D.J. Frantzeskakis, Physica D **212**, 20 (2005). P.G. Kevrekidis (ed). *The Discrete Nonlinear Schrdinger Equation Mathematical Analysis, Numerical Computations and Physical Perspectives'* (Springer-Berlin, Heidelberg, 2008).

[13] N.K. Efremidis, S. Sears, D. N. Christodoulides, J. W. Fleischer, and M. Segev Phys. Rev. E **66**, 46602 (2002).

[14] J.W. Fleischer, M. Segev, N.K. Efremidis and D.N. Christodoulides, Nature **422**, 147 (2003); J.W. Fleischer, T. Carmon, M. Segev, N.K. Efremidis and D.N. Christodoulides, Phys. Rev. Lett. **90**, 23902 (2003).

[15] J. Yang, I. Makasyuk, A. Bezryadina, and Z. Chen, Opt. Lett. **29**, 1662 (2004).

[16] J. Yang, I. Makasyuk, A. Bezryadina, and Z. Chen, Stud. Appl. Math. **113**, 389 (2004).

[17] D. Neshev, Yu. S. Kivshar, H. Martin, and Z. Chen, Opt. Lett. **29**, 486-488 (2004).

[18] J. Yang, I. Makasyuk, P. G. Kevrekidis, H. Martin, B. A. Malomed, D. J. Frantzeskakis, and Zhigang Chen, Phys. Rev. Lett. **94**, 113902 (2005).

[19] X. Wang, Z. Chen, and P. G. Kevrekidis, Phys. Rev. Lett. **96**, 083904 (2006).

[20] D. N. Neshev, T.J. Alexander, E.A. Ostrovskaya, Yu.S. Kivshar, H. Martin, I. Makasyuk and Z. Chen, Phys. Rev. Lett. **92**, 123903 (2004); J. W. Fleischer, G. Bartal, O. Cohen, O. Manela, M. Segev, J. Hudock, and D.N. Christodoulides Phys. Rev. Lett. **92**, 123904 (2004).

[21] G. Bartal, O. Manela, O. Cohen, J.W. Fleischer and M. Segev, Phys. Rev. Lett. **95**, 053904 (2005).

[22] D. Träger, R. Fischer, D.N. Neshev, A.A. Sukhorukov, C. Denz, W. Królikowski and Yu.S. Kivshar, Optics Express **14**, 1913 (2006).

[23] H. Trompeter, W. Królikowski, D.N. Neshev, A.S. Desyatnikov, A.A. Sukhorukov, Yu.S. Kivshar, T. Pertsch, U. Peschel and F. Lederer, Phys. Rev. Lett. **96**, 053903 (2006).

[24] O. Peleg, G. Bartal. B. Freedman, O. Manela, M. Segev and D.N. Christodoulides, Phys. Rev. Lett. **98**, 103901 (2007).

[25] C.R. Rosberg, D.N. Neshev, A.A. Sukhorukov, W. Krolikowski and Yu.S. Kivshar, Opt. Lett. **32**, 397 (2007).

[26] B. Freedman, G. Bartal, M. Segev, R. Lifshitz, D.N. Christodoulides and J.W. Fleischer, Nature **440**, 1166 (2006).

[27] T. Schwartz, G. Bartal, S. Fishman and M. Segev, Nature **446**, 52 (2007).

[28] J.W. Fleischer, G. Bartal, O. Cohen, T. Schwartz, O. Manela, B. Freedman, M. Segev, H. Buljan and N. K. Efremidis, Opt. Express **13**, 1780 (2005).

[29] Z. Chen, H. Martin, E. Eugenieva, J. Xu, and J. Yang, Opt. Express **13**, 1816 (2005).

[30] P.G. Kevrekidis, B.A. Malomed, and Yu.B. Gaididei, Phys. Rev. E **66**, 016609 (2002).

[31] A. Szameit, Y. V. Kartashov, F. Dreisow, M. Heinrich, V. A. Vysloukh, T. Pertsch, S. Nolte, A. Tunnermann, F. Lederer and L. Torner, Opt. Lett. **33**, 663 (2008).

[32] V. Koukouloyannis and R.S. MacKay, J. Phys. A: Math. Gen. **38**, 1021 (2005).

[33] T.J. Alexander, A.S. Desyatnikov and Yu.S. Kivshar, Opt. Lett. **32**, 1293 (2007).

[34] H. Sakaguchi and B. A. Malomed. Phys. Rev. E **74**, 026601 (2006).

[35] K.J.H. Law, H. Susanto, and P.G. Kevrekidis. Phys. Rev. A **78**, 033802 (2008).

[36] K.J.H. Law, P.G. Kevrekidis, V. Koukouloyannis, I. Kourakis, D.J. Frantzeskakis, and A.R. Bishop. Phys. Rev. E **78**, 066610 (2008).

[37] L. Tang, C. Lou, X. Wang, D. Song, X. Chen, J. Xu, Z. Chen, H. Susanto, K. Law and P.G. Kevrekidis, Opt. Lett. **32**, 3011 (2007).

[38] D. Song, L. Tang, C. Lou, X. Wang, J. Xu, Z. Chen, H. Susanto, K.J.H. Law, and P.G. Kevrekidis. Opt. Exp. **16**, 10110 (2008).

[39] P.G. Kevrekidis, H. Susanto and Z. Chen, Phys. Rev. E **74**, 066606 (2006).

[40] B. Terhalle, et. al. Phys. Rev. A **79**, 043821 (2009)

[41] J. Yang, New J. Phys. **6**, 47 (2004).

[42] J. Yang, A. Bezryadina, I. Makasyuk and Z. Chen, Stud. Appl. Math. **113**, 389 (2004).

[43] C. T. Kelley, *Solving Nonlinear Equations with Newton's Method*, no. 1 in Fundamentals of Algorithms, SIAM, Philadelphia, 2003.

[44] E. Doedel. International Journal of Bifurcation and Chaos. 7(9):2127-2143, 1997.

[45] T. Kapitula, P.G. Kevrekidis, B. Sandstede, Physica D **195** 263 (2004).

[46] J.-C. van der Meer, Nonlinearity **3**, 1041 (1990).

[47] B. Deconinck and J. Nathan Kutz, J. Comp. Physics **219**, 296-321, 2006

[48] D. Pelinovsky, A.A. Sukhorukov, and Yu.S. Kivshar, Phys. Rev. E **70**, 036618 (2004).

[49] Z. Shi and J. Yang, Phys. Rev. E **75**, 056602 (2007).

[50] Z. Chen and K. McCarthy, Opt. Lett. **27**, 2019 (2002).

[51] C. Lou, X. Wang, J. Xu, Z. Chen and J. Yang, Phys. Rev. Lett. **98**, 213903 (2007).

[52] D. Neshev, E. Ostrovskaya, Yu.S. Kivshar and W. Krolikowski, Opt. Lett. **28**, 710 (2003).

[53] H. Martin, E.D. Eugenieva, Z. Chen and D.N. Christodoulides, Phys. Rev. Lett. **92**, 123902 (2004).

[54] G. Bartal, O. Cohen, H. Buljan, J. W. Fleischer, O. Manela, and M. Segev, Phys. Rev. Lett. **94**, 163902 (2005).

[55] A. Bezryadina, E. Eugenieva, and Z. Chen, Opt. Lett. **31**, 2456 (2006).

[56] J. Wang and J. Yang, Phys. Rev. A **77**, 033834 (2008).

[57] V. Koukouloyannis. Submitted to JPA.

[58] P K Shukla and A.A Mamun, *Introduction to Dusty Plasma Physics*, Institute of Physics Publishing (Bristol, 2002); S.V. Vladimirov, K. Ostrikov, and A.A. Samarian, *Physics and Applications of Complex Plasmas*, Imperial College Press (London, 2005).

[59] G. E. Morfill, H. M. Thomas & M. Zuzic, *Plasma crystals - a review*, in *Advances in Dusty Plasma Physics*, Eds. P.K. Shukla, D.A. Mendis, & T. Desai, World Scientific (Singapore, 1997); G .E. Morfill, B.M. Annaratone, P. Bryant, A.V. Ivlev, H.M. Thomas, M. Zuzic and V.E. Fortov, Plasma Phys. Control. Fusion **44**, B263 (2002).

[60] O. Ishihara, announcement in *5th Int. Conf. Phys. Dusty Plasmas*, Ponta Delgada, Azores (2008); private communication.

[61] T. Misawa, N. Ohno, K. Asano, M. Sawai, S. Takamura, & P. K. Kaw, Phys. Rev. Lett. **8**6, 1219 (2001).

[62] V. Koukouloyannis and I. Kourakis, Phys. Rev. E **76**, 016402 (2007).

[63] V. Koukouloyannis and I. Kourakis, *Existence and stability of discrete multi-breathers in hexagonal dusty plasma crystals*, in preparation.

[64] see e.g., P.G. Kevrekidis, B.A. Malomed and A.R. Bishop, J. Phys. A **34**, 9615 (2001) and T. Kapitula, P.G. Kevrekidis, and B.A. Malomed, Phys. Rev. E **63**, 036604 (2001).

[65] H. Susanto, K. Law, P.G. Kevrekidis, L. Tang, C. Lou, X. Wang, and Z. Chen, Physica D **237**, 3123 (2008).

[66] B. Terhalle, T. Richter, A.S. Desyatnikov, D.N. Neshev, W. Krolikowski, F. Kaiser, C. Denz, and Yu.S. Kivshar, Phys. Rev. Lett. **101**, 013903 (2008).

[67] See e.g., C. Becker, P. Soltan-Panahi, J. Kronjager, S. Stellmer, K. Bongs and K. Sengstock, "Spinor BEC in Triangular Optical Lattices", IB1_1 IQEC (2007).

[68] Yu.S. Kivshar and M. Peyrard, Phys. Rev. A **46**, 3198 (1992); D.N. Christodoulides and R.I. Joseph, Opt. Lett. **13**, 794 (1988).

[69] B. Terhalle, A. S. Desyatnikov, C. Bersch, D. Träger, L. Tang, J. Imbrock, Yu. S. Kivshar and C. Denz, App. Phys. B **86**, 399 (2007).

[70] B. Terhalle, T. Richter, A. S. Desyatnikov, D. N. Neshev, W. Krolikowski, F. Kaiser, C. Denz, and Y. S. Kivshar, Phys. Rev. Lett. **101**, 013903 (2008).

[71] R. Fischer, D. Träger, D. N. Neshev, A. A. Sukhorukov, W. Krolikowski, C. Denz, and Yu. S. Kivshar, Phys. Rev. Lett. **96**, 023905 (2006).

[72] D. Träger, R. Fischer, D. N. Neshev, A. A. Sukhorukov, C. Denz, W. Krolikowski, and Yu. S. Kivshar, Opt. Express **14**, 1913 (2006).

[73] K. J. H. Law, P. G. Kevrekidis, T. J. Alexander, W. Krolikowski, and Yu. S. Kivhsar, Phys. Rev. A **79**, 025801 (2008).

[74] A. Ya. Bekshaev, M. S. Soskin and M. V. Vasnetsov, Opt. Comm. **241**, 237 (2004).

[75] A. A. Zozulya, D. Z. Anderson, A. V. Mamaev, and M. Saffman, Phys. Rev. A **57**, 522 (1998).

[76] D.N. Christodoulides and R.I. Joseph, Opt. Lett. **13**, 794 (1988); Yu.S. Kivshar and M. Peyrard, Phys. Rev. A **46**, 3198 (1992).

[77] L. Santos, M.A. Baranov, J.I. Cirac, H.-U. Everts, H. Fehrmann, and M. Lewenstein, Phys. Rev. Lett. **93**, 030601 (2004); B. Dmaski, H.-U. Everts, A. Honecker, H. Fehrmann, L. Santos, and M. Lewenstein, Phys. Rev. Lett. **95**, 060403 (2005); B. Damski, H. Fehrmann, H.-U. Everts, M. Baranov, L. Santos, and M. Lewenstein, Phys. Rev. A **72**, 053612 (2005).

[78] R.G. Hutchinson and N.A. Fleck. J. Mech. and Phys. Sol. **54** 756 (2006).

[79] F.C. Coomer, A. Harrison, G.S. Oakley, J. Kulda, J.R. Stewart, J.A. Stride, B. Fak, J.W. Taylor, and D. Visser. J. Phys.: Cond. Matt. **18** 8847 (2006).

[80] K. Atkinson, *An Introduction to Numerical Analysis*, John Wiley (New York, 1989).

[81] M.J. Ablowitz and Z.H. Musslimani, Opt. Lett. **30**, 2140 (2005).

[82] T.I. Lakoba and J. Yang, J. Comp. Phys. **226**, 1668 (2007).

[83] D.E. Pelinovsky, Yu.A. Stepanyants, SIAM J. Numer. Anal. **42**, 1110 (2004).

[84] J. Yang and T.I. Lakoba, arXiv:0711.3434.

[85] J.J. Garcia-Ripoll and V.M. Perez-Garcia, SIAM J. Sci. Comput. **23**, 1315 (2001).

[86] T. R. Taha and M. J. Ablowitz, J. Comp. Phys. **55**, 203 (1984).

[87] E. Hairer, S.P. Norsett and G. Wanner, *Solving ordinary differential equations. I: Nonstiff Problems*, Springer-Verlag (Berlin, 1987).

[88] See http://www.mathworks.com

[89] See the webspace http://www.math.umass.edu/∼law/Research/DNLS_codes/.

[90] R. Mackay. Stability of equilibria of Hamiltonian Systems. In R. Mackay and J. Meiss, eds., *Hamiltonian Dynamical Systems*, pages 137-153. Adam Hilger, (1987).

[91] M.I. Weinstein. Comm. Pure and Appl. Math. **39**, 51-68 (1986).

[92] A.J. Dragt. Ann. N.Y. Acad. Sci. **1045**, 291-307 (2006).